The Investigation on Electrical and Artificial Synaptic Performance of Resistive Random Access Memory Fabricated with Solution-Processed Materials

基于溶液法制材料的阻变随机存储器的电学及其人工突触特性的研究

A Dissertation Submitted to

University of Liverpool

in Partial Fulfillment of the Requirements for

the Degree of Doctor of Philosophy

in the Department of Electrical Engineering and Electronics

2021

By:

Zongjie Shen

Abstract

For now, extensive effort has been put on resistive random access memory devices (RRAM) due to the advantages of low energy consumption, fast writing & erasing speed, large storage capacity, and excellent scalability. To explore the resistive switching (RS) of the RRAM device with lower economic cost and higher manufacturing efficiency, the emerging solution-processed (SP) spin-coating technique was utilized to fabricate RS layers. The primary research work in this thesis mainly focused on the electrical and artificial synaptic performance of RRAM devices with their RS layers fabricated by the SP spin-coating technique, which was divided into Phases 1, 2, and 3). In Phase 1(**Chapter 2**) of this thesis, RRAM devices with the structures of Ni/SP-AlO_x/Pt and TiN/SP-AlO_x/Pt were investigated with their performance variation and the Ni/SP-AlO_x/Pt device showed better performance with lower operation voltage, which was associated with the different work functions (Φ_M) of Ni and TiN. The electrical performance of the Ni/SP-AlO_x/Pt devices was evaluated with the SP-AlO_x layers annealed at 225°C, 250°C, and 275°C. The final results revealed that the performance of the SP-AlO_x layers and the RRAM devices was influenced by the concentration of hydroxyl group (-OH) in the RS layer, higher -OH concentration in the SP-AlO_x layer indicated that more oxygen vacancies were generated during the RS process. In Phase 2 (**Chapter 3**) of this thesis, improvement methods were used to enhance the electrical performance of the new RRAM device. Ni was replaced by Ag, and Pt was replaced by ITO. The RS layer with a single SP-AlO_x thin film was replaced with a stacked layer with the SP-GaO_x/SP-AlO_x thin film. The improved RRAM device with the structure of Ag/SP-GaO_x/SP-AlO_x/ITO was fabricated and the device showed a lower operation voltage, a larger ON/OFF ratio, longer retention time, and more endurance cycles. In Phase 3 (**Chapter 4**) of this thesis, based on the enhanced electrical performance in Phase 2, the multi-level states of current and conductance for the Ag/SP-GaO_x/SP-AlO_x/ITO RRAM device were confirmed and indicated the great potential of the Ag/SP-GaO_x/SP-AlO_x/ITO RRAM device as the artificial synaptic devices. Related artificial synaptic behaviors of the

Ag/SP-GaO_x/SP-AlO_x/ITO RRAM device were investigated based on the multi-level conductance response to electrical pulses, including excitatory postsynaptic current (EPSC), short-term plasticity like paired-pulse facilitation (PPF), long-term plasticity like long-term potentiation (LTP) and long-term depression (LTD), and spiking-timing-dependent plasticity (STDP). By modulating input pulses, the short-term plasticity of the Ag/SP-GaO_x/SP-AlO_x/ITO RRAM device transit to the long-term potentiation, an integrated RRAM array comprising of multiple devices emulated the biomimetic human-brain-like behaviors of 'learning - forgetting - relearning - memorizing'. In addition, with significant parameters obtained in LTP and LTD performance of the Ag/SP-GaO_x/SP-AlO_x/ITO RRAM device, a pattern recognition system based on the artificial neuron network (ANN) algorithm was carried on handwriting Arabic numbers 0 ~ 9. The final average accuracy was about 94% and the highest accuracy was ~ 98%.

Keywords: Solution-processed; Spin-coating; Artificial synaptic behavior; Stacked layer; Pattern recognition.

摘要：

目前，电阻式随机存取存储器（RRAM）由于其能耗低、写入擦除速度快、存储容量大、扩展性好等优点而被广泛研究。为了在使用较低的经济成本制备 RRAM 器件并探索其阻变（RS）性能的同时提高器件的制备效率，利用新兴的旋涂式溶液法制备阻变层薄膜变的越来越广泛。本文的主要工作分为三个阶段，主要针对基于旋涂式溶液法制阻变层 RRAM 器件的电学特性和人工突触特性进行研究。第一阶段中（第二章），主要研究基于镍/溶液法制氧化铝/铂（Ni/SP-AlO_x/Pt）结构和基于氮化钛/溶液法制氧化铝/铂结构（TiN/SP-AlO_x/Pt）的 RRAM 器件之间的电学性能差异。由于镍和氮化钛的功函数差异，镍/溶液法制氧化铝/铂具有更低的操作电压和能耗，电学性能更好。此外还针对不同温度下（225°C、250°C、275°C）退火的镍/溶液法制氧化铝/铂器件进行研究。结果表明溶液法制氧化铝薄膜和器件的表现均受到薄膜中氢氧根（-OH）含量的影响，氢氧根含量越高，阻变过程中会出现更多的氧空位。第二阶段中（第三章），通过更换上下电极材料和阻变层结构改进器件的性能。银代替镍作为顶电极，氧化铟锡代替铂作为底电极，原先的单层溶液法制氧化铝被叠层结构的溶液法制氧化镓/溶液法制氧化铝所替代。新制备的银/溶液法制氧化镓/溶液法制氧化铝/氧化铟锡（Ag/SP-GaO_x/SP-AlO_x/ITO）表现出了更加优异的电学性能，如更低的操作电压，更大的阻变窗口，更长时间的保持特性以及更好的耐受性。第三阶段中（第四章），叠层阻变层器件在表现出优秀电学性能的同时也展现了其电流和电导的多级状态，证明其具有作为人工突触器件的研究潜力。该阶段中主要针对器件的在脉冲刺激下的人工突触响应特性进行研究，其中包括兴奋性突触后电流（EPSC），短期可塑性（short-term plasticity）中的对脉冲易化（PPF），长期可塑性（long-term plasticity）

中的长期增程兴奋特性（LTP）和长期降程抑制特性（LTD），以及依赖尖峰时间的突触可塑性（STDP）。通过对输入脉冲的调制，单个器件的短期可塑性被转化为长期可塑性，多个器件组成的阵列模拟人脑实现了“学习-遗忘-再学习-记忆”的仿生特性。此外，通过利用长期增程兴奋和长期降程抑制特性中的关键参数，构建了基于人工神经元网络（ANN）算法的模式识别系统并对手写的阿拉伯数字进行识别，平均识别率约为 94%且最高可达到约 98%。

关键词：溶液法；旋涂；人工突触特性；叠层阻变层；图像识别

Acknowledgments

First of all, I sincerely thank my supervisor, Associate Professor. Chun Zhao, for allowing me to engage in scientific research. For me, who was not optimistic at that time, I was lucky enough to get a Ph.D. student admission. Whether in life or work, my supervisor Chun Zhao always gave me a lot of support. When I face many problems, he always encourages me and inspires me to try to solve those problems. When I encountered a problem during the experiment, he always comforted me and at the same time worked with me to find the reason for the failure of the experiment, and strictly checked my experiment plan. When I encounter problems in the process of writing an article, he always prompted me to look for suitable references, and he always kept reminding me of the necessary details. Precisely, because of his guidance and patience, I have gradually grown from a layman who knows nothing about scientific research to a qualified Ph.D. student.

The second person I would like to thank is Professor. Cezhou Zhao, who was quite prestigious in the semiconductor industry in China and the world. The solid knowledge reserve and the rigorous academic attitude of Prof. Cezhou Zhao have had a great impact on me. However, the sudden pass away of Prof. Cezhou Zhao hit us all by surprise. I will never have the opportunity to say ‘thank you, sir’ to Professor in person.

Then I would like to thank my mother and my fiancée Lin. When I started my university life in 2012, my father passed away due to gastric disease. My mother has always

supported me alone over these years. After the graduation of my Ph.D. life, my mother will retire and I must take the responsibility of supporting my family. For my fiancée Lin, my dear, I am sincerely grateful that you support me without hesitation when I had nothing. It is my honor to meet with you at that special period. In the future, we will support each other for the rest of our lives, I promise that I will use the rest of my life to care and love you for your selfless dedication to me.

At last, I would like to give my sincere gratitude to my fellows Dr. Yanfei Qi, Dr. Yuxiao Fang, Dr. Chenguang Liu, Dr. Yinchao Zhao, Dr. Miao Cui, Dr. Qifeng Lu, Miss. Yi Sun, Mr. Tianshi Zhao, Mr. Yixin Cao, Mr. Qinan Wang, Mr. Li Yin, Miss. Xiaoping Chen, Mr. Xinkai Xie, Mr. Tian Luo, Miss. Jiahuan He, Mr. Yanbo Huang, Mr. Puzhuo Li, Mr. Zezhou Fan, Mr. Jiacheng Wen and Mr. Qihan Liu.

The research in this thesis was funded in part by the Natural Science Foundation of the Jiangsu Higher Education Institutions of China Program (19KJB510059), Natural Science Foundation of Jiangsu Province of China (BK20180242), the Suzhou Science and Technology Development Planning Project: Key Industrial Technology Innovation (SYG201924), University Research Development Fund (RDF-17-01-13), and the Key Program Special Fund in XJTLU (KSF-P-02, KSF-T-03, KSF-A-04, KSF-A-05, KSF-A-07, KSF-A-18).

Content

List of Publications

Journal Paper

Zongjie Shen, Chun Zhao*, Yina Liu, Yanfei Qi, Ivona Z Mitrovic, Li Yang, Cezhou Zhao, Performance variation of solution-processed memristor induced by different top electrode, *Solid-State Electronics*, Vol. 186, pp. 108132 (1-6). 2021
DOI: https://doi.org/10.1016/j.sse.2021.108132

Zongjie Shen, Chun Zhao*, Tianshi Zhao, Wangying Xu, Yina Liu, Yanfei Qi, Ivona Z Mitrovic, Li Yang, Ce Zhou Zhao, Artificial Synaptic Performance with Learning Behavior for Memristor Fabricated with Stacked Solution-Processed Switching Layers, *ACS Applied Electronic Materials*, Vol. 3, No. 3, pp. 1288-1300, 2021
DOI: https://doi.org/10.1021/acsaelm.0c01094

Zongjie Shen, Chun Zhao*, Yanfei Qi, Wangying Xu, Yina Liu, Ivona Z Mitrovic, Li Yang, Cezhou Zhao, Advances of RRAM devices: resistive switching mechanisms, materials and bionic synaptic application, *Nanomaterials*, Vol. 10, No. 8, pp. 1437 (1-31), 2020
DOI: https://doi.org/10.3390/nano10081437

Yan Fei Qi§, **Zong Jie Shen§**, Chun Zhao*, Ivona Z. Mitrovic, Wang Ying Xu, Eng Gee Lim, Li Yang, Jia Huan He, Tian Luo, Yan Bo Huang, Ce Zhou Zhao, Resistive switching behavior of solution-processed AlO_x and GO based RRAM at low temperature, *Solid-State Electronics*, Vol. 168, pp. 107735 (1-5), 2020 (co-first author)
DOI: https://doi.org/10.1016/j.sse.2019.107735

Yanfei Qi, **Zongjie Shen**, Chun Zhao*, Ce Zhou Zhao, Effect of electrode area on resistive switching behavior in translucent solution-processed AlO_x based memory device, *Journal of Alloys and Compounds*, Vol. 822, pp. 153603 (1-10), 2020
DOI: https://doi.org/10.1016/j.jallcom.2019.153603

Zongjie Shen, Chun Zhao*, Yanfei Qi, Ivona Z Mitrovic, Li Yang, Jiacheng Wen, Yanbo Huang, Puzhuo Li, Cezhou Zhao, Memristive non-volatile memory based on graphene materials, *Micromachines*, Vol. 11, No. 4, pp. 341 (1-26), 2020
DOI: https://doi.org/10.3390/mi11040341

Yanfei Qi, Chun Zhao, Ce Zhou Zhao*, Wangying Xu, **Zongjie Shen**, Jiahuan He, Tianshi Zhao, Yuxiao Fang, Qihan Liu, Ruowei Yi, Li Yang, Enhanced resistive switching performance of aluminum oxide dielectric with a low temperature solution-processed method, *Solid-State Electronics*, Vol. 158, pp. 28-36, 2019
DOI: https://doi.org/10.1016/j.sse.2019.05.007

Zongjie Shen, Yanfei Qi, Ivona Z Mitrovic, Cezhou Zhao, Steve Hall, Li Yang, Tian Luo, Yanbo Huang, Chun Zhao*, Effect of annealing temperature for Ni/AlO_x/Pt RRAM devices fabricated with solution-based dielectric, *Micromachines*, Vol. 10, No. 7, pp. 446 (1-12), 2019
DOI: https://doi.org/10.3390/mi10070446

Conference Paper

Zongjie Shen, Chun Zhao*, Ka Lok Man, Yina Liu, Cezhou Zhao, Long-term memory performance with learning behavior of artificial synaptic memristor based on stacked solution-processed switching layers, *2021 IEEE International Symposium on Circuits and Systems (ISCAS)*, IEEE, Daegu, Korea (South), 2021
DOI: 10.1109/ISCAS51556.2021.9401493

Zongjie Shen, Chun Zhao*, Li Yang, Cezhou Zhao, Bionic Synaptic Application of OxRRAM Devices, *2020 International SoC Design Conference (ISOCC)*, IEEE, Yeosu, Korea (South), 2020
DOI: 10.1109/ISOCC50952.2020.9333055

Zongjie Shen, Chun Zhao*, Ivona Z Mitrovic, Cezhou Zhao, Li Yang, Resistive Switching Performance of RRAM Device with Stacked Solution-based Dielectric Layers, *2020 Joint International EUROSOI Workshop and International Conference on Ultimate Integration on Silicon (EUROSOI-ULIS)*, IEEE, Caen, France, 2020
DOI: 10.1109/EUROSOI-ULIS49407.2020.9365382

Zongjie Shen, Cezhou Zhao*, Li Yang, Chun Zhao, Resistive Switching Behavior of Solution-Processed AlO_x, based RRAM with Ni and TiN Top Electrode at Low Annealing Temperatures, *2019 International SoC Design Conference (ISOCC)*, IEEE, Jeju, Korea (South), 2019
DOI: 10.1109/ISOCC47750.2019.9027657

Zong Jie Shen, Chun Zhao*, Ce Zhou Zhao, Ivona Z Mitrovic, Li Yang, Wang Ying Xu, Eng Gee Lim, Tian Luo, Yan Bo Huang, *2019 International Conference on IC Design and Technology (ICICDT)*, IEEE, Suzhou, China, 2019
DOI: 10.1109/ICICDT.2019.8790838

Zong Jie Shen, Chun Zhao*, Ce Zhou Zhao*, Ivona Z. Mitrovic, Li Yang, Wang Ying Xu, Eng Gee Lim, Tian Luo, Yan Bo Huang, Al/GO/Si/Al RRAM with Solution-processed GO dielectric at Low Fabrication Temperature, *2019 Joint International EUROSOI Workshop and International Conference on Ultimate Integration on Silicon (EUROSOI-ULIS)*, IEEE, Grenoble, France, 2019
DOI: 10.1109/EUROSOI-ULIS45800.2019.9041877

Yan Fei Qi, Ce Zhou Zhao, Chun Zhao*, Ivona Z. Mitrovic, Wang Ying Xu, Li Yang,

Zong Jie Shen, Jia Huan He, Improved Resistive Switching Behavior in Solution-processed AlO_x based RRAM, *2019 Joint International EUROSOI Workshop and International Conference on Ultimate Integration on Silicon (EUROSOI-ULIS)*, IEEE, Grenoble, France, 2019
DOI: 10.1109/EUROSOI-ULIS45800.2019.9041862

Chun Zhao*, **Zong Jie Shen**, Guang You Zhou, Ce Zhou Zhao, Li Yang, Ka Lok Man, Eng Gee Lim, Neuromorphic Properties of Memristor towards Artificial Intelligence, 2018 International SoC Design Conference (ISOCC), IEEE, Daegu, Korea (South), 2018
DOI: 10.1109/ISOCC.2018.8649926

List of Figures

List of Tables

List of Abbreviations and Acronyms

$Al(NO_3)_3 \cdot 9H_2O$	Aluminum nitrate hydrate
$\Delta\Phi_M$	Work function difference
AFM	Atomic force microscope
Ag	Silver
AlO_x/Al_2O_3	Aluminum oxide
ANN	Artificial neuron network
BE	Bottom electrode
CF	Conductive filament
EPSC	Excitatory postsynaptic current
GaO_x	Gallium oxide
GO	Graphene oxide
HRS	High-resistance-state
I_{CC}	Compliance current
InO_x	Indium oxide
ITO	Indium tin oxide
LRS	Low-resistance-state
LTD	Long-term depression
LTM	Long-term memory
LTP	Long-term potentiation
MNIST	Mixed National Institute of Standards and Technology
MO	Metal oxide

M-O	Metal oxide bond
Ni	Nickel
NL	Nonlinearity
NL_{LT-D}	Nonlinearity of LTD
NL_{LT-P}	Nonlinearity of LTP
NVM	Non-volatile memory
-OH	Hydroxyl group
P_A	Pulse amplitude/amplitude of a pulse
PPF	Paired-pulse facilitation
Pt	Platinum
P_W	Pulse width/width of a pulse
RRAM	Resistive random access memory
RS	Resistive switching
SCLC	Space-charge-limited current
SEM	Scanning electron microscope
SP	Solution-processed
STDP	Spiking-timing-dependent plasticit
STM	Short-term memory
TE	Top electrode
TiN	Titanium nitride
V_{RESET}	RESET voltage
V_{SET}	SET voltage

XPS	X-ray photoelectron spectroscopy
XRD	X-ray diffraction
Φ_M	Work function

Chapter 1: Background and introduction

1.1 Review of RRAM devices

1.1.1 Background and overview

With the mass production and commercial application of integrated circuit (IC) chips fabricated with 7 nm technology, the exploration of semiconductor processes has mainly focused on 5 nm technology nodes and smaller technology processes. [1-3] The increasing requirements for device miniaturization make the memory industry, a branch of the IC industry, face unprecedented challenges. The size limitation of silicon-based materials has indicated that the storage density of traditional silicon-based volatile memory devices has been getting closer to the intrinsic limit of its materials. [4] As one of the significant components of the computer, the memory is responsible for some primary work such as the storage of original data, the intermediate operating process of the calculation program, and the final output of operation result, which makes the computer realize the memory function. [5, 6] According to the length of information retention time, the memory is divided into two types, volatile memory (VM) and non-volatile memory (NVM). [7, 8] As illustrated in **Fig. 1-1**, the VM device is characterized by the loss of stored information after a power failure, and its main function is to store programs that are used for a short period of time, such as static random access memory (SRAM) and dynamic random access memory (DRAM). [9]

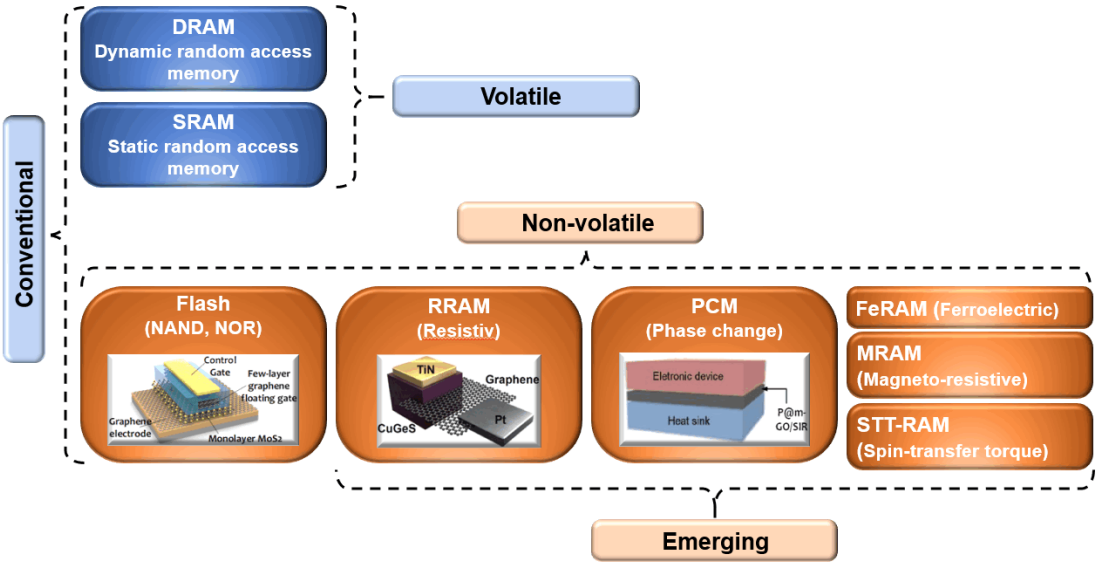

Figure. 1-1 Schematic view of VM and NVM devices with conventional and emerging technologies. [10, 11]

For the NVM device, the information is still stored after a power failure, such as flash memory, phase-change memory (PCM), and resistive random access memory (RRAM), etc. [5, 10, 11] With the increasing popularity of portable electronic devices such as mobile phones and digital cameras, NVM devices are also playing an increasingly important role. DRAM, which currently occupies a dominant position in the commercial market, needs to maintain a certain voltage during the operation process to preserve the information stored in it due to its inherent volatility. [12, 13] This property not only brings extra power consumption to the circuit but also results in a burden to the integration density of the circuit. [12, 13] Although traditional NVM devices such as flash memory are non-volatile, their long response period (~ 100 μs) and low capacity of erasing/writing processes (~10^5) still cannot meet further demands. [14, 15] Hence, it is necessary to explore the emerging NVM device with a simpler structure, a smaller device size, a faster operating (erasing/writing/reading) speed, lower power

consumption, higher storage density, and better CMOS compatibility. As representatives of the new generation of NVM devices, devices like ferroelectric random access memory (FeRAM), magneto-resistive random access memory (MRAM), spin-transfer torque random access memory (STT-RAM), and RRAM have received widespread attention, which has been presented in **Table 1-1**. [10, 11] However, it is hard to realize the further size miniaturization on FeRAM and MRAM while the fabrication cost of STT-RAM is relatively higher. [11, 13, 15] Therefore, more researchers have put their effort into RRAM devices due to their excellent prospects for miniaturization and economic cost reduction.

Table 1-1. Figure of merit (FoM) comparison among main conventional and emerging memory devices [10, 11]

FoM	SRAM	DRAM	Flash NAND	RRAM	FeRAM	PCM	STT-MRAM
Density (bit/chip)	~ 10 MB	~ 10 GB	~ 10 GB	~ 1 GB	~ 1 MB	~ 10 GB	~ 100 MB
Technology feature size F (nm)	16	15	15	16	65	20	22
Cell size (F^2)	> 100	~ 10	~ 5	~ 20	~ 40	~ 20	~ 40
Operation speed (write time)	~ 10 ns	~ 10 ns	~ 100 μs	~ 1 ns	~ 100 ns	----------	----------
Program power/bit	~ 10 pJ	~ 10 pJ	~ 10 nJ	~ 10 pJ	~ 1 pJ	~ 1 nJ	~ 1 pJ
Retention time (y:years)	Volatile	Volatile	> 10 y	> 10 y	> 10 y	> 10 y	> 10 y
Endurance cycles	~ 10^{15}	~ 10^{15}	~ 10^5	~ 10^9	~ 10^{15}	~ 10^8	~ 10^{15}
Price ($/GB)	< 100k	~ 10	~ 1	~ 1k	~ 100K	~ 100	~ 10k

The simple sandwich structure of metal-insulator-metal (MIM) has become the classic structure of two-terminal RRAM devices, which stems from the achievement of Hickmott et al.. Hickmott et al. discovered the resistive switching (RS) performance during the research progress on devices with structures of Al/SiO/Au, Al/AlO_x (Aluminum oxide)/Au, Ta/TaO_x/Au, Zr/ZrO_x/Au, and Ti/TiO_x/Au in 1962 for the first

time. [16] They put primary effort into the RS performance of devices with AlO_x layers and then explained device behaviors with space-charge-limited current (SCLC) theory, dielectric breakdown theory, and oxygen-vacancy drift theory. Although the largest ON/OFF ratio of their device was only ~ 30, this astonishing work provided the technical foundation of the development of RRAM devices, as illustrated in **Fig. 1-2a.** [17-19] In 1971, Chua proposed the concept of 'memristor', which was used to describe the connection between charge and magnetic flux. At that time, it was accepted that one circuit should be determined by four components, including voltage (v), current (i), charge (q), and magnetic flux (φ). The relationship between i and v was defined as a resistor. The connection between q and v was defined as a capacitor while the link between i and φ was an inductor. Chua believed that there should be a component that could be used to describe the relationship between φ and q, which was defined as a memristor. [10, 11] Essentially, the definition of memristor linked the magnetic magnitude of the flux and the time-integral mathematical magnitude of the device voltage. [11] Based on Chua's perspective, the current across a memristor device could change the resistance state of the device and the resistance state would be maintained even without the following current. With the reversed current, the resistance state of the device would transfer back to the previous state, which indicated that the resistance state of a memristor device changed with the change of the current across the device and provided the theoretical foundation of the research of RRAM devices, as illustrated in **Fig. 1-2b.** [20-23] After the 1980s, a large number of researches on RRAM were mainly carried out on the switching mechanism, and various materials were involved. Apart from metal

oxide (MO) reported before, other materials like amorphous silicon, metal sulfide, and polymer also received attention. At the end of the 1990s, the research bottleneck of classical physics and traditional materials science has begun to limit the development of Moore's Law, which indicated that the miniaturization of traditional silicon devices would approach the physical limitation. It is necessary to explore new structures and emerging materials. After 2000, the research of RRAM devices has involved more emerging materials such as perovskite materials, low-dimensional materials, and biological materials. [10, 11, 24-29] Devices based on different materials showed unique differences in electrical properties, which resulted in obvious different interpretations of the switching mechanism. So far, although there are no specific conclusions and standards for the interpretation of switching mechanism, it can be roughly summarized into several classifications: thermal-chemical mechanism (TCM), valance change mechanism (VCM), and electrochemical metallization (ECM), which had been reviewed in my published work. [10, 11] The investigation of TCM theory mainly focuses on the formation and rupture behavior of conductive filament (CF), which is not related to the bipolar or unipolar switching characteristics of the devices. [30-32] For the VCM theory, the main research objectives are defects and vacancies related to oxygen elements in the switching layers, which are always determined by the electrochemical reaction. Compared with the RRAM devices based on TCM, the materials activity variation between top and bottom electrodes is not required for the VCM-based RRAM devices. [33-38] Unlike TCM and VCM, ECM has received the most extensive recognition. The ECM theory is proposed on the basis of the cation migration

phenomenon and electrochemical reaction that occurred in the switching layers, which is always employed to explain the working principles of RRAM devices with active electrodes like silver and copper. [39-45] Among these main mechanism theories, the TCM is also known as the CF mechanism, which included non-metal-vacancy CF and metallic CF. [5, 46-50] In this thesis, I will focus on the switching mechanisms comprising of non-metal-vacancy CF based on oxygen vacancy and metallic CF based on silver (Ag) atom, and related work has been published as journal papers. [51]

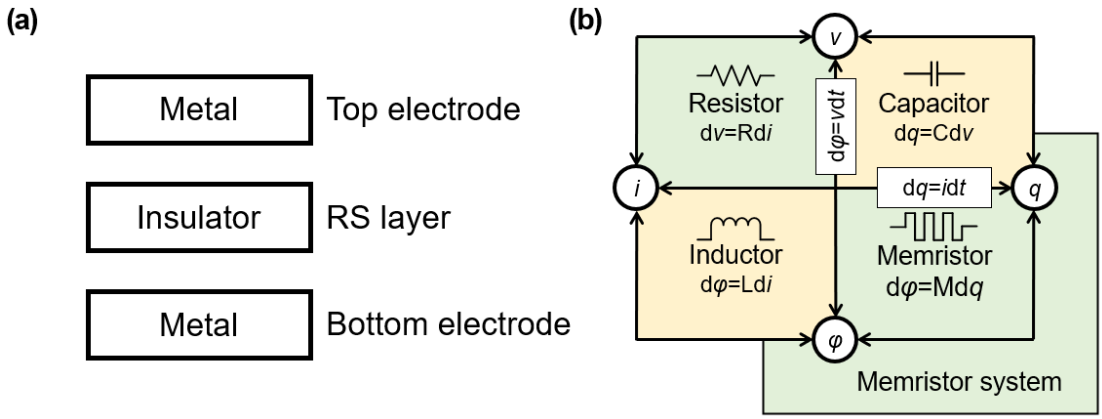

Figure 1-2. (a) Technical and (b) theoretical foundation of the development of RRAM devices. [10, 11, 17-19]

During the developing progress of RRAM devices, apart from the research of physical mechanisms and emerging materials, a growing number of researchers have put their interest into the bionic neuromorphic network circuit of artificial intelligence due to the RS behavior. [51-54] The aim of exploring the bionic neuromorphic network circuit is to emulate the functions and behaviors of the human brain with electronic devices. RRAM devices can emulate the functions of artificial synapses in the neuromorphic network, which can be responsible for connecting the artificial neurons and information storage

units. [52-57] The excellent scalability and the promising prospect of miniaturization are helpful to enhance the artificial synapse density of the bionic neuromorphic network circuit and it is likely to approach a density close to that of the biological synapses in the human brain (~10^{10} / cm^2). [5, 6, 58, 59] Besides, with the low power energy, fast operation speed, and low economic cost, RRAM devices also have a positive influence on program efficiency and cost-effectiveness of the artificial neuromorphic network systems.

1.1.2 FoM of RRAM devices

As mentioned in **Table 1-1**, it is very important to evaluate the electrical and extend the performance of an RRAM device with some primary FoM. As illustrated in **Fig. 1-3**, some primary FoMs have been presented, which are associated with the operation voltages of SET and RESET operations during the RS process. Operation voltage, operation current, ON/OFF ratio, endurance & retention, and operation speed will be introduced in the next section. Works in Chapters 2-4 will also focus on these key parameters and their extensions.

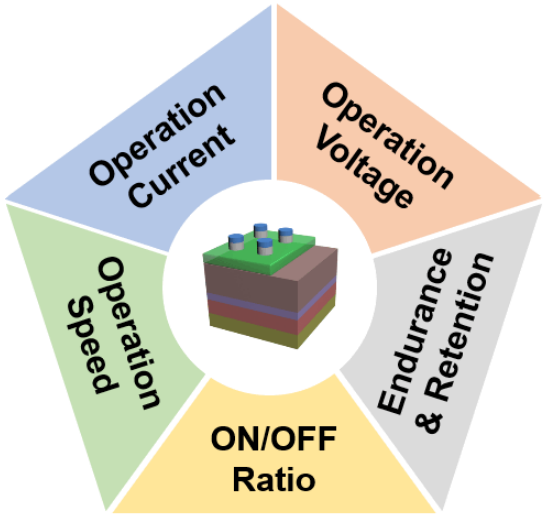

Figure 1-3. Primary FoM in the assessment of the electrical performance of RRAM devices.

Operation Voltage

In general, the SET process is always induced by applying the positive voltage bias onto the top electrode (TE), and then the device switches from the initial high-resistance-state (HRS) to the low-resistance-state (LRS). The voltage when the device has just reached the LRS is defined as the SET voltage (V_{SET}) and the voltage sweeps from 0 V to V_{SET}. After reaching the LRS, the resistance state of the device transfers back to the HRS with the voltage swept from V_{SET} to 0 V. In the practical experimental process, a compliance current (I_{CC}) is always applied to prevent the device from breakdown. Usually, when the current of SET operation reaches I_{CC}, the RRAM device is considered as the LRS. After reaching 0 V, the positive voltage bias is followed by a voltage in the negative direction and induces the RESET process. With the negative voltage sweeps from 0 V to the RESET voltage (V_{RESET}) and then back to 0V, the change of the RRAM device resistance state is demonstrated as HRS-LRS-HRS. In other words, The RRAM device switches from HRS to LRS with the effect of the SET operation

while it switches back to HRS under the effect of the RESET operation. Therefore, two switching modes are defined: unipolar and bipolar modes. As illustrated in **Fig. 1-4**, the unipolar RS mode is only associated with the voltage amplitude and a unipolar device is usually fabricated with the same materials in TE and BE, which is always found in RRAM devices with the symmetric sandwich structure. [19, 60-65] While the bipolar RS mode is controlled by the voltage polarity and the bipolar RRAM devices always demonstrate the asymmetric structure. [6, 10, 11, 19, 60-65] In general, for a bipolar RRAM device, three main forms of structural asymmetry have been noticed. The first one is that there is an obvious difference in materials activity between TE and BE, which is also the most common form. The second one is that the device needs to be formed or initialized with a large voltage before it can enter the steady state of the operation. The last one is that the dielectric layer of the device forms two different interfaces due to plasma oxidation during the working process. [65-70] Compared with the last form, the previous two forms are relatively more common. [64-66]

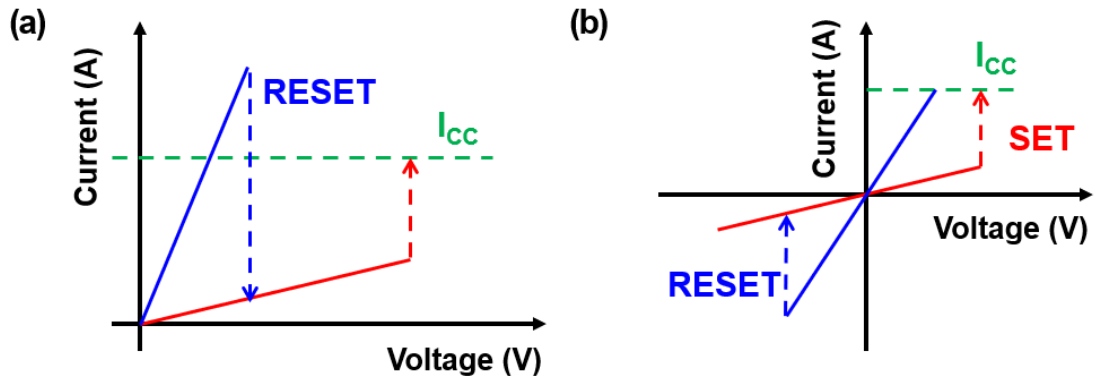

Figure 1-4. (a) Unipolar and (b) bipolar switching modes of RRAM devices.

Operation Current

For the same RRAM device, there is an inseparable relationship between operation voltage and operation current. As mentioned before, I_{CC} in the SET process is an effective barrier to the normal operation of the device. For the RESET process, the operation current is usually defined as the maximum value that the device switches from LRS to HRS. [61, 63, 67] On the one hand, the greater the operation current flowing through the device, the easier it is for the device to fail. On the other hand, the power consumption of the device may also increase unnecessarily due to the increase of the operation current. [6-8] Therefore, the smaller the operation current can reduce the power consumption of an RRAM device while ensuring stable operation of the device.

ON/OFF Ratio

The ON/OFF ratio is also called the switching ratio, which is defined as the ratio value between a high resistance value and a low resistance value read at the same voltage. [19, 51, 53] Compared with conventional memory devices like flash and DRAM, the larger ON/OFF ratio is always observed on RRAM devices. The larger the ON/OFF ratio, the better it is for the external circuit to identify the storage state of the RRAM device. In general, the ON/OFF ratio of an RRAM device is larger than 10^3, the highest one can be up to 10^{11}. [19, 51, 53, 61-63] The larger ON/OFF ratio not only increases the probability of multi-level resistance or conduce states but also provides great potential for the application of artificial intelligence hardware.

Endurance and Retention

Endurance (write endurance) and retention (data retention) properties are always compared together to evaluate the stability and reliability of an RRAM device. [48, 52, 61] Endurance is defined as the cycle number of the RRAM device switches between HRS and LRS. Values of high and low resistance can maintain a stable state to a certain extent, respectively. The endurance cycles are also considered as the number of times the RRAM device can be erased and written repeatedly. [63-65] Compared with flash memory, the endurance cycles of the RRAM devices have been more than 10^6 and the cycles of the RRAM devices based on TaO_x materials fabricated by SAMSUNG have been over 10^{12}. [19, 61, 63-65] Compared with the endurance property that focuses on the cycle number of erasing and writing operations, the research on the retention performance pays more attention to the time that the device can maintain resistance values at LRS and HRS, respectively. Generally, the stable states of HRS and LRS values of the device are evaluated by the distribution statistics of the corresponding resistance values. [68] The retention time is one of the most vital parameters to assess the non-volatility of an RRAM device. Theoretically, the retention time should be over 10 years even the environment temperature at 85°C. [53-55] During the experimental process, it is hard to continuously measure a device with 10 years. Hence, the practical retention time is obtained by extension of the measurement data or by estimating the failure time of the device after being subjected to an aging process with a high temperature.

Operation Speed

The speed of erasing and writing operations is used to evaluate whether an RRAM device has the ability of fast-data-processing. [57, 63, 68] Currently, the operation speed of a DRAM device is lower than 10 ns while that of a flash memory device is over 10 μs, which results in that the DRAM is usually selected as the internal memory while the flash memory is chosen as the external memory of the computer. [5, 7, 16] At present, the operation speed of some RRAM devices have been less than 10 ns, or even as fast as ~1ns, which has exceeded the operation speed of DRAM. [60, 68] Williams et al. from HP Lab have reported that their RRAM device based on TaO_x materials could complete the SET and RESET operations within 105 ps and 120 ps, respectively, which revealed the outstanding potential of RRAM devices as the high-speed memory. [61, 62, 64] Here, an FoM comparison among RRAM devices with various materials were presented in **Table 1-2** below.

Table 1-2. FoM comparison among RRAM devices with various materials

Structure	Switching mode	Thickness (nm)	$V_{Forming}$ (V)	V_{SET} (V)	V_{RESET} (V)	ON/OFF Ratio	Endurance (cycle)	Retention (s)	Ref
Ni/AlO_x/Pt	bipolar	~40	Free	~1.0	~-1.0	~10^3	>150	>10^4	[71]
TaN/HfO_2/Al_2O_3/ITO	bipolar	~6	~4.5	~1.5	~-1.0	~10^2	>100	>2x10^3	[72]
Ti/IL-NiO/Pt	bipolar	~50	Free	~0.5	~-1.5	~10^3	>1300	>10^4	[73]
FeNi/Al_2O_3/NiO/Pt	bipolar	~180	~4.07	~6.0	~-5.0	~10^3	>100	>10^4	[74]
Au/TiO_x/TiO_y/Au	bipolar	~50	~5.62	~1.0	~-2.0	~10^2	N. A.	N. A.	[75]
Ni/$SiGeO_x$/TiO_y/TiN	bipolar	~25	Free	~3.0	~-2.5	~10^3	>10^4	>10^5	[76]
Ti/HfO_2/TiN	bipolar	~15	~6.5	~1.0	~-0.8	~10	N. A.	N. A.	[77]
Pt/Hf/HfO_2/TiN	bipolar	~20	Free	~0.8	~-1.5	~10^2	N. A.	>10^6	[78]
Pt/Ta/HfO_2/TiN	bipolar	~20	Free	~0.8	~-1.8	~10^2	N. A.	>10^4	[78]

Pt/Al:HfO_2/TiN	bipolar	~9	~2.3	~2.0	~-2.0	~10^4	>100	>10^4	[79]
TiN/ZnO/TiN	bipolar	~9	~4.2	~1.0	~-1.0	~10	240	N. A.	[80]
TiN/Al_2O_3/ZnO/Al_2O_3/TiN	bipolar	~15	~5.0	~1.0	~-1.0	~10^2	>10^4	>10^4	[80]
ITO/ZrO_2/Ag	bipolar	~50	N. A.	~5.0	~-15.0	~10^5	>100	>10^4	[81]
Pt/N:ZrO_2/TiN	bipolar	~25	~3.6	~0.5	~-1.0	~10^2	N. A.	N. A.	[82]
Ag/SiO_2/Pt	bipolar	~80	N. A.	~0.5	~-2.0	~10^6	>40	>2x10^3	[39]
ITO/$LaAlO_3$/ITO	bipolar	~30	~3.2	~3.0	~-3.0	~10^2	>100	N. A.	[83]
Cu/Cu:$LaAlO_3$/Pt	bipolar	~10	~ 7.0	~2.0	~-2.0	~10^3	>110	>10^4	[84]
GNR/$SrTiO_3$/GNR	bipolar	~50	N. A.	~2.0	~-3.0	~10	>200	>10^4	[85]
Pt/GO/PCMO/Pt	bipolar	~25	Free	~1.0	~-1.0	~10^2	>150	>10^4	[86]
Pt/$BiFeO_3$/Pt	unipolar	~200	N. A.	~5.0	~-15.0	N. A.	N. A.	N. A.	[87]
Ag/ZnO/$BiFeO_3$/ZnO/Ag	bipolar	~270	Free	~2.0	~-2.0	~10	N. A.	N. A.	[88]
Ag/Ag_2Se/MnO/Au	bipolar	~40	Free	~0.8	~-0.6	~10^2	>800	>10^4	[89]
TiN/SLG/HfO_2/Pt	bipolar	~35	~5.0	~2.0	~-3.0	~10^2	>120	>10^6	[90]
Ti/MoS_2-rGO/ITO	bipolar	~60	Free	~0.5	~-0.4	~10	>200	>10^4	[91]
Au/$CsPbBr_3$/ITO	bipolar	N, A.	Free	~1.0	~-1.0	~10^4	N. A.	>1200	[92]

1.2 Review of solution-processed techniques

Generally, the performance of an RRAM device is always determined by the characteristic of the RS layer, which is associated with the fabrication methods. In the past several decades, some conventional fabrication methods like atomic layer deposition (ALD) and chemical vapor deposition (CVD) have been applied to the fabrication process of RS thin film layers with various materials. [8, 10, 11] RRAM devices

fabricated with ALD and CVD have demonstrated stable electrical performance. [93-96] At present, some emerging fabrication methods have received extensive attention, including liquid-phase exfoliation (LPE), nucleation & growth, and solution-processed (SP) techniques. [11] Methods like and nucleation & growth are mainly utilized to develop graphene and related materials while SP techniques are more universal for most materials, including MO, perovskites, 0D quantum dot (QD), 1D nanowire (NW), 2D nanosheet, organics, and biopolymer materials. [97-105] RS thin film layers fabricated with SP methods have benefits like excellent extensibility, outstanding compatibility with external hardware devices, low economic fabrication cost, high fabrication efficiency, and high tolerance to the manufacturing environment. [49, 106-108] Besides, compared with RS thin films fabricated with conventional methods like ALD and CVD, RS thin films fabricated through SP methods require much lower temperature and less energy consumption during the manufacturing process, which indicates the higher cost-effectiveness while revealing the environment friendliness. [106-108] Currently, SP techniques have been divided into two primary categories: coating and printing. Coating SP techniques including spin-coating, dip-coating, and drop-casting have received more interest due to the ease of operation, the mature experience of the film-forming process, and controllable quality of formed films. [11, 61, 106] While printing SP techniques comprising of inkjet printing, aerosol jet printing, screen printing, and electrohydrodynamic (EHD) printing might be relatively emerging. [49] Also, printing SP techniques have advantages like low manufacturing cost, low demand for raw materials, and ease of pattern deposition. [49, 106, 108] In **Table 1-3**, a specific comparison

among several coating SP techniques has been presented, which was also summarized in my published review. [10, 11, 49, 106-108]

Table 1-3. Specific comparison among several main coating SP techniques

Item	Spin-coating	Drop-casting	Dip-coating
Fabrication cost	Low	Low	High
Fabrication equipment	Spin coater, syringe	Dropper	Dip coater
Fabrication time	< 1 hour	< 1 hour	> 2 hours
Dielectric performance	Uniform/thick	Heterogeneous/thick	Uniform/thick
Device performance	Retention time > 10^4 s	Retention time < 10^4 s	Retention time < 10^4 s
	Endurance cycles > 100	Endurance cycles < 100	Endurance cycles < 100

In this thesis, all RRAM devices with SP RS layers utilize the most popular spin-coating method. Before the thin film deposition, the precursor solution comprising of various solutes and solvents is prepared. After the spin-coating process, the semi-finished device with the spin-coated precursor solution is annealed at the desired temperature. Hence, the thickness of the formed thin film and the device performance is influenced by the concentration/viscosity of the precursor solution, the speed of the spin-coating operation, and the annealed temperature, which will be discussed in the following chapters.

1.3 Objectives of the thesis

As discussed before, the great potential of RRAM devices and the benefits of SP methods have been revealed. It is worth considering using SP methods to realize the RS behavior of dielectric layers. My published review has presented the material classifications of all RS layers, including organics (PVK-C_{60}, PVA, and protein) and

inorganics (AlO_x, $CsPbBr_3$, and graphene oxide). [10, 11, 16, 24, 25] Among various materials, the RS behavior was observed in the inorganic MO materials for the first time. Also, many researchers have proved the reliability and stability of RRAM devices with MO (such as AlO_x, HfO_x, NiO_x, ZnO, and TiO_x) RS layers, and most devices worked with MO RS layers fabricated with ALD methods. Besides, for two devices with the total same materials but different fabrication methods (SP and ALD methods) for the RS layer, the device with the SP RS layer always demonstrated a larger ON/OFF ratio when the energy consumption of these two devices are very similar. [16, 61, 62]

In this thesis, the AlO_x materials were chosen as the candidate of the RS layers and the AlO_x layers were fabricated with the SP spin-coating method. As a compound with high hardness, AlO_x has got attention before due to its application as the gate insulator. The benefits like chemical corrosion resistance, high-temperature tolerance, a high dielectric constant of ~ 8, and a wide bandgap of ~ 8.9 eV demonstrated excellent chemical and physical properties of AlO_x materials. [109-113] Some researchers proved the good stability and compatibility of AlO_x with Si or Pt substrate under a high thermal environment. Besides, due to the better elasticity and toughness, AlO_x materials have been also utilized in electronic devices to alleviate the impact of the external vibration and stress environment. These properties have indicated the appropriateness of selecting AlO_x as the RS layer in an RRAM device.

In **Chapter 2**, the RRAM device with the structure of Nickel (Ni)/SP-AlO_x/Platinum

(Pt) and TiN/SP-AlO_x/Pt were fabricated to investigate the electrical performance and related papers have been published. [110, 112] The objective of this chapter was to explore a probable fabrication environment for RRAM devices with SP-AlO_x layers. For the Ni/SP-AlO_x/Pt device, three main kinds of SP-AlO_x-based RRAM samples were investigated and SP-AlO_x layers were annealed at the different desired temperatures (225 °C, 250 °C, and 275 °C). All devices demonstrated bipolar RS performance. However, performance variation was also obtained due to the variation of the annealing temperature of RS layers. The Ni/SP-AlO_x/Pt device with the 250°C annealed SP-AlO_x layer displayed excellent RS behavior with the V_{SET} lower than 1.5 V and the ON/OFF ratio larger than 10^2. The retention time was longer than 10^4 s and the endurance cycle was over 150. Related results indicated that the 250°C annealing temperature might be one of the most appropriate fabrication conditions for SP-AlO_x RS layers. In addition, the TiN/SP-AlO_x/Pt RRAM devices were manufactured to compare with Ni/SP-AlO_x/Pt devices. The fabrication conditions of TiN/SP-AlO_x/Pt RRAM devices for each sample were as same as that of Ni/SP-AlO_x/Pt devices. The investigation of TiN/SP-AlO_x/Pt devices also verified the excellent performance of devices with the 250°C annealed SP-AlO_x layers. In addition, the variation between Ni and TiN revealed that the work function difference ($\Delta\Phi_M$) between TE and BE could influence the electrical performance of the RRAM devices. [110, 112]

In **Chapter 3**, with the basis of research on RRAM devices with a single SP-AlO_x layer, I explored the electrical performance improvement of RRAM devices with stacked SP

RS layers and related results have been published. [51] Before the research on RRAM devices with stacked SP RS layers, I characterized some samples with single SP RS layers in terms of various materials, including gallium oxide (GaO_x), indium oxide (InO_x), and graphene oxide (GO). After the comprehensive comparison and consideration, the SP-GaO_x layer was selected as the upper part of the total SP RS layers, which formed the stacked SP-GaO_x/SP-AlO_x layer. Besides, silver (Ag) was chosen as the TE instead of Ni and TiN. Related results with improvement operations indicated that the Ag/SP-GaO_x/SP-AlO_x/ITO device displayed the bipolar RS behavior with a lower operation voltage of ~ ±0.6 V, a larger ON/OFF ratio of ~ 2×10^4, a longer retention time of ~ 2×10^4 s, and more retention cycles over 200. [51]

The improved electrical performance indicated that it was easier to explore the potential of RRAM devices with SP RS layers as the artificial synaptic devices. Therefore, in **Chapter 4**, published investigation and discussion about the artificial synaptic performance of the Ag/SP-GaO_x/SP-AlO_x/ITO device were presented. [51, 114] During the measurement of current-voltage (I-V) for the device, the multiple-state RS performance was obtained, which indicated the capability of multi-level storage and multi-level conductance states at the same time. The conductance change with multiple states is always considered as the foundation of biomimetic synaptic behavior. Then, the measurement of pulse response was carried out, which resulted in the typical excitatory postsynaptic current (EPSC) and emulated the basic function of an artificial synapse. The device also demonstrated synaptic response variation to the input pulses

with different pulse magnitudes and pulse widths. After that, the long-term plasticity of the Ag/SP-GaO_x/SP-AlO_x/ITO RRAM device was obtained, including the long-term potentiation (LTP) and long-term depression (LTD). With the classic long-term plasticity, an Ag/SP-GaO_x/SP-AlO_x/ITO RRAM matrix with the desired shape was used to emulate the biomimetic transition from short-term memory (STM) to long-term memory (LTM). At last, an artificial neuron network (ANN) was established with key parameters from the synaptic performance of the RRAM device and then completed a pattern recognition process on Arabic numbers from 0 to 9. The average value of the recognition accuracy was around 90% and the highest one was up to 96%. [51, 114]

In **Chapter 5**, the final conclusions were presented and related discussion on the outlook and development of artificial synaptic electronics was included.

1.4 References

[1] G. Choe and S. Yu, "Variability Study of Ferroelectric Field-Effect Transistors towards 7nm Technology Node," *IEEE Journal of the Electron Devices Society,* pp. 1-1, 2021.

[2] Y.-K. Liang, J.-S. Wu, C.-Y. Teng, H.-L. Ko, Q.-H. Luc, C.-J. Su, E.-Y. Chang, and C.-H. Lin, "Demonstration of Highly Robust 5 nm $Hf_{0.5}Zr_{0.5}O_2$ Ultra-Thin Ferroelectric Capacitor by Improving Interface Quality," *IEEE Electron Device Letters,* vol. 42, no. 9, pp. 1299-1302, 2021.

[3] V. B. Sreenivasulu and V. Narendar, "Characterization and optimization of junctionless gate-all-around vertically stacked nanowire FETs for sub-5 nm technology nodes," *Microelectronics Journal,* pp. 105214(1-32), 2021.

[4] J. Schon, T. Niewelt, D. Mu, S. Maus, A. Wolf, J. D. Murphy, and M. C. Schubert, "Experimental and Theoretical Study of Oxygen Precipitation and the Resulting Limitation of Silicon Solar Cell Wafers," *IEEE Journal of Photovoltaics,* vol. 11, no. 2, pp. 289-297, 2021.

[5] S. Dai, Y. Zhao, Y. Wang, J. Zhang, L. Fang, S. Jin, Y. Shao, and J. Huang,

"Recent Advances in Transistor-Based Artificial Synapses," *Advanced Functional Materials,* vol. 29, no. 42, pp. 1903700(1-23), 2019.

[6] H. Han, H. Yu, H. Wei, J. Gong, and W. Xu, "Recent Progress in Three-Terminal Artificial Synapses: From Device to System," *Small,* vol. 15, no. 32, pp. e1900695(1-17), Aug 2019.

[7] C. Wan, P. Cai, M. Wang, Y. Qian, W. Huang, and X. Chen, "Artificial Sensory Memory," *Adv Mater,* vol. 32, no. 15, pp. e1902434(1-22), Apr 2020.

[8] H. Xu, L. Yin, C. Liu, X. Sheng, and N. Zhao, "Recent Advances in Biointegrated Optoelectronic Devices," *Adv Mater,* vol. 30, pp. e1800156(1-22), May 28 2018.

[9] N. Gupta, A. Makosiej, H. Shrimali, A. Amara, A. Vladimirescu, and C. Anghel, "Tunnel FET Negative-Differential-Resistance Based 1T1C Refresh-Free-DRAM, 2T1C SRAM and 3T1C CAM," *IEEE Transactions on Nanotechnology,* vol. 20, pp. 270-277, 2021.

[10] Z. Shen, C. Zhao, Y. Qi, W. Xu, Y. Liu, I. Z. Mitrovic, L. Yang, and C. Zhao, "Advances of RRAM Devices: Resistive Switching Mechanisms, Materials and Bionic Synaptic Application," *Nanomaterials (Basel),* vol. 10, no. 8, pp. 1437(1-31), Jul 23 2020.

[11] Z. Shen, C. Zhao, Y. Qi, I. Z. Mitrovic, L. Yang, J. Wen, Y. Huang, P. Li, and C. Zhao, "Memristive Non-Volatile Memory Based on Graphene Materials," *Micromachines (Basel),* vol. 11, no. 4, pp. 341(1-26), Mar 25 2020.

[12] E. Garzón, R. De Rose, F. Crupi, L. Trojman, A. Teman, and M. Lanuzza, "Relaxing non-volatility for energy-efficient DMTJ based cryogenic STT-MRAM," *Solid-State Electronics,* vol. 184, pp. 108090(1-5), 2021.

[13] E. S. John Pimo, V. Ashok, T. Logeswaran, and D. Sri Sai Satyanarayana, "A comparative performance analysis of phase change memory as main memory and DRAM," *Materials Today: Proceedings,* vol. In press, 2021.

[14] T. T. Ken Takeuchi, and Toru Tanzawa, "A multipage cell architecture for high-speed programming multilevel NAND flash memories," *IEEE JOURNAL OF SOLID-STATE CIRCUITS,* vol. 33, no. 8, pp. 1228-1238, 1998.

[15] D. Zhang, D. Chong, J. Yan, and B. Zhao, "Experimental study on static flash evaporation of aqueous NaCl solution at different flash speed: Heat transfer characteristics," *International Journal of Heat and Mass Transfer,* vol. 65, pp. 584-591, 2013.

[16] A. Sawa, "Resistive switching in transition metal oxides," *Materials Today,* vol. 11, no. 6, pp. 28-36, 2008.

[17] J. S. Lee, S. Lee, and T. W. Noh, "Resistive switching phenomena: A review of statistical physics approaches," *Applied Physics Reviews,* vol. 2, no. 3, pp. 031303(1-58), 2015.

[18] C. Schindler, G. Staikov, and R. Waser, "Electrode kinetics of Cu–SiO_2-based resistive switching cells: Overcoming the voltage-time dilemma of electrochemical metallization memories," *Applied Physics Letters,* vol. 94, no. 7, pp. 072109(1-4), 2009.

[19] F. Pan, C. Chen, Z.-s. Wang, Y.-c. Yang, J. Yang, and F. Zeng, "Nonvolatile

resistive switching memories-characteristics, mechanisms and challenges," *Progress in Natural Science: Materials International,* vol. 20, pp. 1-15, 2010.

[20] S. C. Sungho Kim, and Wei Lu, "Comprehensive Physical Model of Dynamic Resistive Switching in an Oxide Memristor," *ACS Nano,* vol. 8, no. 3, pp. 2369–2376, 2014.

[21] F. Gul and H. Efeoglu, "ZnO and ZnO_{1-x} based thin film memristors: The effects of oxygen deficiency and thickness in resistive switching behavior," *Ceramics International,* vol. 43, no. 14, pp. 10770-10775, 2017.

[22] G. A. Patterson, P. I. Fierens, and D. F. Grosz, "On the beneficial role of noise in resistive switching," *Applied Physics Letters,* vol. 103, no. 7, pp. 074102(1-5), 2013.

[23] E. Miranda and J. Sune, "Memristive State Equation for Bipolar Resistive Switching Devices Based on a Dynamic Balance Model and Its Equivalent Circuit Representation," *IEEE Transactions on Nanotechnology,* vol. 19, pp. 837-840, 2020.

[24] L. Shao, H. Wang, Y. Yang, Y. He, Y. Tang, H. Fang, J. Zhao, H. Xiao, K. Liang, M. Wei, W. Xu, M. Luo, Q. Wan, W. Hu, T. Gao, and Z. Cui, "Optoelectronic Properties of Printed Photogating Carbon Nanotube Thin Film Transistors and Their Application for Light-Stimulated Neuromorphic Devices," *ACS Appl Mater Interfaces,* vol. 11, no. 12, pp. 12161, Mar 27 2019.

[25] Y. Sun, L. Qian, D. Xie, Y. Lin, M. Sun, W. Li, L. Ding, T. Ren, and T. Palacios, "Photoelectric Synaptic Plasticity Realized by 2D Perovskite," *Advanced Functional Materials,* vol. 29, no. 28, pp. 1902538, 2019.

[26] G. Gou, J. Sun, C. Qian, Y. He, L.-a. Kong, Y. Fu, G. Dai, J. Yang, and Y. Gao, "Artificial synapses based on biopolymer electrolyte-coupled SnO2nanowire transistors," *Journal of Materials Chemistry C,* vol. 4, no. 47, pp. 11110, 2016.

[27] H. Ling, D. A. Koutsouras, S. Kazemzadeh, Y. van de Burgt, F. Yan, and P. Gkoupidenis, "Electrolyte-gated transistors for synaptic electronics, neuromorphic computing, and adaptable biointerfacing," *Applied Physics Reviews,* vol. 7, no. 1, pp. 011307, 2020.

[28] A. Younis, C. H. Lin, X. Guan, S. Shahrokhi, C. Y. Huang, Y. Wang, T. He, S. Singh, L. Hu, J. R. D. Retamal, J. H. He, and T. Wu, "Halide Perovskites: A New Era of Solution-Processed Electronics," *Adv Mater,* vol. 33, no. 23, pp. e2005000(1-34), Jun 2021.

[29] N. Liu, Y. Cao, Y. L. Zhu, Y. J. Wang, Y. L. Tang, B. Wu, M. J. Zou, Y. P. Feng, and X. L. Ma, "Spinodal Decomposition-Driven Endurable Resistive Switching in Perovskite Oxides," *ACS Appl Mater Interfaces,* vol. 13, no. 26, pp. 31001-31009, Jul 7 2021.

[30] L. X. Xinxin Zhang, Hui Zhang, Jian Liu, Dingwen Tan, Liangliang Chen, Zhongyuan Ma, "Effect of Joule Heating on Resistive Switching Characteristic in AlO_x Cells Made by Thermal Oxidation Formation," *Nanoscale Research Letters,* vol. 19, pp. 3229-1-3229-19, 2020.

[31] T. Tsuruoka, T. Hasegawa, K. Terabe, and M. Aono, "Conductance quantization and synaptic behavior in a Ta_2O_5-based atomic switch," *Nanotechnology,* vol.

23, no. 43, pp. 435705-435711, Nov 2 2012.

[32] P. Sun, L. Li, N. Lu, Y. Li, M. Wang, H. Xie, S. Liu, and M. Liu, "Physical model of dynamic Joule heating effect for reset process in conductive-bridge random access memory," *Journal of Computational Electronics,* vol. 13, no. 2, pp. 432-438, 2014.

[33] T. Zhang, X. Ou, W. Zhang, J. Yin, Y. Xia, and Z. Liu, "High-k-rare-earth-oxide Eu_2O_3 films for transparent resistive random access memory (RRAM) devices," *Journal of Physics D: Applied Physics,* vol. 47, no. 6, pp. 065302-065308, 2014.

[34] J. L. Kun-Ji Chen, Yuefei Wang, Huafeng Yang, Zhongyuan Ma, Xinfan Huang, "VCM Conductive defect states based filament in MOM structure RRAM," *IEEE Electronic Device Letter,* vol. 9, pp. 1-4, 2018.

[35] D. H. Kwon, K. M. Kim, J. H. Jang, J. M. Jeon, M. H. Lee, G. H. Kim, X. S. Li, G. S. Park, B. Lee, S. Han, M. Kim, and C. S. Hwang, "Atomic structure of conducting nanofilaments in TiO_2 resistive switching memory," *Nat Nanotechnol,* vol. 5, no. 2, pp. 148-153, Feb 2010.

[36] W. Xue, G. Liu, Z. Zhong, Y. Dai, J. Shang, Y. Liu, H. Yang, X. Yi, H. Tan, L. Pan, S. Gao, J. Ding, X. H. Xu, and R. W. Li, "A 1D Vanadium Dioxide Nanochannel Constructed via Electric-Field-Induced Ion Transport and its Superior Metal-Insulator Transition," *Adv Mater,* vol. 29, no. 39, pp. 1702162(1)-1702162(9), Oct 2017.

[37] S. Lee, J. Sohn, Z. Jiang, H. Y. Chen, and H. S. Philip Wong, "Metal oxide-resistive memory using graphene-edge electrodes," *Nat Commun,* vol. 6, pp. 8407-8413, Sep 25 2015.

[38] S. Munjal and N. Khare, "Valence Change Bipolar Resistive Switching Accompanied With Magnetization Switching in $CoFe_2O_4$ Thin Film," *Sci Rep,* vol. 7, no. 1, pp. 12427-12436, Sep 29 2017.

[39] L. F. L. D. Yu, B. Chen, F.F. Zhang, B. Gao, Y.H. Fu, X.Y. Liu, J.F. Kang, X. Zhang, "Multilevel resistive switching characteristics in Ag/SiO_2/Pt RRAM devices," *IEEE Electron Device Letters,* vol. 11, pp. 1-4, 2011.

[40] T. Tsuruoka, K. Terabe, T. Hasegawa, and M. Aono, "Forming and switching mechanisms of a cation-migration-based oxide resistive memory," *Nanotechnology,* vol. 21, no. 42, pp. 425205-425213, Oct 22 2010.

[41] T. Guo, B. Sun, Y. Zhou, H. Zhao, M. Lei, and Y. Zhao, "Overwhelming coexistence of negative differential resistance effect and RRAM," *Phys Chem Chem Phys,* vol. 20, no. 31, pp. 20635-20640, Aug 8 2018.

[42] Q. L. Shi-Bing Long, Hang-Bing Lv, Ying-Tao Li, Yan Wang, Sen Zhang, Wen-Tai Lian and Ming Liu, "Resistive switching mechanism of Cu doped ZrO_2-based RRAM," *IEEE Electronic Device Letter,* vol. 5, pp. 1-4, 2010.

[43] S. Long, Q. Liu, H. Lv, Y. Li, Y. Wang, S. Zhang, W. Lian, K. Zhang, M. Wang, H. Xie, and M. Liu, "Resistive switching mechanism of Ag/ZrO_2:Cu/Pt memory cell," *Applied Physics A,* vol. 102, no. 4, pp. 915-919, 2011.

[44] F. Yuan, S. Shen, Z. Zhang, L. Pan, and J. Xu, "Interface-induced two-step RESET for filament-based multi-level resistive memory," *Superlattices and Microstructures,* vol. 91, pp. 90-97, 2016.

[45] S. Gao, F. Zeng, C. Chen, G. Tang, Y. Lin, Z. Zheng, C. Song, and F. Pan, "Conductance quantization in a Ag filament-based polymer resistive memory," *Nanotechnology,* vol. 24, no. 33, pp. 335201-335208, Aug 23 2013.

[46] L. Chen, C. Li, T. Huang, Y. Chen, S. Wen, and J. Qi, "A synapse memristor model with forgetting effect," *Physics Letters A,* vol. 377, no. 45-48, pp. 3260, 2013.

[47] M. Kumar, S. Abbas, and J. Kim, "All-Oxide-Based Highly Transparent Photonic Synapse for Neuromorphic Computing," *ACS Appl Mater Interfaces,* vol. 10, no. 40, pp. 34370, Oct 10 2018.

[48] M. Lee, W. Lee, S. Choi, J. W. Jo, J. Kim, S. K. Park, and Y. H. Kim, "Brain-Inspired Photonic Neuromorphic Devices using Photodynamic Amorphous Oxide Semiconductors and their Persistent Photoconductivity," *Adv Mater,* vol. 29, no. 28, pp. 1700951, Jul 2017.

[49] K. Lu, X. Li, Q. Sun, X. Pang, J. Chen, T. Minari, X. Liu, and Y. Song, "Solution-processed electronics for artificial synapses," *Materials Horizons,* vol. 8, no. 2, pp. 447-470, 2021.

[50] Y. Zhai, J.-Q. Yang, Y. Zhou, J.-Y. Mao, Y. Ren, V. A. L. Roy, and S.-T. Han, "Toward non-volatile photonic memory: concept, material and design," *Materials Horizons,* vol. 5, no. 4, pp. 641-654, 2018.

[51] Z. Shen, C. Zhao, T. Zhao, W. Xu, Y. Liu, Y. Qi, I. Z. Mitrovic, L. Yang, and C. Z. Zhao, "Artificial Synaptic Performance with Learning Behavior for Memristor Fabricated with Stacked Solution-Processed Switching Layers," *ACS Applied Electronic Materials,* vol. 3, no. 3, pp. 1288-1300, 2021.

[52] S. Park, J. Noh, M. L. Choo, A. M. Sheri, M. Chang, Y. B. Kim, C. J. Kim, M. Jeon, B. G. Lee, B. H. Lee, and H. Hwang, "Nanoscale RRAM-based synaptic electronics: toward a neuromorphic computing device," *Nanotechnology,* vol. 24, no. 38, pp. 384009(1-7), Sep 27 2013.

[53] K. Moon, S. Lim, J. Park, C. Sung, S. Oh, J. Woo, J. Lee, and H. Hwang, "RRAM-based synapse devices for neuromorphic systems," *Faraday Discuss,* vol. 213, pp. 421-451, Feb 18 2019.

[54] V. Milo, C. Zambelli, P. Olivo, E. Pérez, M. K. Mahadevaiah, O. G. Ossorio, C. Wenger, and D. Ielmini, "Multilevel HfO_2-based RRAM devices for low-power neuromorphic networks," *APL Materials,* vol. 7, no. 8, pp. 081120(1-11), 2019.

[55] T. Li, H. Yu, Z. Xiong, Z. Gao, Y. Zhou, and S.-T. Han, "2D oriented covalent organic frameworks for alcohol-sensory synapses," *Materials Horizons,* vol. 8, no. 7, pp. 2041-2049, 2021.

[56] J. Zhou, H. Feng, Y. Wang, Q. Sun, Y. Liu, X. Liu, L. Zhang, and S. Cao, "Flexible random resistive access memory devices with ferrocene–rGO nanocomposites for artificial synapses," *Journal of Materials Chemistry C,* vol. 9, no. 17, pp. 5749-5757, 2021.

[57] C. Mahata, H. Algadi, M. Ismail, D. Kwon, and S. Kim, "Controlled multilevel switching and artificial synapse characteristics in transparent HfAlO-alloy based memristor with embedded TaN nanoparticles," *Journal of Materials Science & Technology,* vol. 95, pp. 203-212, 2021.

[58] Y. Liu, W. Huang, X. Wang, R. Liang, J. Wang, B. Yu, T.-L. Ren, and J. Xu, "A Hybrid Phototransistor Neuromorphic Synapse," *IEEE Journal of the Electron Devices Society,* vol. 7, pp. 13-17, 2019.

[59] M. Kimura, Y. Koga, H. Nakanishi, T. Matsuda, T. Kameda, and Y. Nakashima, "In–Ga–Zn–O Thin-Film Devices As Synapse Elements in a Neural Network," *IEEE Journal of the Electron Devices Society,* vol. 6, pp. 100-105, 2018.

[60] S. Kim, H. Y. Jeong, S. K. Kim, S. Y. Choi, and K. J. Lee, "Flexible memristive memory array on plastic substrates," *Nano Lett,* vol. 11, no. 12, pp. 5438-42, Dec 14 2011.

[61] H. S. P. Wong, H.-Y. Lee, S. Yu, Y.-S. Chen, Y. Wu, P.-S. Chen, B. Lee, F. T. Chen, and M.-J. Tsai, "Metal–Oxide RRAM," *Proceedings of the IEEE,* vol. 100, no. 6, pp. 1951-1970, 2012.

[62] X. Hong, D. J. Loy, P. A. Dananjaya, F. Tan, C. Ng, and W. Lew, "Oxide-based RRAM materials for neuromorphic computing," *Journal of Materials Science,* vol. 53, no. 12, pp. 8720-8746, 2018.

[63] V. Gupta, S. Kapur, S. Saurabh, and A. Grover, "Resistive Random Access Memory: A Review of Device Challenges," *IETE Technical Review,* vol. 37, no. 4, pp. 377-390, 2019.

[64] H. Wang and X. Yan, "Overview of Resistive Random Access Memory (RRAM): Materials, Filament Mechanisms, Performance Optimization, and Prospects," *physica status solidi (RRL) – Rapid Research Letters,* vol. 13, no. 9, pp. 1900073(1-12), 2019.

[65] Y. Guo, H. Wu, B. Gao, and H. Qian, "Unsupervised Learning on Resistive Memory Array Based Spiking Neural Networks," *Front Neurosci,* vol. 13, pp. 812(1-16), 2019.

[66] T. S. Lee, N. J. Lee, H. Abbas, H. H. Lee, T.-S. Yoon, and C. J. Kang, "Compliance Current-Controlled Conducting Filament Formation in Tantalum Oxide-Based RRAM Devices with Different Top Electrodes," *ACS Applied Electronic Materials,* vol. 2, no. 4, pp. 1154-1161, 2020.

[67] B. Mu, H.-H. Hsu, C.-C. Kuo, S.-T. Han, and Y. Zhou, "Organic small molecule-based RRAM for data storage and neuromorphic computing," *Journal of Materials Chemistry C,* vol. 8, no. 37, pp. 12714-12738, 2020.

[68] F. Zahoor, T. Z. Azni Zulkifli, and F. A. Khanday, "Resistive Random Access Memory (RRAM): an Overview of Materials, Switching Mechanism, Performance, Multilevel Cell (mlc) Storage, Modeling, and Applications," *Nanoscale Res Lett,* vol. 15, no. 1, pp. 90, Apr 22 2020.

[69] M. M. Rehman, H. Rehman, J. Z. Gul, W. Y. Kim, K. S. Karimov, and N. Ahmed, "Decade of 2D-materials-based RRAM devices: a review," *Sci Technol Adv Mater,* vol. 21, no. 1, pp. 147-186, 2020.

[70] S. Yu, W. Shim, X. Peng, and Y. Luo, "RRAM for Compute-in-Memory: From Inference to Training," *IEEE Transactions on Circuits and Systems I: Regular Papers,* vol. 68, no. 7, pp. 2753-2765, 2021.

[71] Z. Shen, Y. Qi, I. Z. Mitrovic, C. Zhao, S. Hall, L. Yang, T. Luo, Y. Huang, and C. Zhao, "Effect of Annealing Temperature for Ni/AlO_x/Pt RRAM Devices

Fabricated with Solution-Based Dielectric," *Micromachines (Basel),* vol. 10, no. 7, pp. 44601-44612, Jul 2 2019.

[72] C. Mahata, C. Lee, Y. An, M.-H. Kim, S. Bang, C. S. Kim, J.-H. Ryu, S. Kim, H. Kim, and B.-G. Park, "Resistive switching and synaptic behaviors of an HfO_2/Al_2O_3 stack on ITO for neuromorphic systems," *Journal of Alloys and Compounds,* vol. 826, pp. 154434-154460, 2020.

[73] X. Kang, J. Guo, Y. Gao, S. Ren, W. Chen, and X. Zhao, "NiO-based resistive memory devices with highly improved uniformity boosted by ionic liquid pre-treatment," *Applied Surface Science,* vol. 480, pp. 57-62, 2019.

[74] G. Wang, L. Hu, Y. Xia, Q. Li, and Q. Xu, "Resistive switching in $FeNi/Al_2O_3/NiO/Pt$ structure with various Al_2O_3 layer thicknesses," *Journal of Magnetism and Magnetic Materials,* vol. 493, pp. 165728-165734, 2020.

[75] J. Kim, S. Cho, T. Kim, and J. J. Pak, "Mimicking Synaptic Behaviors with Cross-Point Structured TiO_x/TiO_y-Based Filamentary RRAM for Neuromorphic Applications," *Journal of Electrical Engineering & Technology,* vol. 14, no. 2, pp. 869-875, 2019.

[76] C. H. Cheng, A. Chin, and H. H. Hsu, "Forming-Free $SiGeO_x/TiO_y$ Resistive Random Access Memories Featuring Large Current Distribution Windows," *J Nanosci Nanotechnol,* vol. 19, no. 12, pp. 7916-7919, Dec 1 2019.

[77] K.-J. Zhou, T.-C. Chang, C.-Y. Lin, C.-K. Chen, Y.-T. Tseng, H.-X. Zheng, H.-C. Chen, L.-C. Sun, C.-Y. Lien, Y.-F. Tan, C.-W. Wu, Y.-H. Yeh, and S. M. Sze, "Abnormal High Resistive State Current Mechanism Transformation in $Ti/HfO_2/TiN$ Resistive Random Access Memory," *IEEE Electron Device Letters,* vol. 41, no. 2, pp. 224-227, 2020.

[78] L. Cai, W. Chen, Y. Zhao, X. Liu, J. Kang, X. Zhang, and P. Huang, "Insight into Effects of Oxygen Reservoir Layer and Operation Schemes on Data Retention of HfO_2-Based RRAM," *IEEE Transactions on Electron Devices,* vol. 66, no. 9, pp. 3822-3827, 2019.

[79] S. Roy, G. Niu, Q. Wang, Y. Wang, Y. Zhang, H. Wu, S. Zhai, P. Shi, S. Song, Z. Song, Z. G. Ye, C. Wenger, T. Schroeder, Y. H. Xie, X. Meng, W. Luo, and W. Ren, "Toward a Reliable Synaptic Simulation Using Al-Doped HfO_2 RRAM," *ACS Appl Mater Interfaces,* vol. 12, no. 9, pp. 10648-10656, Mar 4 2020.

[80] D. Kumar, U. Chand, L. Wen Siang, and T.-Y. Tseng, "High-Performance $TiN/Al_2O_3/ZnO/Al_2O_3/TiN$ Flexible RRAM Device With High Bending Condition," *IEEE Transactions on Electron Devices,* vol. 67, no. 2, pp. 493-498, 2020.

[81] S. Ha, H. Lee, W.-Y. Lee, B. Jang, H.-J. Kwon, K. Kim, and J. Jang, "Effect of Annealing Environment on the Performance of Sol–Gel-Processed ZrO_2 RRAM," *Electronics,* vol. 8, no. 9, pp. 947-954, 2019.

[82] X. Wei, H. Huang, C. Ye, W. Wei, H. Zhou, Y. Chen, R. Zhang, L. Zhang, and Q. Xia, "Exploring the role of nitrogen incorporation in ZrO_2 resistive switching film for enhancing the device performance," *Journal of Alloys and Compounds,* vol. 775, pp. 1301-1306, 2019.

[83] K.-C. Liu, W.-H. Tzeng, K.-M. Chang, J.-J. Huang, Y.-J. Lee, P.-H. Yeh, P.-S. Chen, H.-Y. Lee, F. Chen, and M.-J. Tsai, "Investigation of the effect of different oxygen partial pressure to $LaAlO_3$ thin film properties and resistive switching characteristics," *Thin Solid Films,* vol. 520, no. 4, pp. 1246-1250, 2011.

[84] Y. Wang, H. Liu, X. Wang, and L. Zhao, "Impacts of Cu-Doping on the Performance of La-Based RRAM Devices," *Nanoscale Res Lett,* vol. 14, no. 1, pp. 22401-22409, Jul 9 2019.

[85] Y. A. Cheol Hwan Kim, and Jong Yeog Son, "$SrTiO_3$-Based Resistive Switching Memory Device with Graphene Nanoribbon Electrodes," *Rapid Communication,* vol. 99, no. 1, pp. 9-11, 2016.

[86] I. Kim, M. Siddik, J. Shin, K. P. Biju, S. Jung, and H. Hwang, "Low temperature solution-processed graphene oxide/$Pr_{0.7}Ca_{0.3}MnO_3$ based resistive-memory device," *Applied Physics Letters,* vol. 99, no. 4, pp. 042101-042104, 2011.

[87] S.-W. Chen and J.-M. Wu, "Unipolar resistive switching behavior of $BiFeO_3$ thin films prepared by chemical solution deposition," *Thin Solid Films,* vol. 519, no. 1, pp. 499-504, 2010.

[88] D. Liang, X. Li, J. Wang, L. Wu, and P. Chen, "Light-controlled resistive switching characteristics in ZnO/$BiFeO_3$/ZnO thin film," *Solid-State Electronics,* vol. 145, pp. 46-48, 2018.

[89] Q. Hu, T. S. Lee, N. J. Lee, T. S. Kang, M. R. Park, T.-S. Yoon, H. H. Lee, and C. J. Kang, "Resistive Switching Characteristics in MnO Nanoparticle Assembly and Ag_2Se Thin Film Devices," *Journal of Nanoscience and Nanotechnology,* vol. 17, no. 10, pp. 7189-7193, 2017.

[90] H. T. Hong-Yu Chen, Bin Gao, Shimeng Yu, Jiale Liang, Jinfeng Kang, Yuegang Zhang, Tian-Ling Ren, H.-S. Philip Wong, "Electrode oxide interface engineering by inserting single-layer graphene Application for HfO_x-based resistive random access memory," *IEEE Electron Device Letters,* vol. 11, pp. 489-492, 2012.

[91] L. Wu, J. Guo, W. Zhong, W. Zhang, X. Kang, W. Chen, and Y. Du, "Flexible, multilevel, and low-operating-voltage resistive memory based on MoS_2–rGO hybrid," *Applied Surface Science,* vol. 463, pp. 947-952, 2019.

[92] Z. Chen, Y. Zhang, Y. Yu, Y. Che, L. Jin, Y. Li, Q. Li, T. Li, H. Dai, and J. Yao, "Write once read many times resistance switching memory based on all-inorganic perovskite $CsPbBr_3$ quantum dot," *Optical Materials,* vol. 90, pp. 123-126, 2019.

[93] Q. A. Vu, H. Kim, V. L. Nguyen, U. Y. Won, S. Adhikari, K. Kim, Y. H. Lee, and W. J. Yu, "A High-On/Off-Ratio Floating-Gate Memristor Array on a Flexible Substrate via CVD-Grown Large-Area 2D Layer Stacking," *Adv Mater,* vol. 29, no. 44, pp. 1703363(1-7), Nov 2017.

[94] U. Das, S. Bhattacharjee, B. Mahato, M. Prajapat, P. Sarkar, and A. Roy, "Uniform, large-scale growth of WS_2 nanodomains via CVD technique for stable non-volatile RRAM application," *Materials Science in Semiconductor Processing,* vol. 107, pp. 104837(1-7), 2020.

[95] B. Ku, Y. Abbas, A. S. Sokolov, and C. Choi, "Interface engineering of ALD

HfO_2-based RRAM with Ar plasma treatment for reliable and uniform switching behaviors," *Journal of Alloys and Compounds,* vol. 735, pp. 1181-1188, 2018.

[96] Z. Yong, K.-M. Persson, M. Saketh Ram, G. D'Acunto, Y. Liu, S. Benter, J. Pan, Z. Li, M. Borg, A. Mikkelsen, L.-E. Wernersson, and R. Timm, "Tuning oxygen vacancies and resistive switching properties in ultra-thin HfO_2 RRAM via TiN bottom electrode and interface engineering," *Applied Surface Science,* vol. 551, pp. 149386(1-13), 2021.

[97] S. V. Kershaw, L. Jing, X. Huang, M. Gao, and A. L. Rogach, "Materials aspects of semiconductor nanocrystals for optoelectronic applications," *Materials Horizons,* vol. 4, no. 2, pp. 155-205, 2017.

[98] S.-T. Han, Y. Zhou, L. Zhou, Y. Yan, L.-B. Huang, W. Wu, and V. A. L. Roy, "CdSe/ZnS core–shell quantum dots charge trapping layer for flexible photonic memory," *Journal of Materials Chemistry C,* vol. 3, no. 13, pp. 3173(1-8), 2015.

[99] C.-C. Chiang, V. Ostwal, P. Wu, C.-S. Pang, F. Zhang, Z. Chen, and J. Appenzeller, "Memory applications from 2D materials," *Applied Physics Reviews,* vol. 8, no. 2, pp. 021306(1-19), 2021.

[100] X. Jiang, Q. Liu, J. Xing, N. Liu, Y. Guo, Z. Liu, and J. Zhao, "Recent progress on 2D magnets: Fundamental mechanism, structural design and modification," *Applied Physics Reviews,* vol. 8, no. 3, pp. 031305(1-69), 2021.

[101] J. Zhang, Y. Lu, S. Dai, R. Wang, D. Hao, S. Zhang, L. Xiong, and J. Huang, "Retina-Inspired Organic Heterojunction-Based Optoelectronic Synapses for Artificial Visual Systems," *Research (Wash D C),* vol. 2021, pp. 7131895(1-10), 2021.

[102] J. Zhang, Q. Shi, R. Wang, X. Zhang, L. Li, J. Zhang, L. Tian, L. Xiong, and J. Huang, "Spectrum-dependent photonic synapses based on 2D imine polymers for power-efficient neuromorphic computing," *InfoMat,* pp. 1-13, 2021.

[103] S. Zhang, K. Guo, H. Han, H. Yu, H. Wei, J. Gong, and W. Xu, "Multiplexed Neurotransmission Emulated by a p–n Cross Nanowire Synaptic Transistor for Satiety, Depression, and Drug Withdrawal," *Advanced Functional Materials,* pp. 2101917(1-9), 2021.

[104] H. Tian, J. Tice, R. Fei, V. Tran, X. Yan, L. Yang, and H. Wang, "Low-symmetry two-dimensional materials for electronic and photonic applications," *Nano Today,* vol. 11, no. 6, pp. 763(1-15), 2016.

[105] J. N. Tiwari, R. N. Tiwari, and K. S. Kim, "Zero-dimensional, one-dimensional, two-dimensional and three-dimensional nanostructured materials for advanced electrochemical energy devices," *Progress in Materials Science,* vol. 57, no. 4, pp. 724(1-80), 2012.

[106] R. Chen and L. Lan, "Solution-processed metal-oxide thin-film transistors: a review of recent developments," *Nanotechnology,* vol. 30, no. 31, pp. 312001(1-75), Aug 2 2019.

[107] J. W. Park, B. H. Kang, and H. J. Kim, "A Review of Low-Temperature Solution-Processed Metal Oxide Thin-Film Transistors for Flexible Electronics," *Advanced Functional Materials,* vol. 30, no. 20, pp. 1904632(1-

40), 2019.
[108] S. J. Kim, S. Yoon, and H. J. Kim, "Review of solution-processed oxide thin-film transistors," *Japanese Journal of Applied Physics,* vol. 53, no. 2S, pp. 02ba02(1-11), 2014.
[109] Y. Qi, C. Zhao, C. Z. Zhao, W. Xu, Z. Shen, J. He, T. Zhao, Y. Fang, Q. Liu, R. Yi, and L. Yang, "Enhanced resistive switching performance of aluminum oxide dielectric with a low temperature solution-processed method," *Solid-State Electronics,* vol. 158, pp. 28-36, 2019.
[110] Z. Shen, Y. Qi, I. Z. Mitrovic, C. Zhao, S. Hall, L. Yang, T. Luo, Y. Huang, and C. Zhao, "Effect of Annealing Temperature for Ni/AlO_X/Pt RRAM Devices Fabricated with Solution-Based Dielectric," *Micromachines (Basel),* vol. 10, no. 7, pp. 446(1-12), Jul 2 2019.
[111] Y. Qi, Z. Shen, C. Zhao, and C. Z. Zhao, "Effect of electrode area on resistive switching behavior in translucent solution-processed AlO_X based memory device," *Journal of Alloys and Compounds,* vol. 822, pp. 153603(1-10), 2020.
[112] Z. Shen, C. Zhao, Y. Liu, Y. Qi, I. Z. Mitrovic, L. Yang, and C. Zhao, "Performance variation of solution-processed memristor induced by different top electrode," *Solid-State Electronics,* vol. 186, pp. 108132(1-6), 2021.
[113] Y. F. Qi, Z. J. Shen, C. Zhao, I. Z. Mitrovic, W. Y. Xu, E. G. Lim, L. Yang, J. H. He, T. Luo, Y. B. Huang, and C. Z. Zhao, "Resistive switching behavior of solution-processed AlO_X and GO based RRAM at low temperature," *Solid-State Electronics,* vol. 168, pp. 107735(1-5), 2020.
[114] Z. Shen, C. Zhao, K. L. Man, Y. Liu, and C. Zhao, "Long-Term Memory Performance with Learning Behavior of Artificial Synaptic Memristor Based on Stacked Solution-Processed Switching Layers," presented at the 2021 IEEE International Symposium on Circuits and Systems (ISCAS), Daegu, Korea, 2021.

Chapter 2: Electrical performance for RRAM devices with solution-processed AlO_x dielectric

In this chapter, the electrical performance of RRAM devices with structures of Ni/SP-AlO_x/Pt and TiN/SP-AlO_x/Pt were researched in terms of bipolar I-V characteristics, voltage distribution, resistance distribution, endurance, and retention. For Ni/SP-AlO_x/Pt devices, the SP-AlO_x layers were annealed at 225°C, 250°C, and 275°C. The device with a 250°C annealed SP-AlO_x layer displayed the best performance with the lowest operation voltage, the longest retention time, and the most endurance cycles. A similar performance was also observed in TiN/SP-AlO_x/Pt RRAM devices and the TiN/SP-AlO_x/Pt device with a 250°C annealed SP-AlO_x layer also displayed the best electrical performance. While TiN/SP-AlO_x/Pt RRAM devices at various annealing temperatures showed higher operation voltages than Ni/SP-AlO_x/Pt samples with SP-AlO_x layers annealed at all temperatures. This performance variation was explained with the influence of $\Delta\Phi_M$ of TE and BE. In addition, the performance variation of devices with the same TE but the RS layer annealed at different temperatures were also discussed with the X-ray photoelectron spectroscopy (XPS) results, which was associated with the concentration variation of the hydroxyl group (-OH). [10, 110, 112]

2.1 Experimental

2.1.1 Preparation of AlO_x precursor solution

As mentioned above, all RS layers in this thesis were fabricated with the SP spin-

coating method. The SP-AlO_x layer was deposited from the precursor solution comprising of ~ 5 mL deionized (DI) water (solvent) and ~ 4.6765 g aluminum nitrate nonahydrate ($Al(NO_3)_3 \cdot 9H_2O$) powder (solute). With the magnetic stirring process, the 2.5 M precursor solution was stirred for about ~ 20 min until it was clear and transparent. The stirring temperature was the ambient temperature. The 2.5 M concentration of the AlO_x precursor solution was calculated from the equation 2-1 (**Eq. 2-1**) below,

$$M = \frac{m}{n \cdot v} \qquad \textbf{(Eq. 2-1)}$$

where M was the molar concentration of AlO_x precursor, m was the mass of $Al(NO_3)_3 \cdot 9H_2O$, n was the molecular weight of $Al(NO_3)_3 \cdot 9H_2O$, and v was the volume of DI water. Finally, the concentration of AlO_x precursor M was calculated as 2.5 M.

2.1.2 Fabrication of the Ni/SP-AlO_x/Pt RRAM device

The substrate layer Pt (Pt/Ti/SiO_2/Si) was ultrasonically cleaned in acetone, ethanol, and DI water, respectively. The ultrasonic cleaning process in each cleaning solvent was ~ 30 min to remove organic and inorganic impurities attached to the surface of the Pt layer. The cleaned Pt substrate was dried in a nitrogen environment until the remaining moisture was completely evaporated. To enhance the hydrophilia of the Pt layer, the dried Pt substrate was treated in a vacuum with a hydrophilic operation in a PLASMA cleaner (PDC-002 HARRICK PLASMA) for ~ 30 min. Herein, some induction and discission on the hydrophilic operation were presented. At first,

hydrophilic treatment is one of the common methods in the handling process of thin-film devices [115-121]. Hydrophilic treatment aims to change the hydrophilicity of materials [118-121]. Hydrophilicity means that molecules with polarizing groups have a strong affinity for water and can attract water molecules or dissolve in water [119]. It is a physical property that allows molecules to form short-term bonds with water through hydrogen bonds [116, 117]. Due to thermodynamics, this molecule is not only soluble in water but also soluble in other polar solutions [115-118]. A hydrophilic molecule, or the hydrophilic part of a molecule, can polarize, make it form hydrogen bonds, and make it more soluble in water in oil solutions or other hydrophobic solutions [115-117]. Hydrophilic and hydrophobic molecules can also be referred to as polar and non-polar molecules, respectively [115, 116, 120, 121]. Many hydrophilic groups, such as hydroxyl, carboxyl, amino, and sulfonic acid groups are easily combined with hydrogen bonds, so they are hydrophilic [115, 118, 119, 121]. In this work, the dielectric layers were fabricated from the precursor solution, which included a large number of hydroxyl groups. Therefore the hydrophilic treatment was conducted to enhance the hydrophilicity of the substrate, making the entire spin-coating process easier to achieve. A plasma cleaner (PDC-002 HARRICK PLASMA expanded plasma cleaner) was used to complete the hydrophilic treatment in a vacuum. The active particles in the plasma react with the surface of the material to produce hydrophilic groups, thereby enhancing hydrophilicity [116-120]. Secondly, the spin-coating process and the annealing process were conducted in the air, the environment temperature was the room temperature, which was ~ 25°C. Thirdly, the Pt/Ti/SiO_2/Si substrate was purchased from a professional organization

called Aladdin, and the Pt layer was deposited onto Ti/SiO_2/Si by the sputtering method. After the hydrophilic treatment, the prepared AlO_x precursor solution was spin-coated onto the Pt substrate through a medical syringe with a 0.45 μm polyethersulfone (PES) filter. The spin-coating speed was 4500 rpm and the spin-coating process last for ~ 40 s. After the spin-coating process, the semi-finished device was annealed at the desired temperature (225°C, 250°C, and 275°C) for ~ 60 min under an atmospheric condition. After the deposition process of the AlO_x layer, a TE layer of ~ 40-nm thick Ni (or TiN) and a capping layer of ~ 40-nm thick Al were deposited onto the AlO_x layer in the thermal evaporator. Electrodes Al, Ni, and TiN were all cylindrical and the diameter of each cylindrical electrode was 0.1 mm. The fabrication process could be observed in **Fig. 2-1**.

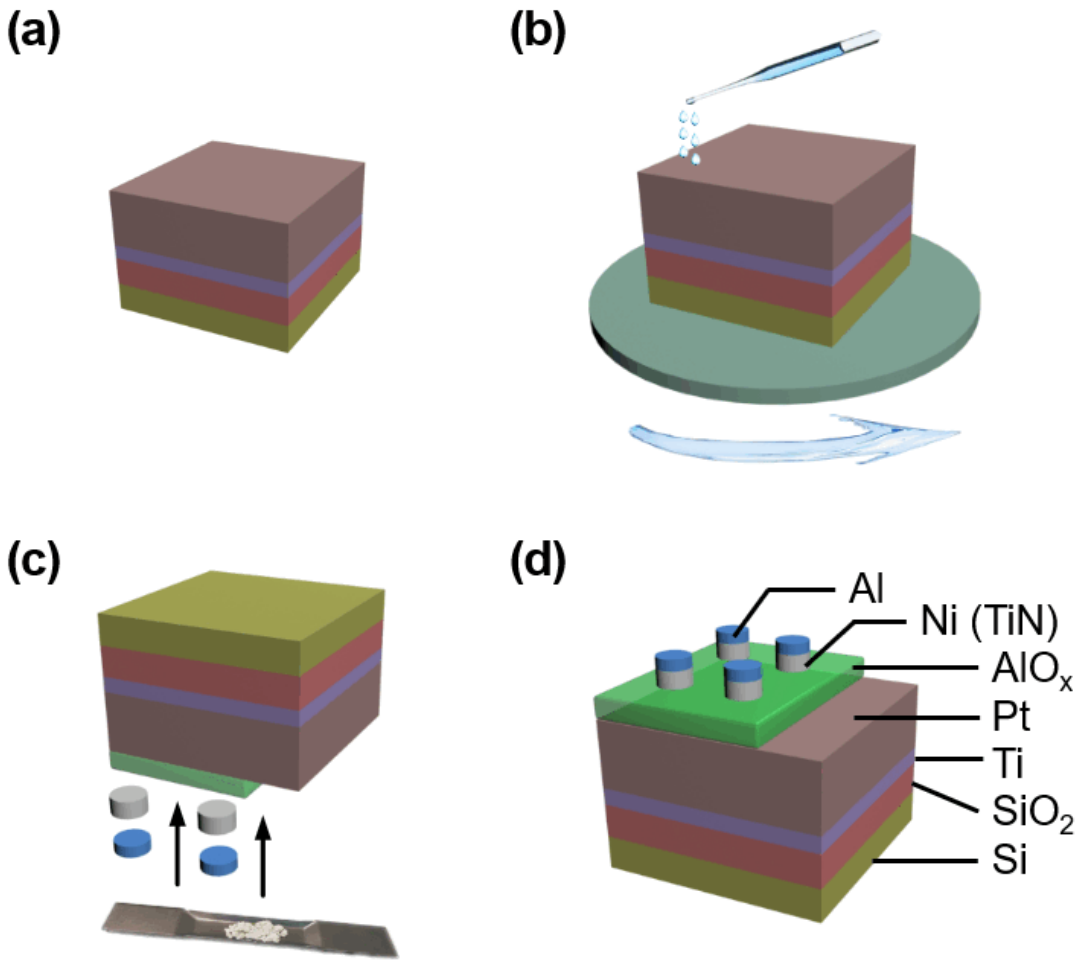

Figure 2-1. Fabrication process of an RRAM device with the SP-AlO_x layer, including (a) a cleaned and dried substrate, (b) the AlO_x precursor solution was spin-coated onto the substrate, (c) the TE layer and capping layers was thermal evaporated onto the deposited AlO_x layer, (d) the completed device with the structure of Al/Ni(TiN)/SP-AlO_x/Pt.

2.2 Results and discussion

2.2.1 I-V characteristics comparison between Ni/SP-AlO_x/Pt and TiN/SP-AlO_x/Pt RRAM devices

The scanning electron microscope (SEM) cross-sectional image in **Fig. 2-2a** indicated the successful deposition of a ~30-nm SP-AlO_x layer. The electrical performance of all devices was measured by an Agilent B1500A high-precision semiconductor analyzer (Agilent Santa Rosa, CA, USA). For the annealing process of the SP-AlO_x layer, a

lower temperature was desirable as it indicated the lower energy consumption in the fabrication process. During the measurement process, the RRAM device with an SP-AlO_x layer annealed at 200°C exhibited the breakdown characteristic at very low voltage < 0.3 V, whereas the 300°C annealed device rarely showed the breakdown behavior even the operation voltages higher than 18 V. The breakdown behavior and such high voltages were not desired for RRAM devices. Furthermore, almost no bipolar I-V characteristics could be observed at higher annealing temperatures (> 300°C). Therefore, 225°C, 250°C, and 275°C were selected as the desired annealing temperatures. As illustrated in **Fig. 2-2**, I-V curves of Ni/SP-AlO_x/Pt and TiN/SP-AlO_x/Pt RRAM devices with SP-AlO_x layers annealed at 225°C, 250°C, and 275°C demonstrated typical bipolar RS performance, which presented the resistance change with the SET and RESET processes. Take the I-V curves in **Fig. 2-2c** as an example. SET and RESET processes have been represented by circle numbers in black and green, respectively. During the SET process, with the positive voltage bias applied onto the TE layer, the resistance states change followed the black direction arrows from ① to ④ and the device was at ON state (LRS) when the operation current reached I_{CC} (1 mA). With the negative voltage bias applied onto the TE layer, the resistance states of the device change followed the green direction arrows from ⑤to ⑧ and the device switched back to the OFF state (HRS) at last. The purpose of only I_{CC}-setting in the SET process was to prevent the device from being destroyed by a large current. In order to make the device switch back to HRS to the greatest extent, there was no I_{CC}-setting during the RESET process. Compared with TiN/AlO_x/Pt RRAM devices, Ni/AlO_x/Pt

devices with solution-processed AlO_x layers annealed at different desired temperatures showed lower operation voltages in both SET and RESET processes. For Ni/AlO_x/Pt RRAM device, the voltage of Forming operation was very close to those of the following SET operations, which indicated the forming-free characteristic of the Ni/AlO_x/Pt RRAM device. Therefore, the power of the first SET for the Ni/AlO_x/Pt RRAM device could be considered as the initial power, which was lower than that of the TiN/AlO_x/Pt RRAM device. During the following SET operations, Ni/AlO_x/Pt RRAM device always showed lower power than that of the TiN/AlO_x/Pt RRAM device due to the lower operation voltage (they had the same compliance current of ~ 1mA). The same performance could be also observed during the RESET process.

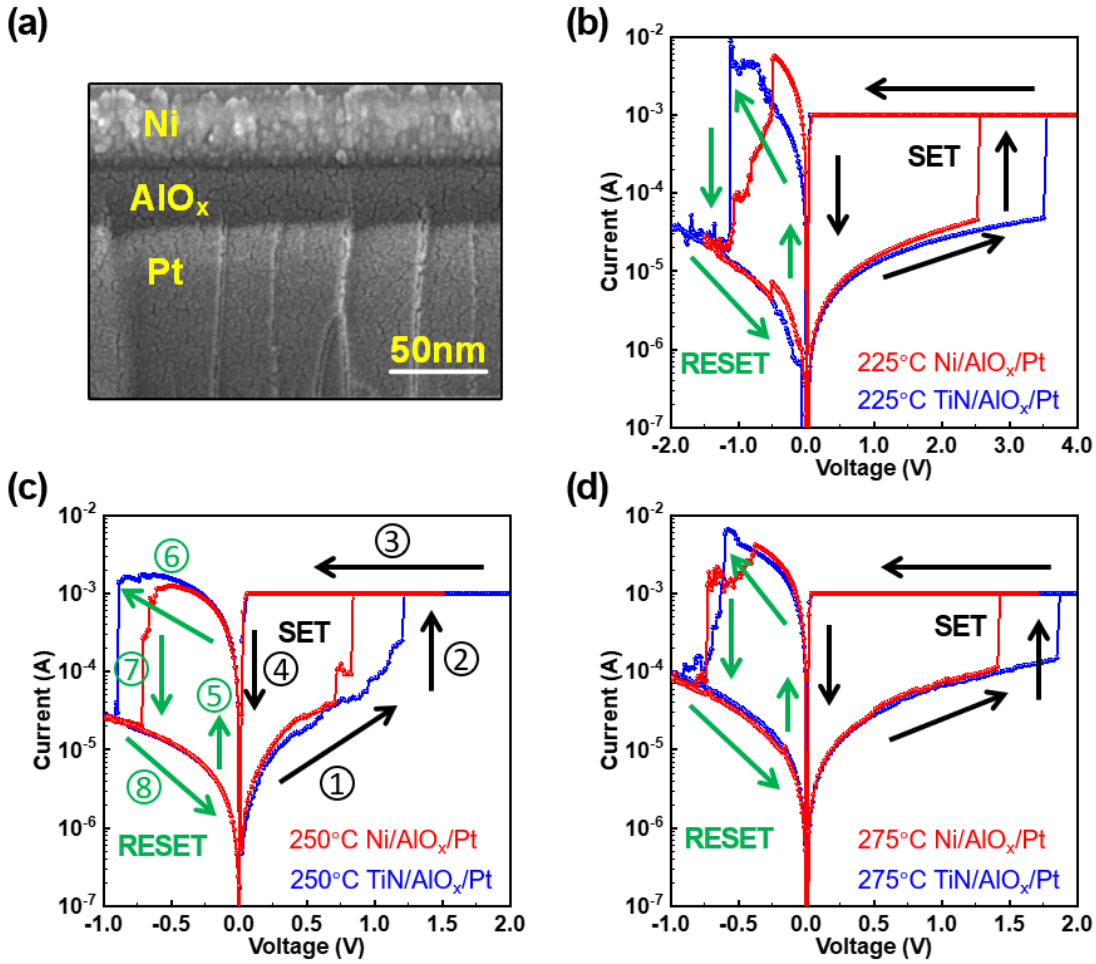

Figure 2-2. (a) Sectional view of SEM image of a Ni/SP-AlO_x/Pt RRAM device with a 250°C annealed SP-AlO_x layer. I-V characteristics with the typical bipolar RS performance of Ni/SP-AlO_x/Pt and TiN/SP-AlO_x/Pt RRAM devices annealed at (b) 225°C, (c) 250°C, and (d) 275°C.

Fig. 2-3 demonstrated the voltage distribution of Ni/SP-AlO_x/Pt and TiN/SP-AlO_x/Pt RRAM devices. **Fig. 2-3a** displayed the distribution of SET voltages and RESET voltages distribution could be observed in **Fig. 2-3b**. Fabricated 240 devices were prepared for the investigation in this chapter, including 225°C Ni/SP-AlO_x/Pt (40 devices), 225°C TiN/SP-AlO_x/Pt (40 devices), 250°C Ni/SP-AlO_x/Pt (40 devices), 250°C TiN/SP-AlO_x/Pt (40 devices), 275°C Ni/SP-AlO_x/Pt (40 devices) and 275°C TiN/SP-AlO_x/Pt (40 devices). For each box-line plot, operation voltages of 40 RRAM devices were gathered and distributed. For TiN/SP-AlO_x/Pt RRAM devices, the

samples with the SP-AlO_x layer annealed at 225°C operated with the highest operation voltages during the SET and RESET processes. Reversely, the operation voltages of 250°C annealed samples were the lowest during the switching process. The voltages of 275°C annealed samples were higher than that of 250°C annealed samples while lower than that of 225°C annealed samples. A similar distribution was also observed in Ni/SP-AlO_x/Pt RRAM devices. Ni/SP-AlO_x/Pt samples with 225°C annealed SP-AlO_x layers showed the highest voltages both in SET and RESET processes. Compared with 250° C Ni/SP-AlO_x/Pt samples, 275°C Ni/SP-AlO_x/Pt samples showed higher SET voltages. However, during the RESET process, similar RESET voltages were observed both in 250 ° C and 275 ° C Ni/SP-AlO_x/Pt samples, which might be resulted from the incompleted break of CF based on oxygen vacancies. [61, 62, 107, 108]

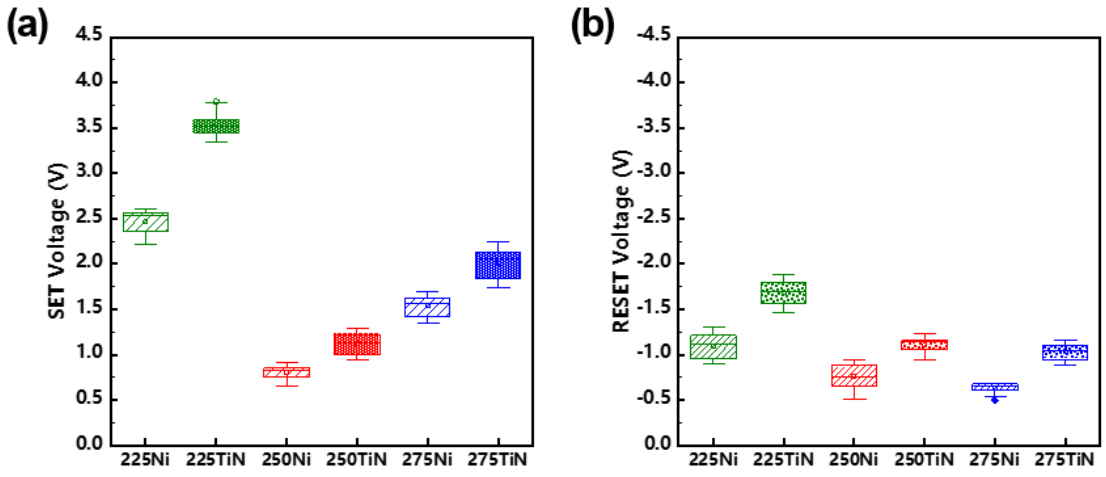

Figure 2-3. Voltage distribution of Ni/SP-AlO_x/Pt and TiN/SP-AlO_x/Pt RRAM devices annealed at 225°C, 250°C, and 275°C.

2.2.2 Endurance and retention of Ni/SP-AlO_x/Pt and TiN/SP-AlO_x/Pt RRAM devices

Fig. 2-4 displayed the endurance and retention performance of Ni/SP-AlO_x/Pt and

TiN/SP-AlO_x/Pt RRAM devices. **Figs. 2-4(a)**, **(c)**, and **(e)** presented the endurance cycles while the retention property was observed in **Figs. 2-4 (b)**, **(d)**, and **(f)**. The read voltage of the resistance values was 0.1 V for both endurance and retention performance. To ensure the accuracy of the performance analysis with the data dispersion, the standard deviation (σ) and the variation coefficient (c_v) were used as the major analysis index. The measurement of endurance and retention was conducted at room temperature (~25°C). Temperature retention is one of the reliability and stability metrics for RRAM devices and is considered at typical circuit operating temperatures up to 200°C. [122, 123] Compared with devices tested at room temperature, RRAM devices tested at high temperature (> 85°C) show deterioration of retention and endurance properties, including unstable ON/OFF ratio, unstable resistance values, shorter retention time, and reduced endurance cycles. In addition, a longer test time of retention (10 hours and 100 hours) is also associated with the degraded performance of RRAM devices. The RRAM devices in this chapter showed excellent resistive switching performance with the SP-AlO_x layers fabricated by the spin-coating method. As an emerging fabrication methodology, the solution-processed method is not as mature as traditional methods such as ALD and RF sputtering but is already for demonstrating the potential for application with high fabrication efficiency and low commercial cost. In particular, the inherent low-temperature process is compatible with the use of flexible substrates such as PET and PI, which are important for wearable devices. The temperature environment of wearable devices is always under 40°C, which is eco-friendly to the human body. In addition, with the tendency of low power consumption

in electronic devices, the operation temperature is decreasing dramatically. Therefore, high operating temperature issues may not be significant for solution-based RRAM devices.

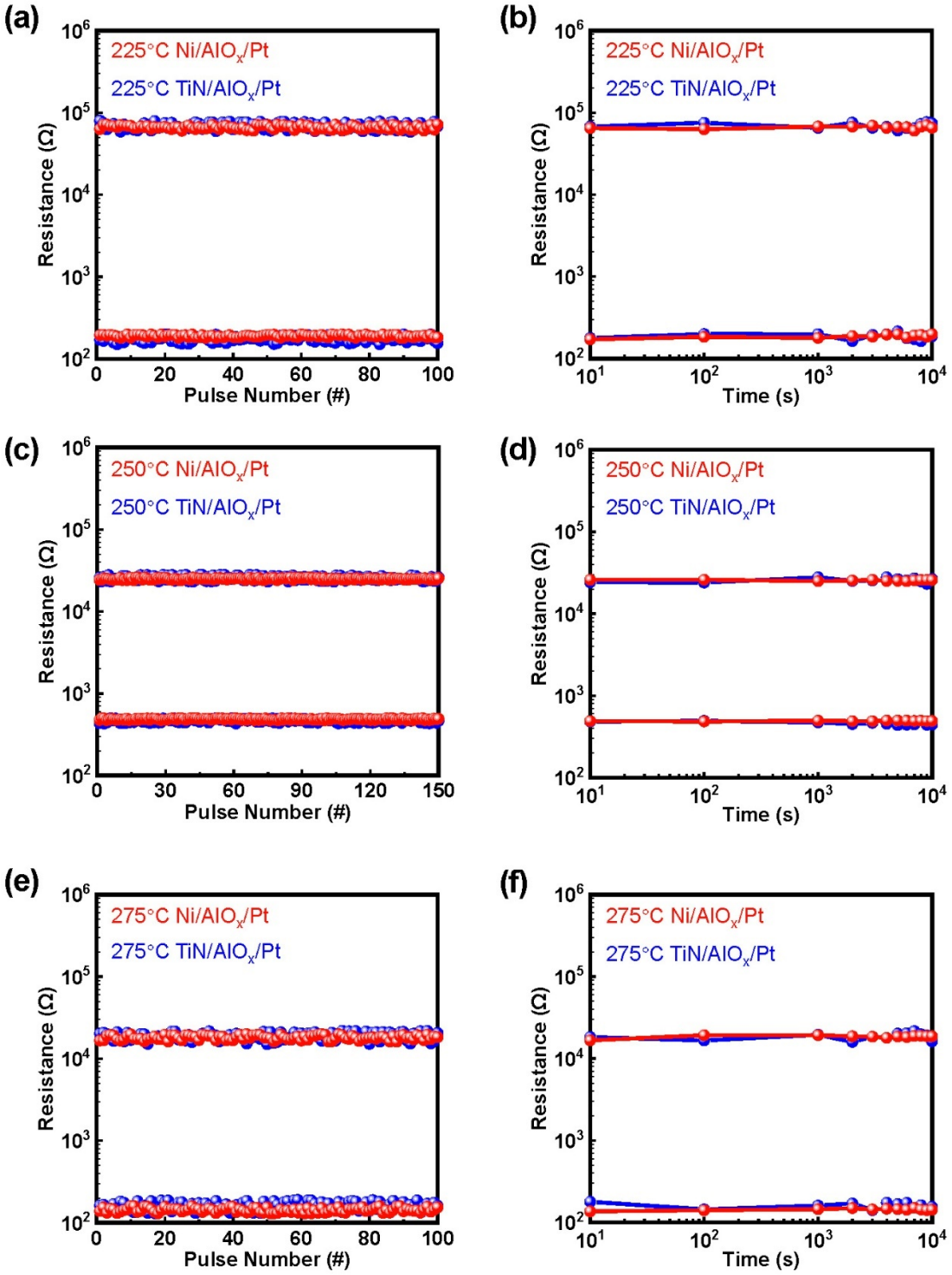

Figure 2-4. Endurance and retention properties of Ni/SP-AlO_x/Pt and TiN/SP-AlO_x/Pt RRAM devices annealed at 225°C, 250°C, and 275°C.

In general, several indexes are used to process the statistical dispersion, including range, sum of squares of deviation from mean, variance, standard deviation, and variation coefficient. Compared with other indexes, standard deviation and the variation coefficient can demonstrate the statistical dispersion with higher accuracy. [124-127] In addition, to a great extent, the data dispersion is influenced by the dimensions of data values, which should be under consideration. The standard deviation σ can be calculated with the equation 2-2 (**Eq. 2-2**), which was as follows:

$$\sigma = \sqrt{\frac{1}{n} \cdot \sum_{i=1}^{n} (x_i - \bar{x})^2} \qquad \textbf{(Eq. 2-2)}$$

where n is the total number of data, i is the sequence number of a data value and $i \leq n$, $\bar{x}$ is the average value of all data in the desired sequence. [124-127] σ is an index influenced by the value dimension. [61, 108, 124-127] For an RRAM device with the SP-AlO_x layer in this work, the data difference between HRS values and LRS values of one device was over two orders of magnitude (> 100 times), which indicated a large dimension variation and σ would not be appropriate to be used to evaluate the data dispersion between HRS and LRS values of the same device. However, the data difference among HRS values (or LRS values) of RRAM devices with various SP-AlO_x layers was smaller than one order of magnitude (< 10 times), therefore, it has been enough to evaluate the data dispersion among various RRAM devices through

comparing σ.

For the dispersion comparison between HRS values and LRS values of the same RRAM device, it should be considering the influence of data dimension. Therefore, the variation coefficient c_v could be used to evaluate the dispersion due to its dimensionless characteristic, which was as follows in equation 2-3 (**Eq. 2-3**):

$$c_v = \frac{\sqrt{\frac{1}{n} \cdot \sum_{i=1}^{n}(x_i - \bar{x})^2}}{\bar{x}} \quad \textbf{(Eq. 2-3)}$$

c_v could be described as the ratio between σ and the average value $\bar{x}$. [124-126] Based on **Eqs. 2-2** and **2-3**, **Tables 2-1** and **2-2** were presented with specific values of σ and c_v, which displayed standard deviation and variation coefficient for resistance values during the endurance of Ni/SP-AlO_x/Pt and TiN/SP-AlO_x/Pt with RS layers annealed at 225°C, 250°C, and 275°C. The smaller values of σ and c_v, the smaller the data dispersion. For external comparison among RRAM devices with SP-AlO_x layers annealed at different temperatures, Ni/SP-AlO_x/Pt samples presented smaller values of σ and c_v, which indicated that better electrical performance could be obtained on SP-AlO_x-based RRAM devices with Ni TE instead of TiN TE. In addition, compared with samples with 225°C and 275°C annealed SP-AlO_x layers, 250°C annealed Ni/SP-AlO_x/Pt samples exhibited better electrical with lower operation voltages and enhanced stability. The 250°C annealed Ni/SP-AlO_x/Pt samples showed the best stability with σ values of 4.99912 (LRS) and 589.14454 (LRS), and c_v values of 0.01853 (LRS) and

0.02354 (HRS). Similarly, although the device performance of TiN/SP-AlO_x/Pt samples was not as excellent as Ni/SP-AlO_x/Pt samples, 250°C annealed TiN/SP-AlO_x/Pt samples still showed better performance than 225°C and 275°C annealed TiN/SP-AlO_x/Pt samples.

Table 2-1. Standard deviation for resistance values during the endurance of Ni/SP-AlO_x/Pt and TiN/SP-AlO_x/Pt with RS layers annealed at desired temperatures (225°C, 250°C, and 275°C)

Samples	Resistance state	225°C	250°C	275°C
Ni/SP-AlO_x/Pt	LRS	5.90194	4.99912	8.49596
Ni/SP-AlO_x/Pt	HRS	3280.88764	589.14454	1103.54298
TiN/SP-AlO_x/Pt	LRS	13.57554	12.47578	18.05036
TiN/SP-AlO_x/Pt	HRS	6192.10980	1521.28229	1954.16433

Table 2-2. Variation coefficient for resistance values during the endurance of Ni/SP-AlO_x/Pt and TiN/SP-AlO_x/Pt with RS layers annealed at desired temperatures (225°C, 250°C, and 275°C)

Samples	Resistance state	225°C	250°C	275°C
Ni/SP-AlO_x/Pt	LRS	0.03105	0.01853	0.05926
Ni/SP-AlO_x/Pt	HRS	0.04952	0.02354	0.06100
TiN/SP-AlO_x/Pt	LRS	0.07805	0.04366	0.11140
TiN/SP-AlO_x/Pt	HRS	0.09004	0.05949	0.10392

2.2.3 Mechanism analysis on performance variation of Ni/SP-AlO_x/Pt and TiN/SP-AlO_x/Pt RRAM devices with SP-AlO_x layers annealed at the same desired temperature

Based on the obvious performance variation among Ni/SP-AlO_x/Pt and TiN/SP-AlO_x/Pt RRAM devices with SP-AlO_x layers, it was necessary to analyze the variation in terms of the switching and conduction mechanisms. In general, the mechanism analysis was divided into two parts, and the first part was about the operation voltage

comparison between Ni/SP-AlO_x/Pt and TiN/SP-AlO_x/Pt RRAM devices with the SP-AlO_x layers annealed at the same desired temperature, which was discussed in this section. The performance variation induced by different TE materials (Ni and TiN) indicated the role of work function difference ($\Delta\Phi_M$) between TE and BE.

Figs. 2-5a and **2-5b** displayed the energy band change of a TiN/SP-AlO_x/Pt device while the energy band change of a Ni/SP-AlO_x/Pt device could be observed in **Figs. 2-5c** and **2-5d**. Ni/SP-AlO_x/Pt and TiN/SP-AlO_x/Pt devices shared the same work function of Pt substrate ($\Phi_{M\text{-}Pt}$), which was ~ 5.93 eV. [128-130] Therefore, the voltage variation was mainly determined by the different Φ_M of TE Ni and TiN, which were ~ 5.35 eV ($\Phi_{M\text{-}Ni}$), and ~ 4.4 eV ($\Phi_{M\text{-}TiN}$). [129, 131-133] In **Figs. 2-5a** and **2-5c**, oxygen trap left in SP-AlO_x layers of the devices at the initial OFF state. With the external electric field induced by desired voltage bias in **Figs. 2-5a** and **2-5c**, the drift process of electrons occurred with the drift direction from BE to TE. The Φ_M was defined as the minimum energy consumption of the escape process of electrons and the escape direction was from the inside of the metal to the vacuum. Therefore, a larger Φ_M indicated that it was harder for electrons to escape. $\Delta\Phi_M$ still influenced the whole drift process of electrons and the higher $\Delta\Phi_M$ indicated that it was required more energy to support the electron drift, which presented the RS behavior with higher voltage. [129, 133-137] $\Delta\Phi_M$ between Ni and Pt was smaller than that between TiN and Pt (0.58 eV < 1.53 eV). Therefore, a lower V_{SET} of Ni/SP-AlO_x/Pt device was needed during the SET process. During the RESET process, lower energy demand was required to cancel the

band bending of the SP-AlO_x layer, which indicated the lower operation voltages were needed during the RS process. [129, 133-137]

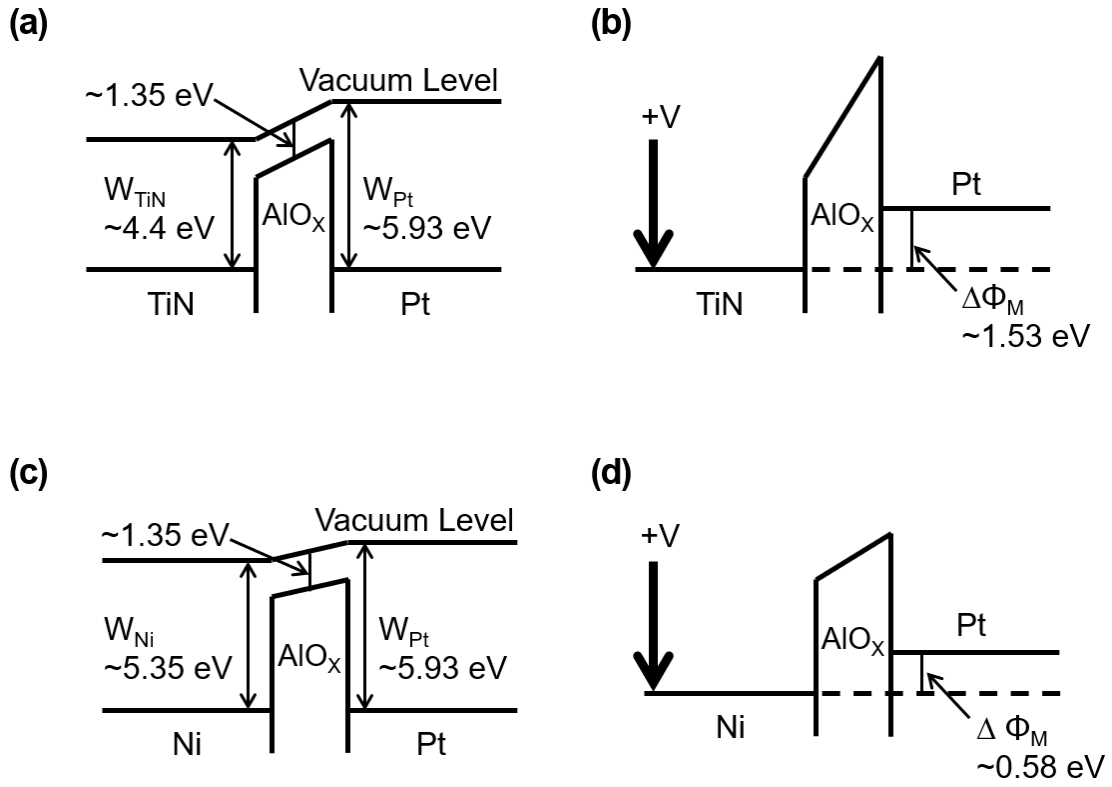

Figure 2-5. Energy band diagrams of Ni/SP-AlO_x/Pt devices at (a) initial state without external voltage bias, (b) ON state after the SET operation, and energy band diagrams of TiN/SP-AlO_x/Pt devices at (a) initial state without external voltage bias, and (b) ON state after the SET operation.

2.2.4 Mechanism analysis on performance variation of Ni/SP-AlO_x/Pt with SP-AlO_x layers annealed at different temperatures

As mentioned before, there were two parts of mechanism analysis were investigated and the first one has been introduced in the last section. The second one was introduced in this section. The second part mainly focused on the device variation of Ni/SP-AlO_x/Pt RRAM devices with SP-AlO_x layers annealed at 225°C, 250°C, and 275°C, which also revealed the influence induced by the change of hydroxyl group (-OH) concentration with various annealing temperatures. [129, 133-137]

Based on previous research, obviously, Ni/SP-AlO_x/Pt RRAM devices exhibited more excellent RS behaviors with lower operation voltages, stable ON/OFF ratio, and better stability. It was significant to investigate the performance variation of Ni/SP-AlO_x/Pt samples with SP-AlO_x layers annealed at different temperatures. Before starting the mechanism analysis, some physical characterizations were carried out to evaluate the properties of SP-AlO_x thin films at first, as illustrated in **Fig. 2-6**. **Fig. 2-6a** showed the x-ray diffraction (XRD) results of SP-AlO_x thin films annealed at 225°C, 250°C, and 275°C. All thin films demonstrated similar amorphous characteristics, which indicated the successful film-forming process of the SP-AlO_x layer with low annealing temperature. With the measurement of atomic force microscope (AFM), **Figs. 2-6b**, **2-6c**, and **2-6d** demonstrated the different roughness of SP-AlO_x thin films annealed at 225°C, 250°C, and 275°C, respectively. The roughness of the 225°C annealed SP-AlO_x thin film was 0.682 nm, which was the highest among all samples. The roughness of 250°C and 275°C annealed SP-AlO_x thin films were 0.230 nm and 0.524 nm, respectively. The smaller the roughness value, the smoother the dielectric thin film. [129, 133-137] Theoretically, a smoother surface of the dielectric layer is essential to achieve a lower leakage current, which is helpful to improve the electrical performance of the device. [129, 133-137] Therefore, the smoothest SP-AlO_x thin film was obtained with the 250°C annealing temperature and the 250°C annealed Ni/SP-AlO_x/Pt RRAM device demonstrated the best electrical performance.

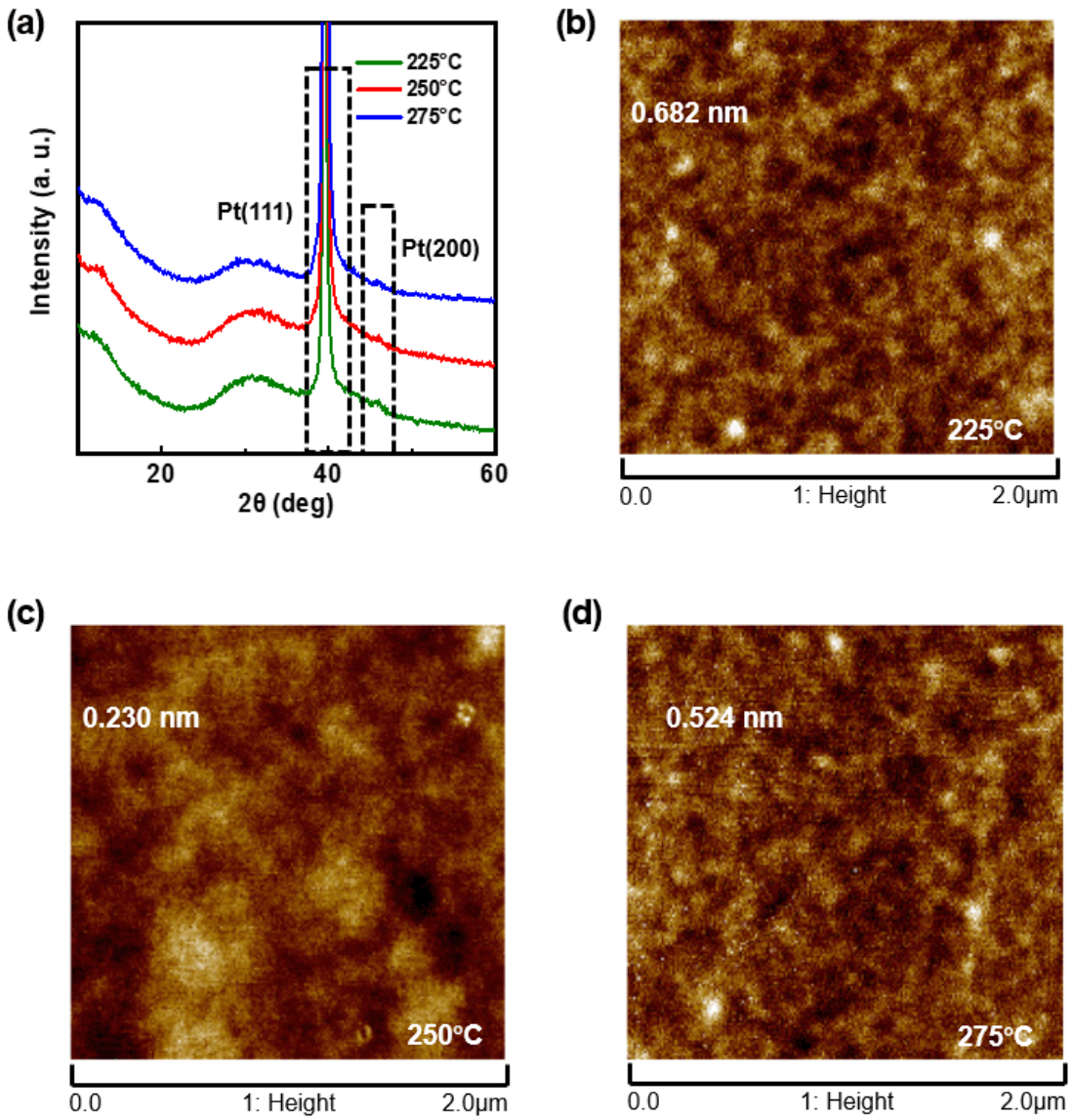

Figure 2-6. (a) XRD results of SP-AlO_x thin films annealed at different temperatures. AFM-roughness results of SP-AlO_x thin films annealed at (b) 225°C, (c) 250°C, and (d) 275°C.

Characterization results in **Fig. 2-6** have indicated that the excellent performance of 250°C annealed Ni/SP-AlO_x/Pt samples was determined by related characteristics of the SP-AlO_x thin film annealed at 250°C. In the later content of this section, the discussion of switching and conduction mechanism for Ni/SP-AlO_x/Pt RRAM devices would be presented, and then XPS spectra would be utilized to investigate the performance variation of Ni/SP-AlO_x/Pt RRAM devices with SP-AlO_x layers annealed

at 225°C, 250°C, and 275°C.

Fig. 2-7 demonstrated the schematic views of conduction and switching mechanisms. The conduction mechanism could be observed in **Figs. 2-7a**, **2-7b**, and **2-7c**, which corresponded to Ni/SP-AlO_x/Pt samples with SP-AlO_x layers annealed at 225°C, 250° C, and 275 ° C, respectively. **Figs. 2-7d**, **2-7e**, and **2-7f** described the switching mechanism based on the formation and rupture behaviors of CF comprising oxygen vacancies. Fitting results of the conduction mechanism pointed that the space-charge-limited current (SCLC) was the dominating mechanism of all samples. Herein, the 225° C annealed Ni/SP-AlO_x/Pt sample was chosen as the typical example for a further and detailed discussion on conduction and switching mechanisms.

As illustrated in **Fig. 2-7a**, I-V curves with the form of a double logarithmic plot presented positive and negative bias regions, which corresponded to original SET and RESET processes. The value of I_{CC} was very close to the value of RESET current, which resulted in the overlap with a large area between SET and RESET curves. The OFF state of I-V curves in **Fig. 2-7a** was corresponding to the OFF state exhibited in **Fig. 2-7d**, where the Ni/SP-AlO_x/Pt RRAM device was at the initial HRS state without any external voltage bias. Oxygen atoms (blue balls) stayed in the SP-AlO_x RS layer. When the external positive voltage bias (+ V) was applied onto TE Ni in **Fig. 2-7e**, the switching current started to change with the increase of the switching voltage. The slope of ~ 1 in **Fig. 2-7a** indicated the ohmic conduction ($I \propto V$) of the switching current

with low switching voltage during this phase. [41, 138, 139] When the + V in **Fig. 2-7e** increased to V_{SET}, the RRAM device was at the ON state (LRS). Electrons brought by the external electric field moved from BE to TE. Oxygen atoms combined with electrons (oxygen ions) also drift to TE while oxygen vacancies (red balls) were left in the SP-AlO_x RS layer. CFs were formed with left oxygen vacancies to connect TE and BE, which resulted in the LRS of the RRAM device. During the process where the device switched from the initial OFF state to the ON state, the slope of I-V curves in **Fig. 2-7a** changed from ~ 2.1 to ~ 4.9, which followed Child's square law ($I \propto V^2$) and the steep increase of the current ($I \propto V^x$, $x > 2$), which indicated the SCLC mechanism. [41, 140-144] When the negative voltage was (- V) applied onto TE Ni, as illustrated in **Fig. 2-7e**, the voltage amplitude still changed from 0 V to V_{RESET} and then back to 0 V. During the increasing phase from 0 V to V_{RESET}, the RRAM device was still at the ON state. When the voltage amplitude reached V_{RESET}, the negative electric field drove oxygen ions in TE to move to the SP-AlO_x RS layer. The density of oxygen vacancies was reduced and then resulted in the rupture of CFs, which made the RRAM device switched back to the OFF state. [108, 110, 112] The same explanation could be applied to Ni/SP-AlO_x/Pt RRAM devices with SP-AlO_x thin films annealed at 250°C and 275°C.

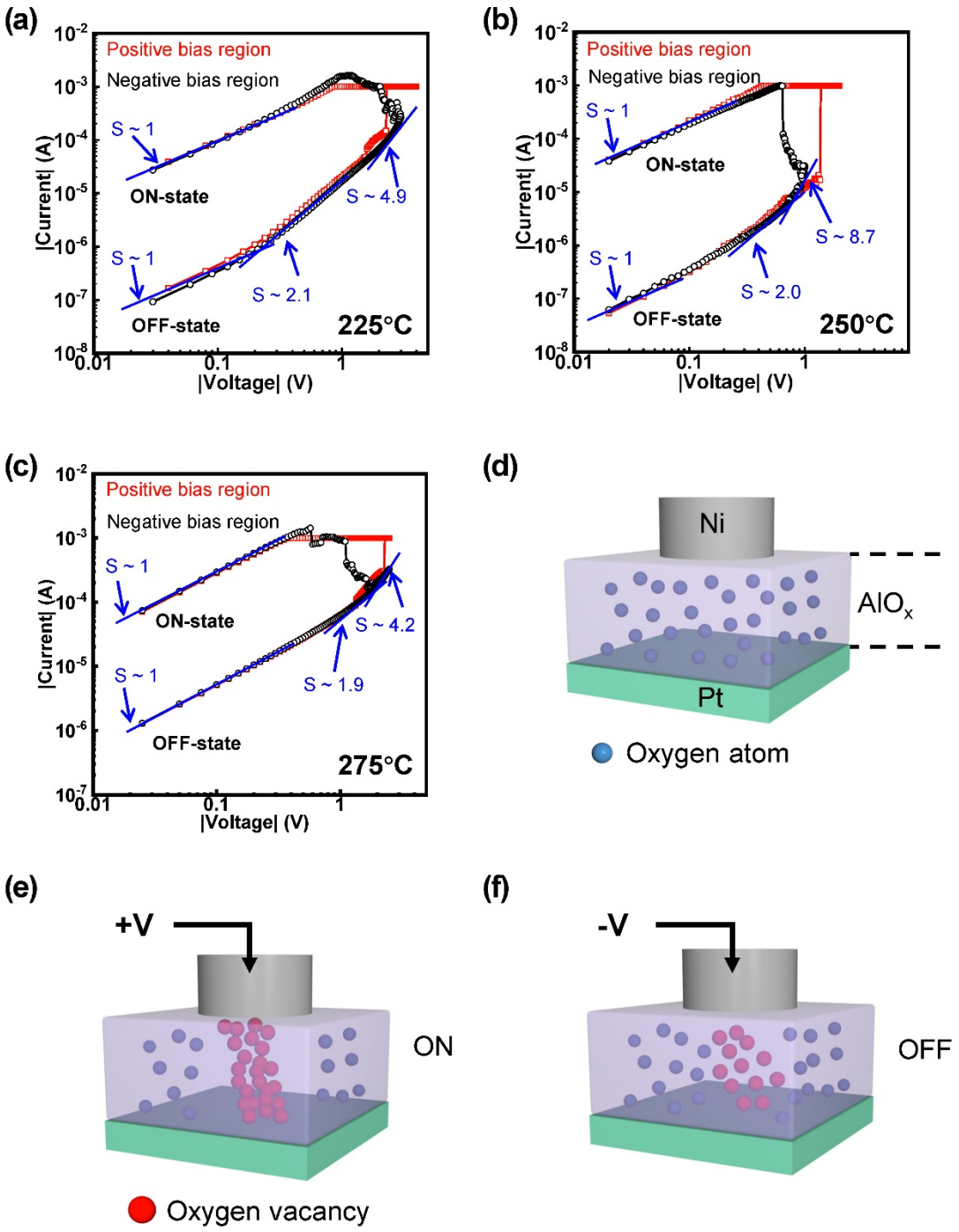

Figure 2-7. Conduction mechanisms of Ni/SP-AlO_x/Pt RRAM devices with SP-AlO_x layers annealed at (a) 225°C, (b) 250°C, and (c) 275°C. Switching mechanism with a Ni/SP-AlO_x/Pt RRAM device at (d) initial OFF state, (e) ON state after a SET operation, and (f) OFF state after a RESET operation.

During the formation/rupture process of CFs, it was necessary to consider the influence of vital properties of RS thin film, including thickness, uniformity, growth temperature,

etc. As characterized by AFM in **Fig. 2-6**, the roughness and uniformity of an SP thin film were determined by the annealing temperature. Therefore, further investigation on the internal change of SP-AlO_x thin films was carried out with XPS. For the XPS measurement process, some related parameters of the measurement environment were presented. The Total Acquisition Time was 1 min and 20.4 s, the Number of Scans was 8, the Source Gun Type was Al K Alpha, the Spot Size was 500 μm, the Lens Mode was Standard, the Analyzer Mode was CAE: Pass Energy 30.0 eV, the Energy Step Size was 0.100 eV, and the Number of Energy Steps was 210. The XPS measurement was taken from the surface of the SP-AlO_x thin film. The thickness of the SP-AlO_x thin film was about 30 nm, which was larger than the profiling depth of XPS. Device samples for XPS measurement were fabricated with the same methodology, without a top electrode. All samples were stored in a vacuum oven before the XPS measurement. During the XPS measurement process, all samples were operated in a vacuum. **Figs. 2-8a**, **2-8c**, and **2-8e** demonstrated the O 1s spectra of SP-AlO_x thin films annealed at 225° C, 250°C, and 275°C, respectively. While the corresponding spectra of Al 2p could be observed in **Figs. 2-8b**, **2-8d**, and **2-8f**. For one sample, O_1 and O_2 were two de-convoluted sub-peaks of the O 1s spectrum. The binding energies of O_1 and O_2 peaks were located at 531.1 eV and 532.2 eV, which were related to metal-oxygen bonds (M-O) and hydroxyl group (-OH), respectively. [144-148] With the annealing temperature increased from 225°C to 250°C, an obvious increasing tendency of the peak O_2 associated with -OH was observed. However, the concentration of O_2 decreased with the annealing temperature increased from 250°C to 275°C. The change of Al 2p also

supported the change tendency of O 1s. For now, it has been confirmed that M-O and -OH were playing significant roles during the RS process. With further comparison in **Fig. SI-1** with error bars in the supplementary information, the concentration of M-O and -OH for each sample were obtained. For each annealing temperature, 20 samples were evaluated with the XPS measurement and all data in **Fig. SI-1** were from 60 samples. For the 225°C annealed SP-AlO_x thin film, the concentration of M-O was about 50%, which was approximately equal to the concentration of -OH. For the 250° C annealed SP-AlO_x thin film, the concentration of -OH was about ~ 70%, which was higher than the concentration of M-O. The -OH concentration of the 275°C annealed SP-AlO_x thin film was still higher than that of M-O, which was around 61% and slightly lower than the -OH concentration of the 250°C annealed sample. Therefore, the 225°C annealed sample displayed the lowest concentration of -OH while the highest -OH concentration was detected in the 250°C annealed sample. The -OH concentration of 275°C annealed sample was lower than that of 250°C annealed sample but higher than that of 225°C annealed sample. These results were corresponding to the roughness variation of SP-AlO_x thin films with AFM measurement.

Therefore, based on the electrical performance variation, the roughness variation, and the composition change tendency, an overall hypothesis was proposed. During the deposition process of the RS layer, the annealing temperature of the SP-AlO_x thin film determined the dominant composition of AlO_x, which included AlO_x and $Al(OH)_x$. AlO_x and $Al(OH)_x$ were associated with concentration variation of M-O and -OH. For

SP-AlO_x thin films annealed at 225°C, 250°C, and 275°C, 250°C annealed thin film exhibited the lowest roughness due to the highest -OH concentration, which was helpful to the sufficient accumulation of oxygen vacancies. Therefore, the Ni/SP-AlO_x/Pt RRAM device with a 250°C annealed SP-AlO_x layer demonstrated the best electrical performance with the lowest operation voltage, stablest ON/OFF ratio, and the best stability. Due to the lowest -OH concentration of the 225°C annealed SP-AlO_x thin film, the worst electrical performance of the Ni/SP-AlO_x/Pt RRAM device with a 225°C annealed SP-AlO_x layer was observed. For the 275°C annealed SP-AlO_x thin film, its concentration of -OH was between that of 250°C and 225°C annealed thin films, hence the electrical performance of the 275°C annealed Ni/SP-AlO_x/Pt RRAM device was also between that of 250°C and 225°C annealed Ni/SP-AlO_x/Pt RRAM devices.

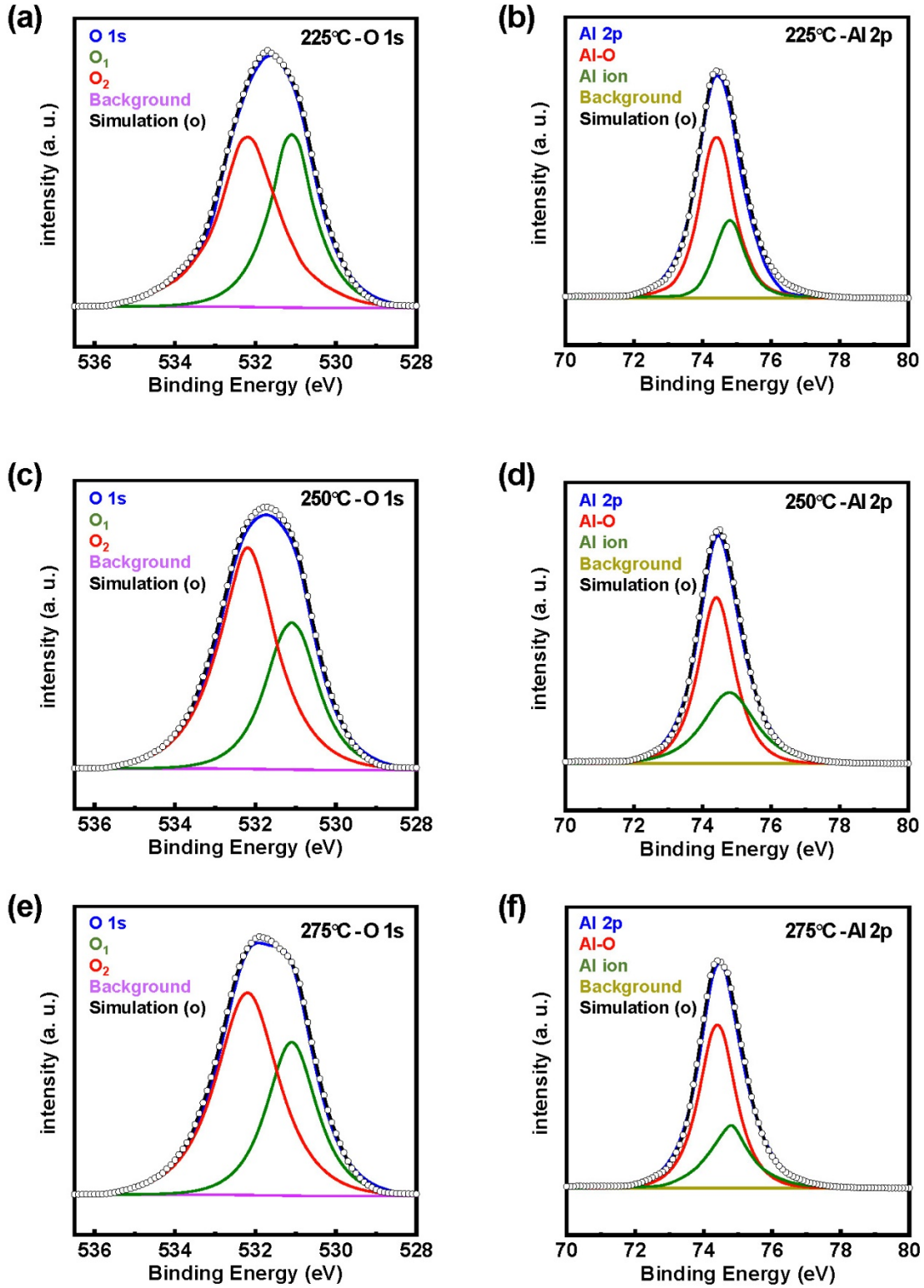

Figure 2-8. Fitted XPS spectra for O 1s for Ni/SP-AlO_x/Pt RRAM devices annealed at (a) 225°C, (c) 250°C, and (e) 275°C. Fitted XPS spectra for Al 2p for Ni/SP-AlO_x/Pt RRAM devices annealed at (b) 225°C, (d) 250°C, and (f) 275°C.

2.3 Conclusion

In this chapter, the electrical performance of Ni/SP-AlO_x/Pt and TiN/SP-AlO_x/Pt RRAM devices were studied with SP-AlO_x layers annealed at 225°C, 250°C, and 275° C. Compared with TiN/SP-AlO_x/Pt RRAM devices, Ni/SP-AlO_x/Pt devices under each annealing temperature exhibited better performance with lower operation voltages, more stable ON/OFF ratio, and enhanced stability, which was contributed to the smaller $\Delta\Phi_M$ between TE Ni and BE Pt. For Ni/SP-AlO_x/Pt RRAM devices with SP-AlO_x layers annealed at different temperatures, the 250°C annealed device displayed the best electrical performance in terms of the lowest operation voltage (< 1.5 V), the stablest ON/OFF ratio (> 10^2), and the best stability (retention time > 10^4 s and endurance cycles > 150), which was resulted from the highest -OH concentration of the 250°C annealed SP-AlO_x thin film.

2.4 References

[10] Z. Shen, C. Zhao, Y. Qi, W. Xu, Y. Liu, I. Z. Mitrovic, L. Yang, and C. Zhao, "Advances of RRAM Devices: Resistive Switching Mechanisms, Materials and Bionic Synaptic Application," *Nanomaterials (Basel),* vol. 10, no. 8, pp. 1437(1-31), Jul 23 2020.

[41] T. Guo, B. Sun, Y. Zhou, H. Zhao, M. Lei, and Y. Zhao, "Overwhelming coexistence of negative differential resistance effect and RRAM," *Phys Chem Chem Phys,* vol. 20, no. 31, pp. 20635-20640, Aug 8 2018.

[61] H. S. P. Wong, H.-Y. Lee, S. Yu, Y.-S. Chen, Y. Wu, P.-S. Chen, B. Lee, F. T. Chen, and M.-J. Tsai, "Metal–Oxide RRAM," *Proceedings of the IEEE,* vol. 100, no. 6, pp. 1951-1970, 2012.

[62] X. Hong, D. J. Loy, P. A. Dananjaya, F. Tan, C. Ng, and W. Lew, "Oxide-based RRAM materials for neuromorphic computing," *Journal of Materials Science,* vol. 53, no. 12, pp. 8720-8746, 2018.

[107] J. W. Park, B. H. Kang, and H. J. Kim, "A Review of Low-Temperature

Solution-Processed Metal Oxide Thin-Film Transistors for Flexible Electronics," *Advanced Functional Materials,* vol. 30, no. 20, pp. 1904632(1-40), 2019.

[108] S. J. Kim, S. Yoon, and H. J. Kim, "Review of solution-processed oxide thin-film transistors," *Japanese Journal of Applied Physics,* vol. 53, no. 2S, pp. 02ba02(1-11), 2014.

[110] Z. Shen, Y. Qi, I. Z. Mitrovic, C. Zhao, S. Hall, L. Yang, T. Luo, Y. Huang, and C. Zhao, "Effect of Annealing Temperature for Ni/AlO_X/Pt RRAM Devices Fabricated with Solution-Based Dielectric," *Micromachines (Basel),* vol. 10, no. 7, pp. 446(1-12), Jul 2 2019.

[112] Z. Shen, C. Zhao, Y. Liu, Y. Qi, I. Z. Mitrovic, L. Yang, and C. Zhao, "Performance variation of solution-processed memristor induced by different top electrode," *Solid-State Electronics,* vol. 186, pp. 108132(1-6), 2021.

[115] V. M. Gun'ko, V. V. Turov, V. M. Bogatyrev, V. I. Zarko, R. Leboda, E. V. Goncharuk, A. A. Novza, A. V. Turov, and A. A. Chuiko, "Unusual properties of water at hydrophilic/hydrophobic interfaces," *Adv Colloid Interface Sci,* vol. 118, no. 1-3, pp. 125-72, Dec 30 2005.

[116] T. Oroguchi and M. Nakasako, "Influences of lone-pair electrons on directionality of hydrogen bonds formed by hydrophilic amino acid side chains in molecular dynamics simulation," *Sci Rep,* vol. 7, no. 1, pp. 15859-15872, Nov 20 2017.

[117] K. H. T. Suni, I. Suni, and J. Ma¨kinen, "Effects of Plasma Activation on Hydrophilic Bonding of Si and SiO_2," *Journal of The Electrochemical Society,* vol. 149, no. 6, pp. G348-G351, 2002.

[118] J. S. Heo, J. W. Jo, J. Kang, C. Y. Jeong, H. Y. Jeong, S. K. Kim, K. Kim, H. I. Kwon, J. Kim, Y. H. Kim, M. G. Kim, and S. K. Park, "Water-Mediated Photochemical Treatments for Low-Temperature Passivation of Metal-Oxide Thin-Film Transistors," *ACS Appl Mater Interfaces,* vol. 8, no. 16, pp. 10403-10412, Apr 27 2016.

[119] W. Wu, L. Liang, J. Yu, X. Xiao, H. Zhang, J. Gao, F. Zhuge, T.-C. Chang, L. Lan, and H. Cao, "Aqueous solution-processed, self-flattening AlO_x:Y dielectrics for fully-transparent thin-film transistors," *Ceramics International,* vol. 45, no. 13, pp. 15883-15891, 2019.

[120] E. Carlos, S. Dellis, N. Kalfagiannis, L. Koutsokeras, D. C. Koutsogeorgis, R. Branquinho, R. Martins, and E. Fortunato, "Laser induced ultrafast combustion synthesis of solution-based AlO_x for thin film transistors," *Journal of Materials Chemistry C,* vol. 8, no. 18, pp. 6176-6184, 2020.

[121] M. M. Hasan, M. M. Islam, X. Li, M. He, R. Manley, J. Chang, N. Zhelev, K. Mehrotra, and J. Jang, "Interface Engineering With Polystyrene for High-Performance, Low-Voltage Driven Organic Thin Film Transistor," *IEEE Transactions on Electron Devices,* vol. 67, no. 4, pp. 1751-1756, 2020.

[122] Y. Y. Chen, L. Goux, S. Clima, B. Govoreanu, R. Degraeve, G. S. Kar, A. Fantini, G. Groeseneken, D. J. Wouters, and M. Jurczak, "Endurance/Retention Trade-off on HfO_2/Metal Cap 1T1R Bipolar RRAM," *IEEE Transactions on Electron*

Devices, vol. 60, no. 3, pp. 1114-1121, 2013.
[123] M.-S. Kang and W.-J. Cho, "Effect of microwave irradiation power on resistive switching performance in solution-processed aluminum oxide resistive memory," *Journal of Physics and Chemistry of Solids,* vol. 123, pp. 52-58, 2018.
[124] M. E. Edjabou, J. A. Martin-Fernandez, C. Scheutz, and T. F. Astrup, "Statistical analysis of solid waste composition data: Arithmetic mean, standard deviation and correlation coefficients," *Waste Manag,* vol. 69, pp. 13-23, Nov 2017.
[125] C. Zambelli, A. Grossi, P. Olivo, C. Walczyk, and C. Wenger, "RRAM Reliability/Performance Characterization through Array Architectures Investigations," presented at the 2015 IEEE Computer Society Annual Symposium on VLSI, Montpellier, France, 2015.
[126] R. Ram, "International convergence in population happiness: evidence from recent data," *Applied Economics,* vol. 53, no. 34, pp. 3984-3991, 2021.
[127] R. B. Maurizio Trevisan, Malathi Ram, Paola Muti, Jo Freudenheim, Ann Marie Carosella, and Donald Armstrong, "Correlates of Markers of Oxidative Status in the General Population," *American Journal of Epidemiology,* vol. 154, no. 4, pp. 348-356, 2001.
[128] B. Ghosh and M. W. Akram, "Junctionless Tunnel Field Effect Transistor," *IEEE Electron Device Letters,* vol. 34, no. 5, pp. 584-586, 2013.
[129] C. Beasley, M. Kumaran Gnanamani, E. Santillan-Jimenez, M. Martinelli, W. D. Shafer, S. D. Hopps, N. Wanninayake, and D. Y. Kim, "Effect of Metal Work Function on Hydrogen Production from Photocatalytic Water Splitting with MTiO
2
Catalysts," *ChemistrySelect,* vol. 5, no. 3, pp. 1013-1019, 2020.
[130] J. Yuan, E. S. Choo, X. Tang, Y. Sheng, J. Ding, and J. Xue, "Synthesis of ZnO-Pt nanoflowers and their photocatalytic applications," *Nanotechnology,* vol. 21, no. 18, pp. 185606(1-11), May 7 2010.
[131] C. P. T. Nguyen, T. T. Trinh, J. Raja, A. H. T. Le, Y.-J. Lee, V. A. Dao, and J. Yi, "Source/drain metallization effects on the specific contact resistance of indium tin zinc oxide thin film transistors," *Materials Science in Semiconductor Processing,* vol. 39, pp. 649-653, 2015.
[132] L. P. B. Lima, H. F. W. Dekkers, J. G. Lisoni, J. A. Diniz, S. Van Elshocht, and S. De Gendt, "Metal gate work function tuning by Al incorporation in TiN," *Journal of Applied Physics,* vol. 115, no. 7, pp. 074504(1-6), 2014.
[133] H. Helal, Z. Benamara, M. B. Arbia, A. Rabehi, A. C. Chaouche, and H. Maaref, "Electrical behavior of n-GaAs based Schottky diode for different contacts: Temperature dependence of current-voltage," *International Journal of Numerical Modelling: Electronic Networks, Devices and Fields,* vol. In press, 2021.
[134] S. M. Hong, H.-D. Kim, H.-M. An, and T. G. Kim, "Effect of Work Function Difference Between Top and Bottom Electrodes on the Resistive Switching Properties of SiN Films," *IEEE Electron Device Letters,* vol. 34, no. 9, pp. 1181-1183, 2013.

[135] S. Liu, S. Dong, H. Jin, S. Huang, X. Wang, and J. Luo, "Significant Effects of Electrode Metal Work Function on Resistive Memory Devices with Gelatin Biodielectric Layer," *Journal of The Electrochemical Society,* vol. 165, no. 7, pp. G90-G95, 2018.

[136] Y. Qi, C. Z. Zhao, C. Liu, Y. Fang, J. He, T. Luo, L. Yang, and C. Zhao, "Comparisons of switching characteristics between Ti/Al_2O_3/Pt and TiN/Al_2O_3/Pt RRAM devices with various compliance currents," *Semiconductor Science and Technology,* vol. 33, no. 4, pp. 045003(1-17), 2018.

[137] C. S. H. B. Jain, D. Misra, K. Tapily, R.D. Clark, S. Consiglio, C.S. Wajda, and G.J. Leusink, "Multilevel Resistive Switching in Hf-Based RRAM," *ECS Transactions,* vol. 89, no. 3, pp. 39-44, 2019.

[138] S. Kim, H. Kim, S. Jung, M.-H. Kim, S.-H. Lee, S. Cho, and B.-G. Park, "Tuning resistive switching parameters in Si_3N_4-based RRAM for three-dimensional vertical resistive memory applications," *Journal of Alloys and Compounds,* vol. 663, pp. 419-423, 2016.

[139] Y. He, G. Ma, X. Zhou, H. Cai, C. Liu, J. Zhang, and H. Wang, "Impact of chemical doping on resistive switching behavior in zirconium-doped $CH_3NH_3PbI_3$ based RRAM," *Organic Electronics,* vol. 68, pp. 230-235, 2019.

[140] M. D. Debanjan Jana, Subhranu Samanta and Siddheswar Maikap, "RRAM characteristics using a new Cr/GdOx/TiN structure," *Nanoscale Research Letters,* vol. 9, pp. 680(1-9), 2014.

[141] F. Y. Yuan, N. Deng, C. C. Shih, Y. T. Tseng, T. C. Chang, K. C. Chang, M. H. Wang, W. C. Chen, H. X. Zheng, H. Wu, H. Qian, and S. M. Sze, "Conduction Mechanism and Improved Endurance in HfO_2-Based RRAM with Nitridation Treatment," *Nanoscale Res Lett,* vol. 12, no. 1, pp. 574(1-6), Oct 26 2017.

[142] A. N. Rodrigues, Y. P. Santos, C. L. Rodrigues, and M. A. Macêdo, "Al_2O_3 thin film multilayer structure for application in RRAM devices," *Solid-State Electronics,* vol. 149, pp. 1-5, 2018.

[143] T. S. Bhat, C. C. Revadekar, S. S. Patil, T. D. Dongale, D.-k. Kim, and P. S. Patil, "Photo-induced resistive switching in CdS-sensitized TiO_2 nanorod array memristive device," *Journal of Materials Science: Materials in Electronics,* vol. 31, no. 13, pp. 10919-10929, 2020.

[144] H.-D. Kim, M. J. Yun, and S. Kim, "Resistive switching characteristics of Al/Si_3N_4/p-Si MIS-based resistive switching memory devices," *Journal of the Korean Physical Society,* vol. 69, no. 3, pp. 435-438, 2016.

[145] F. Lyu, Y. Bai, Q. Wang, L. Wang, X. Zhang, and Y. Yin, "Coordination-assisted synthesis of iron-incorporated cobalt oxide nanoplates for enhanced oxygen evolution," *Materials Today Chemistry,* vol. 11, pp. 112-118, 2019.

[146] B. Sun, Y. Qian, Z. Liang, Y. Guo, Y. Xue, J. Tian, and H. Cui, "Oxygen vacancy-rich BiO_{2-x} ultra-thin nanosheet for efficient full-spectrum responsive photocatalytic oxygen evolution from water splitting," *Solar Energy Materials and Solar Cells,* vol. 195, pp. 309-317, 2019.

[147] J. T. Mefford, A. A. Kurilovich, J. Saunders, W. G. Hardin, A. M. Abakumov, R. P. Forslund, A. Bonnefont, S. Dai, K. P. Johnston, and K. J. Stevenson,

"Decoupling the roles of carbon and metal oxides on the electrocatalytic reduction of oxygen on $La_{1-x}Sr_xCoO_3$-delta perovskite composite electrodes," *Phys Chem Chem Phys,* vol. 21, no. 6, pp. 3327-3338, Feb 6 2019.

[148] S. Cook, M. T. Dylla, R. A. Rosenberg, Z. R. Mansley, G. J. Snyder, L. D. Marks, and D. D. Fong, "The Vacancy-Induced Electronic Structure of the $SrTiO_{3-\delta}$ Surface," *Advanced Electronic Materials,* vol. 5, no. 1, pp. 1800460(1-9), 2018.

Chapter 3: Electrical performance for RRAM devices with stacked solution-processed GaO_x/AlO_x dielectric

With the investigation results in **Chapter 2**, the best RS behaviors could be obtained in the SP-AlO_x layer with the annealing temperature of 250°C. However, it is worth considering enhancing the performance of the RRAM with the structure of Ni/SP-AlO_x/Pt. The enhancement of device performance can be realized by improving the electrode layer and RS layer. For the electrode layer improvement of the device, generally, the materials of TE and BE have high electrical conductivity, and there is an appropriate difference between the material activities of TE and BE layers. [10, 64] For the improvement techniques of the RS layer, it is usually to investigate doping of hybrid materials and layered processing. [79, 149-155] Whether it is the improvement of the electrode layer or the RS layer, the final goal of these improvement techniques is to obtain the RRAM device with a lower operation voltage, a larger ON/OFF ratio, and better reliability.

In this chapter, the improvement of electrode and RS layers of the previous Ni/SP-AlO_x/Pt RRAM device was conducted at the same time. Some evidence has pointed that RRAM devices based on metallic CF could demonstrate lower operation voltage than oxygen-vacancy-based devices, and the formation/rupture process was easier to modulate. [10, 47, 49, 51, 64, 156, 157] Therefore, Ag, which is easily oxidized, was selected as the candidate of the TE layer due to its high activity. [158, 159] Besides, indium tin oxide was selected as the candidate of the BE layer due to its high electrical conductivity,

high transparency, and better hydrophilia. [160-162] On the other hand, based on the consideration of fabrication efficiency and economic cost, the RS layer with a stacked structure was chosen and the SP-AlO_x layer was still utilized, which indicated a metallic-CF-based RRAM device with the structure of Ag/SP-X/SP-AlO_x/ITO. For now, some researchers have demonstrated that the improvement with stacked RS layers could show enhanced electrical performance with higher efficiency. [80, 163-170] For instance, Jung Ho Yoon et al. proposed the RRAM device with the Ta_2O_5/HfO_2 stack. The HfO_2 layer played the role of switching layer through trapping or de-trapping of electronic carriers while the Ta_2O_5 layer remained intact during the whole switching cycle and provided the rectification [166]. They also researched the RS performance of the TiO_2/HfO_2 resistive switching material system. TiO_2 layer worked as the rectification layer due to its high k-value (~40) and low bandgap (~3.2 eV). The Pt/TiO_2 interface served as a fluent Schottky interface and provided the device with the desirable rectifying characteristics when the spurious effect can be feasibly suppressed. [168]. These results proved the reliable prospect of MO materials and stack RS layer structure in the research of RRAM. The metallic CF in the RRAM device was always associated with oxidation and reduction reactions of the metal component, which indicated that a certain degree of oxidation difference was required between the SP-X layer and the SP-AlO_x layer. [10, 51, 64] Therefore, some RRAM devices with single SP RS layers such as gallium oxide (GaO_x), indium oxide (InO_x), and graphene oxide (GO) were investigated and the 2.5 M SP-GaO_x layer was chosen as the upper candidate of the SP-X layer. After the experimental and comparison process, the Ag/SP-GaO_x/SP-

AlO_x/ITO RRAM device displayed enhanced electrical performance in terms of an operation voltage lower than 0.6 V, an ON/OFF ratio larger than 2×10^4, a retention time longer than 2×10^4 s, and retention cycles over 200. [51]

3.1 Experimental

3.1.1 For Ag/SP-X/ITO RRAM devices with a single RS layer

The precursor solutions of different RS layers were prepared according to the experimental process mentioned in section 2.1.1 of **Chapter 2**. With similar methods, precursor solutions of 2.5 M AlO_x (~ 5 mL DI water + ~ 4.6765 g $Al(NO_3)_3\cdot9H_2O$), 2.5 M GaO_x (~ 5 mL DI water + ~ 3.4368 g $Ga(NO_3)_3\bullet xH_2O$), and 2.5 InO_x (~ 5 mL DI water + ~ 3.9856 g $In(NO_3)_3\bullet xH_2O$) were obtained. For the GO precursor suspension, the GO powder was purchased from Nanjing XFNANO Materials Tech Co., Ltd and the concentration was 0.1 mg/mL (~ 5 mL DI water + ~ 0.5 mg GO). The composition of all precursor solutions and suspension could be observed in **Table 3-1**. After the same ultrasonic cleaning operation was applied onto the ITO substrate, precursor solution or suspension were spin-coated onto the cleaned substrate, respectively. The annealing temperature for all materials was the same 250°C and the time of the annealing process was 1 hour. Finally, a 40-nm Ag layer and a 40-nm Al layer were thermally evaporated onto the RS layer as a TE layer and a capping layer. Fabricated devices with the structure of Ag/SP-AlO_x/ITO, Ag/SP-GaO_x/ITO, Ag/SP-InO_x/ITO, and Ag/SP-GO/ITO were obtained.

Table 3-1. Composition of all precursor solutions and suspension

RS layer	Solute	Solvent	Concentration
SP-AlO_x	4.6765 g $Al(NO_3)_3 \cdot 9H_2O$	5 mL DI water	2.5 M
SP-GaO_x	3.4368 g $Ga(NO_3)_3 \bullet xH_2O$	5 mL DI water	2.5 M
SP-InO_x	3.9856 g $In(NO_3)_3 \bullet xH_2O$	5 mL DI water	2.5 M
SP-GO	0.5 mg GO	5 mL DI water	0.1 mg/mL

3.1.2 For Ag/SP-GaO_x/SP-AlO_x/ITO RRAM device with a stacked RS layer

Based on the fundamental operations of section 3.1.1, an SP-AlO_x layer was deposited onto the ITO layer at first. Then an SP-GaO_x layer was deposited onto the SP-AlO_x layer with the same technique. Electrodes Al and Ag were all cylindrical and the diameter of each cylindrical electrode was 0.1 mm. **Fig. 3-1a** showed the schematic view of and fabricated Al/Ag/SP-GaO_x/SP-AlO_x/ITO RRAM device. A 50-nm SP-AlO_x layer and a 35-nm SP-GaO_x layer were observed in **Fig. 3-1b**.

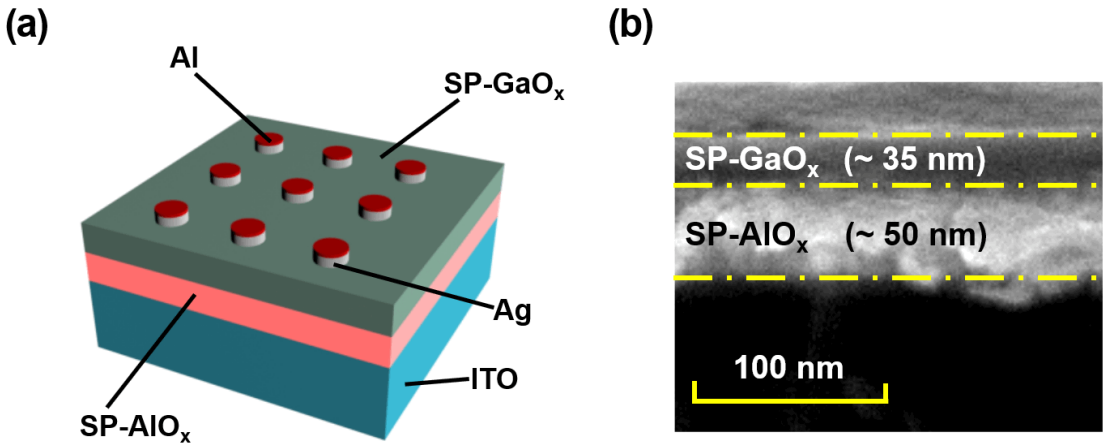

Figure 3-1. (a) Schematic view of Al/Ag/SP-GaO_x/SP-AlO_x/ITO RRAM devices. (b) SEM image of an Ag/SP-GaO_x/SP-AlO_x/ITO RRAM device.

3.2 Electrical performance of Ag/SP-X/ITO RRAM devices based on various RS materials

The electrical characterization of all RRAM devices was still conducted by an Agilent B1500A high-precision semiconductor analyzer. During the comparison phase in this section, some factors such as operation voltage, ON/OFF ratio, distribution of resistance values, endurance, and retention. Among these indexes, the first priority was the operation voltage. The lower operation voltage indicated that the oxidation of Ag was easier to occur in the RS layer. [61-63, 171, 172] The ON/OFF ratio was considered with the second priority because the larger switching meant the larger storage capacity. [61, 172] **Fig. 3-2** showed the statistical results of related electrical indexes, which included V_{SET} (**Fig. 3-2a**), V_{RESET} (**Fig. 3-2b**), ON/OFF ratio (**Fig. 3-2c**), and resistance distribution (**Fig. 3-2d**). In **Figs. 3-2a** and **3-2b**, compared with the Ag/SP-AlO_x/ITO RRAM device, lower operation voltages of SET and RESET processes were observed in Ag/SP-GaO_x/ITO, Ag/SP-InO_x/ITO, and Ag/SP-GO/ITO RRAM devices, which indicated that Ag was easier oxidized in SP-GaO_x, SP-InO_x, and SP-GO layers. Compared with the SP-GO-based device, devices with SP-GaO_x and SP-InO_x layers showed lower operation voltages. In **Fig. 3-2c**, Ag/SP-GaO_x/ITO device exhibited a similar ON/OFF ratio to Ag/SP-GO/ITO devices. The smallest switching ratio was observed in Ag/SP-InO_x/ITO, which was even smaller than half of the switching ratio of Ag/SP-GaO_x/ITO devices. For now, previous evidence has supported that better electrical performance could be obtained with RRAM devices with SP-GaO_x and SP-InO_x layers. Although the Ag/SP-InO_x/ITO device showed a lower V_{SET}, considering

the extremely small switching ratio of the Ag/SP-InO_x/ITO device, and the acceptable voltage difference (< 1.0 V) between Ag/SP-GaO_x/ITO and Ag/SP-InO_x/ITO RRAM devices, the SP-GaO_x layer was chosen as the candidate of the SP-X layer.

In order to make the investigation on data distribution of resistance values among these RRAM devices with single SP RS layers, standard deviation and variation coefficient mentioned above were used to evaluate the resistance distribution illustrated in **Fig. 3-2d.** Related statistic results could be obtained in **Tables 3-2** and **3-3**. The difference of endurance variation coefficient between Ag/SP-GaO_x/ITO and Ag/SP-InO_x/ITO RRAM devices was smaller than 0.1 at HRS and LRS, which was acceptable and indicated the similar stability between Ag/SP-GaO_x/ITO and Ag/SP-InO_x/ITO RRAM devices.

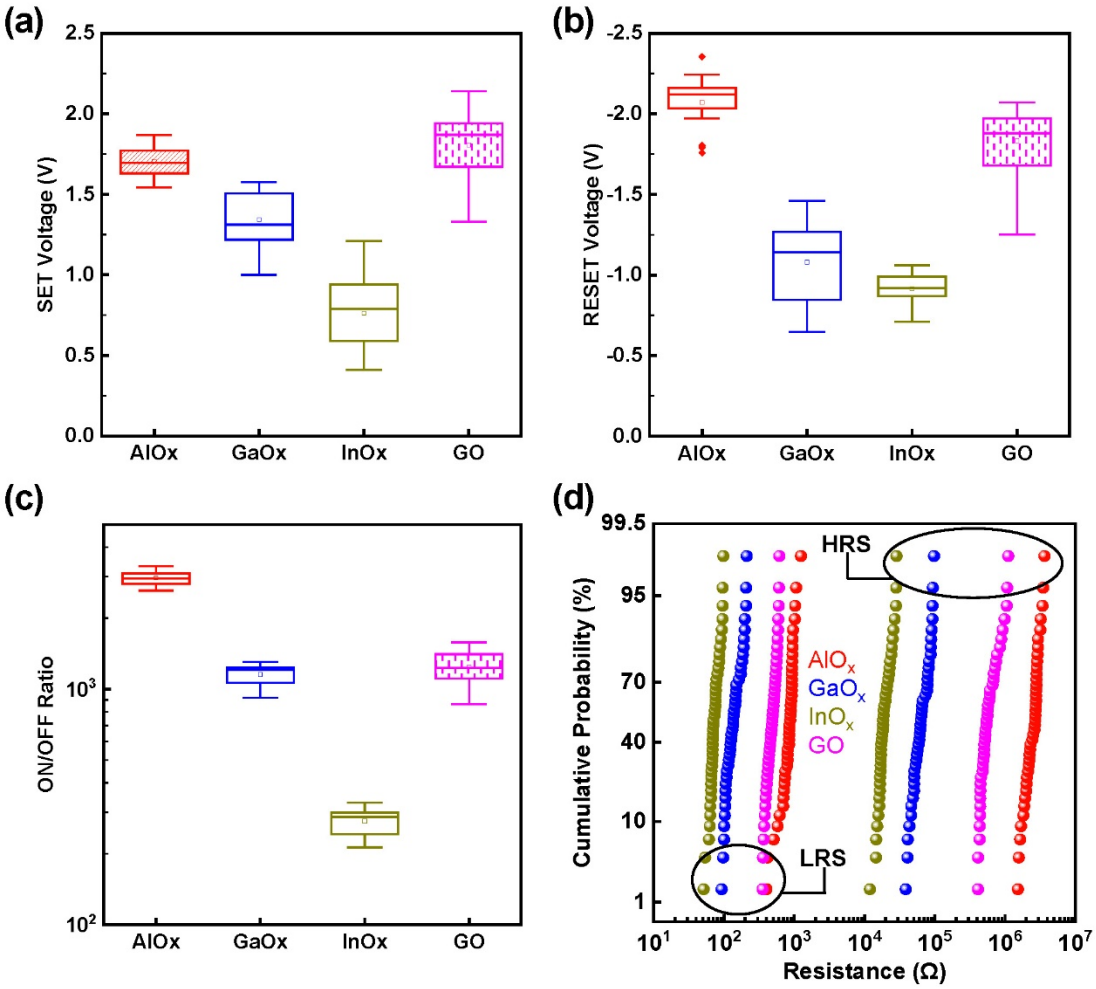

Figure 3-2. Statistic results of the electrical performance of Ag/SP-AlO_x/ITO, Ag/SP-GaO_x/ITO, Ag/SP-InO_x/ITO, and Ag/SP-GO/ITO, including (a) V_{EST}, (b) V_{RESET}, (c) ON/OFF ratio, and (d) resistance distribution.

In addition, the measurement of endurance and retention properties of Ag/SP-AlO_x/ITO, Ag/SP-GaO_x/ITO, Ag/SP-InO_x/ITO, and Ag/SP-GO/ITO RRAM devices were obtained in **Fig. 3-3**. Resistance values of HRS and LRS for each device were read at 0.1 V. The quantitative assessment on the distribution of HRS and LRS values during endurance measurements was presented in **Tables 3-2** and **3-3**, which indicated that it was appropriate to use the SP-GaO_x layer as the improved layer of the stacked SP-X/SP-AlO_x layer.

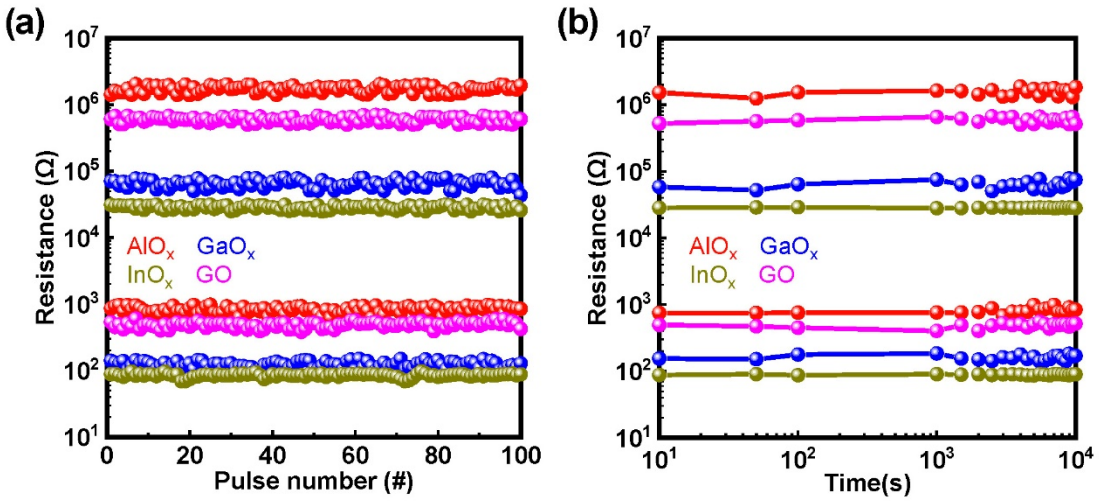

Figure 3-3. Endurance and retention performance of Ag/SP-AlO_x/ITO, Ag/SP-GaO_x/ITO, Ag/SP-InO_x/ITO, and Ag/SP-GO/ITO.

Table 3-2. Standard deviation of resistance distribution and endurance for RRAM devices with a single SP RS layer

Samples	Resistance state	Resistance distribution	Endurance values
Ag/SP-AlO_x/ITO	LRS	165.02509	86.61476
Ag/SP-AlO_x/ITO	HRS	105914.41134	54602.57567
Ag/SP-GaO_x/ITO	LRS	35.53483	13.17800
Ag/SP-GaO_x/ITO	HRS	17058.18702	8692.78413
Ag/SP-InO_x/ITO	LRS	11.40099	5.04359
Ag/SP-InO_x/ITO	HRS	4111.97226	1992.03368
Ag/SP-GO/ITO	LRS	76.95325	45.90578
Ag/SP-GO/ITO	HRS	195750.98183	55829.75706

Table 3-3. Variation coefficient of resistance distribution and endurance for RRAM devices with a single SP RS layer

Samples	Resistance state	Resistance distribution	Endurance values
Ag/SP-AlO_x/ITO	LRS	0.19771	0.10818
Ag/SP-AlO_x/ITO	HRS	0.20996	0.08513
Ag/SP-GaO_x/ITO	LRS	0.25035	0.10697
Ag/SP-GaO_x/ITO	HRS	0.25758	0.13336
Ag/SP-InO_x/ITO	LRS	0.15339	0.05937
Ag/SP-InO_x/ITO	HRS	0.20886	0.07022
Ag/SP-GO/ITO	LRS	0.15921	0.09436
Ag/SP-GO/ITO	HRS	0.31666	0.09412

3.3 Performance comparison between Ag/SP-GaO_x/SP-AlO_x/ITO and Ag/SP-AlO_x/ITO RRAM devices

Based on the results of the previous section, the SP-GaO_x layer was chosen as the upper part of the stacked RS layer, which referred to the improved RRAM device with the structure of Ag/SP-GaO_x/SP-AlO_x/ITO. The comparison between Ag/SP-GaO_x/SP-AlO_x/ITO and Ag/SP-AlO_x/ITO RRAM devices was used to reveal the successful improvement of the device performance. Before starting the research on the performance variation between these two devices, the physical characterization with XPS was presented to prove the successful deposition of the SP-GaO_x layer onto the SP-AlO_x layer, as illustrated in **Fig. 3-4**. **Figs. 3-4a** and **3-4b** demonstrated the O 1s and Al 2p spectra of the SP-AlO_x layer while the O 1s and Ga 2p spectra of the SP-GaO_x layer were observed in **Figs. 3-4c** and **3-4d**. The peak in **Fig. 3-4a** with the binding energy located at 531.9 eV indicated the existence of Al_2O_3 in the SP-AlO_x layer while the peak at 72.6 eV of the Al 2p spectrum (**Fig. 3-4b**) revealed that there were metallic Al components in the SP-AlO_x layer. [173-175] In addition, in the SP-GaO_x layer, the Ga_2O_3 was pointed by the peak located at 631.7 eV in the O 1s spectrum (**Fig. 3-4c**) and the single peak located at 1117.1 eV in the Ga 2p spectrum (**Fig. 3-4d**). [173-177] The results of XPS spectra proved that the SP-GaO_x layer was successfully spin-coated onto the deposited SP-AlO_x layer.

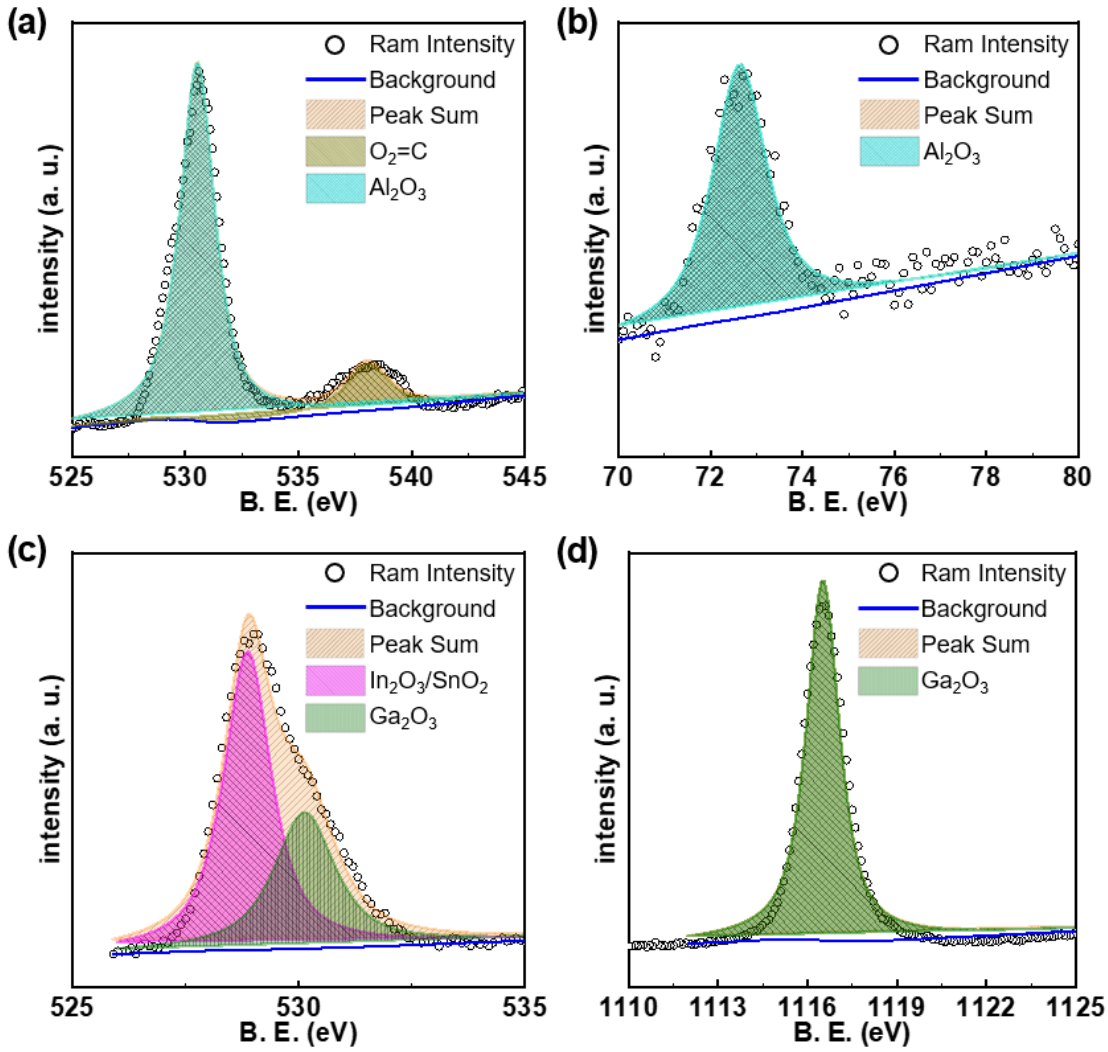

Figure 3-4. XPS spectra results for (a) O 1s spectrum and (b) Al 2p spectrum of the SP-AlO_x layer. XPS spectra results for (a) O 1s spectrum and (b) Ga 2p spectrum of the SP-GaO_x layer.

With the I_{CC} at 1 mA, the bipolar I-V curves of Ag/SP-GaO_x/SP-AlO_x/ITO and Ag/SP-AlO_x/ITO RRAM devices were presented in **Fig. 3-5a** and **Fig. 3-5b**, respectively. For the Ag/SP-GaO_x/SP-AlO_x/ITO RRAM device, a forming operation with high voltage at ~ 2.3 V was required before starting the stable SET and RESET processes. Compared with the device based on the stacked SP-GaO_x/SP-AlO_x layer, the forming voltage of the Ag/SP-AlO_x/ITO device was approximately equal to the voltage of the first SET operation. Therefore, the Ag/SP-AlO_x/ITO RRAM device was considered as the

forming-free device. [154, 178, 179] Based on the I-V curves presented in **Fig. 3-5**, compared with the Ag/SP-AlO_x/ITO RRAM device, the Ag/SP-GaO_x/SP-AlO_x/ITO RRAM device demonstrated improved electrical performance with lower operation voltage and larger ON/OFF ratio. In the supplementary information, **Fig. SI-2** demonstrated the device-to-device variation of the formation voltages for Ag/SP-AlO_x/ITO and Ag/SP-GaO_x/SP-AlO_x/ITO RRAM devices. **Figs. SI-2a** and **b** showed the IV curves of the forming process. Also, 20 samples of each kind of RRAM device were chosen to investigate the device-to-device variation of forming voltages and the results could be observed in **Figs. SI-2c** and **d**. As illustrated in **Fig. SI-2**, both Ag/SP-GaO_x/SP-AlO_x/ITO and Ag/SP-AlO_x/ITO RRAM devices demonstrated a stable forming process. The forming voltage of the Ag/SP-GaO_x/AlO_x/ITO RRAM device was higher than the SET voltage of the Ag/SP-GaO_x/SP-AlO_x/ITO RRAM device while the forming and SET voltages of the Ag/SP-AlO_x/ITO RRAM device was very similar. In addition, an obvious backward scan effect was also observed on the Ag/SP-AlO_x/ITO RRAM device, as illustrated in **Fig. SI-3**. In general, the backward scan effect was usually observed on SiO_x-based RRAM devices. [180-184] Before the sweep voltage reaches the stop voltage of SET operation at HRS, the current will decrease abruptly. The current value is mostly lower than the compliance current (CC) and then begins to fluctuate near this level. The device is still at HRS. When the sweep voltage reaches the stop voltage of SET operation, the device starts to enter the LRS [180-184]. However, there is a little difference between the typical backward scan effect of SiO_x RRAM devices and the performance of the Ag/AlO_x/ITO RRAM devices. **Fig. SI-3a** showed the

backward scan effect of the SiO_x RRAM device [181]. During the forward sweep in the electroforming process, current fluctuations occur at about 1 μA followed by a backward sweep that forms a switchable filament, even if the electroforming process is momentarily stopped (see step 1 to step 3 in **Fig. SI-3a** where the backward sweep was stopped at 8 V in the electroforming process, the state was checked at 1 V followed by a set process). The backward-scan effect can also be observed in the reset process, where the device changes from HRS to LRS if the backward scan is done slowly (step 4 in **Fig. SI-3a**). In **Fig. SI-3b**, the current decreased obviously in step 2 and then fluctuate at this level until the SET voltage occurred. Compared with **Fig. SI-3a**, the most different was the change tendency of step 4 of the Ag/AlO_x/ITO device. The device was directly switched into LRS at CC. However, for the Ag/SP-GaO_x/SP-AlO_x/ITO RRAM device, there was no such backward scan effect. Therefore, the backward scan effect of the Ag/SP-AlO_x/ITO device might be associated with the redox of RS layers and the non-uniformity of CF [8, 164, 185-189]. Due to the low redox rate of the AlO_x layer, It was difficult for Ag atoms to completely transform into Ag ions smoothly in a short time with the voltage bias applied onto the Ag electrode [164, 185-187]. As illustrated in **Fig. SI-3b**, when the sweep voltage reached around 1.3 V in the forming process, the current decreased abruptly to 10^{-6} A level, which might be resulted from the incomplete and heterogeneous Ag CF formed in the RRAM device [8, 188, 189]. The incomplete Ag CF resulted in the current fluctuations at 10^{-6} A level, which was very like the backward scan effect.

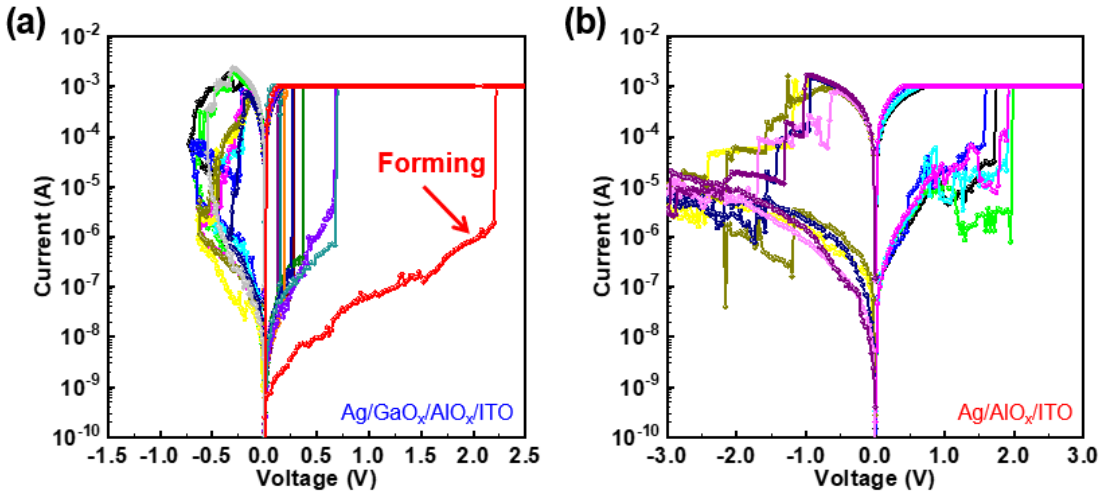

Figure 3-5. Bipolar I-V characteristics of (a) Ag/SP-GaO_x/SP-AlO_x/ITO and (b) Ag/SP-AlO_x/ITO RRAM devices.

With the statistical results illustrated in **Fig. 3-6**, it has been confirmed that the Ag/SP-GaO_x/SP-AlO_x/ITO RRAM device exhibited improved RS behavior with lower operation voltage, larger switching ratio, and enhanced device stability. The average amplitudes of V_{SET} and V_{RESET} were around ~ 0.6 V and the maximum value was 0.8 V. The quantitative statistical results of resistance distribution were presented in **Table 3-4** with standard deviation and variation coefficient. Both Ag/SP-GaO_x/SP-AlO_x/ITO and Ag/SP-AlO_x/ITO RRAM devices demonstrated excellent device stability. While smaller values of standard deviation and variation coefficient indicated the better stability of the Ag/SP-GaO_x/SP-AlO_x/ITO RRAM device.

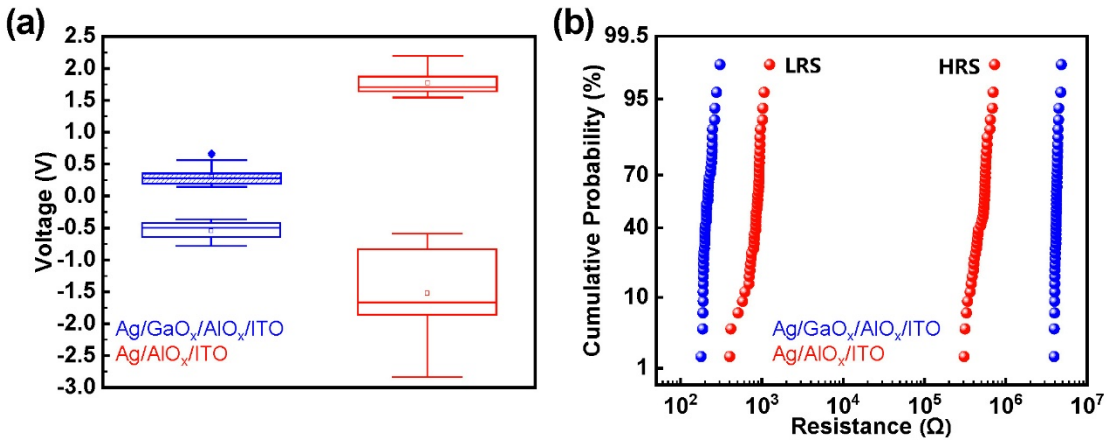

Figure 3-6. Statistic results on (a) voltage distribution and (b) resistance distribution of Ag/SP-GaO_x/SP-AlO_x/ITO and Ag/SP-AlO_x/ITO RRAM devices.

Table 3-4. Standard deviation and variation coefficient of resistance distribution for Ag/SP-GaO_x/SP-AlO_x/ITO and Ag/SP-AlO_x/ITO RRAM devices

Samples	Resistance state	Standard deviation	variation coefficient
Ag/SP-GaO_x/SP-AlO_x/ITO	LRS	28.28755	0.13017
Ag/SP-GaO_x/SP-AlO_x/ITO	HRS	193062.97470	0.04587
Ag/SP-AlO_x/ITO	LRS	165.02509	0.19771
Ag/SP-AlO_x/ITO	HRS	105914.41134	0.20996

To a certain extent, the quantitative statistical results of resistance distribution have indicated the stability of the Ag/SP-GaO_x/SP-AlO_x/ITO RRAM device. The measurement of retention and endurance properties could more fully prove this remarkable device stability. All resistance values of HRS and LRS were read at 0.1 V. The retention in **Fig. 3-7a** indicated that the Ag/SP-GaO_x/SP-AlO_x/ITO RRAM device could maintain the information longer than 2×10^4 s with the stable ON/OFF ratio around ~ 2×10^4. The endurance in **Fig. 3-7b** proved that the number of writing & erasing behavior cycles could be over 1000. **Table 3-5** presented the quantitative statistical results of the endurance comparison between Ag/SP-GaO_x/SP-AlO_x/ITO and

Ag/SP-AlO_x/ITO RRAM devices, which also supported that better electrical performance was obtained with the improvement operations of RS and electrode layers.

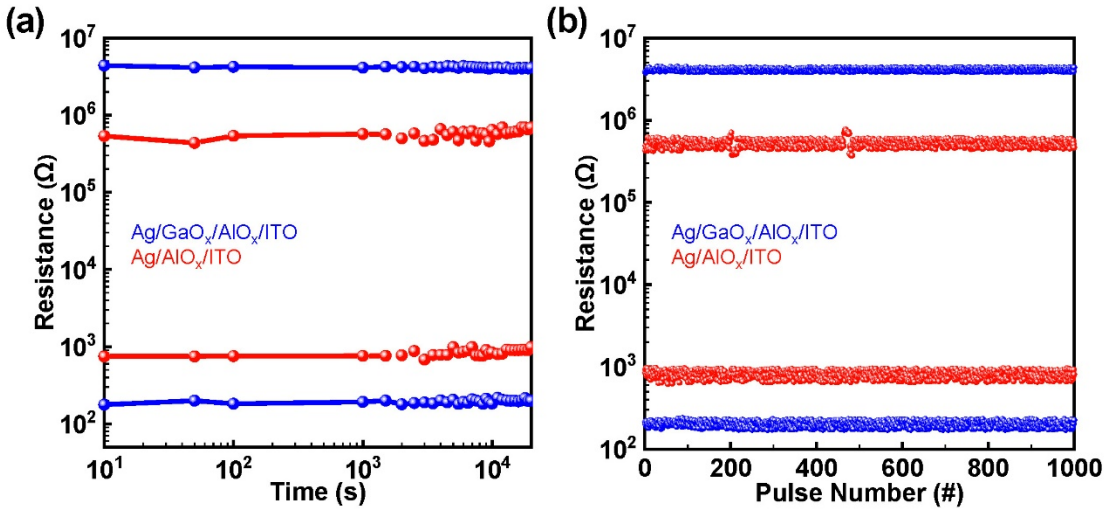

Figure 3-7. (a) Endurance and (b) retention performance of Ag/SP-GaO_x/SP-AlO_x/ITO and Ag/SP-AlO_x/ITO RRAM devices.

Table 3-5. Standard deviation and variation coefficient of endurance for Ag/SP-GaO_x/SP-AlO_x/ITO and Ag/SP-AlO_x/ITO RRAM devices

Samples	Resistance state	Standard deviation	variation coefficient
Ag/SP-GaO_x/SP-AlO_x/ITO	LRS	17.05981	0.10470
Ag/SP-GaO_x/SP-AlO_x/ITO	HRS	158929.24778	0.03882
Ag/SP-AlO_x/ITO	LRS	86.61476	0.10818
Ag/SP-AlO_x/ITO	HRS	54602.57567	0.08513

To prove the excellent RS performance of the Ag/SP-GaO_x/SP-AlO_x/ITO RRAM device, a brief comparison among devices with MO materials was conducted in **Table 3-6**. [7, 190-197] Compared with conventional fabrication methods of RS thin films, emerging methods represented by the SP methods have demonstrated their positive characteristics, such as low fabrication cost with the elimination of vacuum deposition

processes, easy acquisition of precursor materials, and high-efficiency throughput of devices. [198-202] During the comparison, the SP-GaO_x/SP-AlO_x RRAM devices demonstrated lower operation voltage, higher ON/OFF ratio, and excellent stability, which indicated the power consumption of SP-GaO_x/SP-AlO_x RRAM devices was lower.

Table 3-6. Comparison among RRAM devices with RS layers fabricated with various materials

RS layer	Thickness (nm)	$V_{forming}$ (V)	V_{SET} (V)	V_{RESET} (V)	on/off ratio	Endurance (cycles)	Retention (s)	Fabrication method
TiO_x/AlO_x	~24	~2.0	~0.8	~1.0	$>10^3$	120	N. A.	ALD
Ta_2O_5	~15	~1.0	~0.6	~1.0	>100	N. A.	N. A.	ALD
TiO_x	~15	~6.0	~4.0	~4.5	$>10^4$	$4x10^3$	10^4	ALD
TiO_2	~60	Free	~4.0	~3.8	>300	100	10^4	SP
ZnO	~130	Free	~1.0	~2.0	~100	200	5000	SP
CeO_2/ZrO_2	~100	Free	~1.5	~2.0	$>10^3$	100	10^5	SP
ZnO	~60	Free	~2.5	~1.5	$>10^4$	300	10^8	Sputtering
Gd_2O_3	~45 - ~8	Free	~1.0	~2.0	>600	100	10^4	Sputtering
HfO_2/ZrO_2	~12	Free	~1.0	~1.5	>100	1000	10^4	Sputtering
GaO_x/AlO_x	~80	~2.2	~0.8	~1.0	$>10^4$	100	10^4	SP

3.4 Mechanism analysis of Ag/SP-GaO_x/SP-AlO_x/ITO RRAM devices

Previous results have proved that electrically improvement was obtained in the Ag/SP-GaO_x/SP-AlO_x/ITO, which was associated with the mechanism replacement of oxygen-vacancy CF to metallic CF. Before starting the further discussion on the switching mechanism, it was necessary to determine whether metallic CF was playing the dominating role during the switching process. As illustrated in **Fig. 3-8**, the

measurement of metallic temperature dependency was carried out on both Ag/SP-GaO_x/SP-AlO_x/ITO and Ag/SP-AlO_x/ITO RRAM devices, which followed the equation 3-1 (**Eq. 3-1**): [203, 204]

$$R(T) = R_0[1 + k(T - T_0)]^2 \quad \textbf{(Eq. 3-1)}$$

where *R(T)* was the instantaneous resistance of the RRAM device at the desired temperature *T*, R_0 was the and initial resistance of the device at the initial environmental temperature T_0. For the fitting process, the independent variable was temperature *T* while the dependent variable was presented with the form of R/R_0, which could provide a more intuitive description of the relationship function. The linear relationship between R/R_0 and *T* indicated that the linear increase of LRS resistance occurred with the increase of the environment temperature, which pointed to the metallic characteristics of Ag/SP-GaO_x/SP-AlO_x/ITO and Ag/SP-AlO_x/ITO RRAM devices. [49, 51, 171] Also, some other researchers used the activation energy (E_a) to explore the switching mechanism, which was an indicating role of switching location where CF raptured. Chen et al. utilized the activation energy (E_a) extraction methodology to investigate the relaxation properties with the resistive switching identification method, which provided insights and design guidance for non-uniform bilayer selectorless 1R-only RRAM array applications [205]. However, the E_a extraction method might make more sense for research on 1R-only or 1T-1R RRAM arrays. In addition, the E_a is also associated with the environmental temperature during the measurement process. In this work, the most

important research was to investigate the performance variation between single-layer devices and bilayer devices. Therefore, it was ensured that the only difference between single layer and bilayer devices was the existence of the SP-GaO_x layer. That is to say, the temperature of fabrication and measurement of these two kinds of devices were totally the same. Hence, the metallic measurement was conducted to understand the switching mechanism. In addition, the SP-AlO_x has been accepted as a good oxygen reservoir by many researchers, which was also confirmed by the thesis work in **Chapter 2** [206-210]. However, the RS performance and RS mechanism are not only decided by the RS layer but also affected by the electrode layer. More AlO_x RRAM devices with active electrodes like Cu and Ag agreed with the role of metallic filament [208, 211-218]. Therefore, the measurement of a metallic characteristic for Ag/SP-AlO_x/ITO and Ag/SP-GaO_x/SP-AlO_x/ITO RRAM devices could exclude the influence of oxygen vacancy in SP-AlO_x and SP-GaO_x layers.

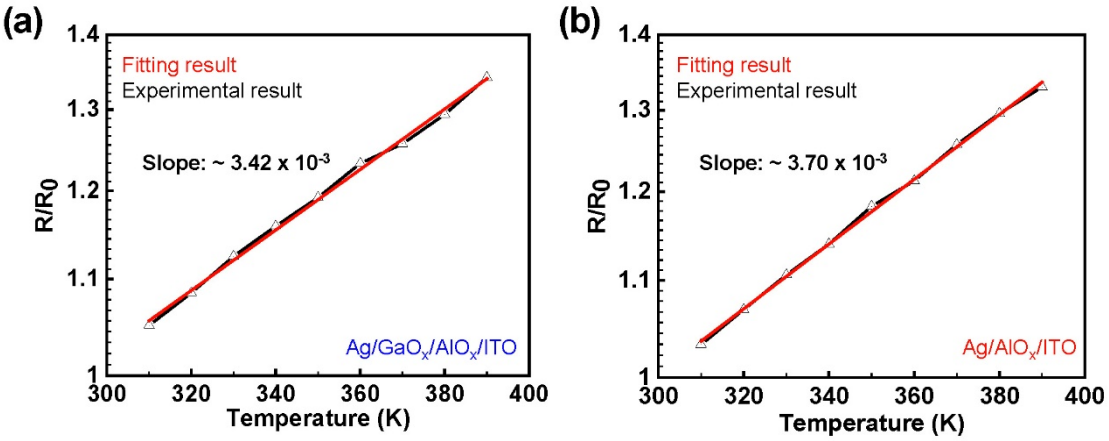

Figure 3-8. Metallic temperature dependency of (a) Ag/SP-GaO_x/SP-AlO_x/ITO and (b) Ag/SP-AlO_x/ITO RRAM devices at LRS.

Based on the LRS metallic behavior of the temperature dependency of the Ag/SP-

GaO_x/SP-AlO_x/ITO RRRAM device, metallic CFs were considered to be dominant during the RS process. [10, 43, 61, 62, 64, 204, 219-222] **Figs. 3-9a** to **3-9d** provided that schematic diagram of the RS process. The initial HRS state (initial OFF) of the RRAM device with a stacked RS layer was observed in **Fig. 3-9a**, including an Ag TE layer, an ITO BE layer, and an SP-GaO_x/SP-AlO_x RS layer. In **Fig. 3-9b**, when the + V was applied onto the TE layer, electrons (gray balls, e^-) driven by the external electric field moved from BE ITO to TE Ag while Ag ions (red balls, Ag^+) were generated from TE Ag and drifted to BE ITO due to the oxidation reaction, which could be described by the equation 3-2 (**Eq. 3-2**): [43, 204, 219]

$$Ag \rightarrow Ag^+ + e^- \qquad \textbf{(Eq. 3-2)}$$

After reaching BE ITO, Ag^+ met with e^- and re-combined to be new-generated Ag atoms (orange balls), which was considered as the reduction reaction and followed the equation 3-3 (**Eq. 3-3**): [43, 204, 219-222]

$$Ag^+ + e^- \rightarrow Ag \qquad \textbf{(Eq. 3-3)}$$

With the continuous new generation, the accumulation of new-generated Ag atoms resulted in the formation of metallic CFs based on Ag atoms induced by the redox reaction (**Fig. 3-9c**). During the RESET process, with the negative voltage added onto TE Ag, partially formed metallic CFs broken due to the Joule-heating effect, and then

the device was at HRS (**Fig. 3-9d**). [10, 32, 64, 79, 223] Some other work also supported the Joule-heating effect. [32, 43, 224-227] The Joule-heating effect influenced not only metallic filaments but also filaments composed of non-metal materials, but the effect of Joule heating was more obvious on metallic filaments during the RESET process. Imanishi et al. investigated the RS performance of Ag/GeTe/SiO_2/Si RRAM device and considered that the clockwise switching arose from a SET process due to a conductive filament connection between the electrodes and a subsequent RESET process due to a rupture of the filaments induced by Joule heating and/or dissolution, which could occur even with the current compliance. [224] Suresh et al. demonstrated Al/N-vinyl carbazole (PVK)/Al RRAM device with the unipolar Write Once Read Many times (WORM) characteristics. The pristine devices were in the low resistance ON state exhibiting ohmic behavior and at a voltage near 2 V, they switched abruptly to the high resistance OFF state showing space charge limited current (SCLC). Suresh et al. suggested that the rupturing of metallic filaments due to Joule heating may explain the effect. [225]. Therefore, the RESET process of the Ag/SP-GaO_x/SP-AlO_x/ITO RRAM devices was primarily influenced by the Joule-heating effect.

The conduction mechanism could be observed in **Fig. 3-9e**. The fitting results of regions with positive and negative bias indicated the device followed the ohmic conduction ($I \propto V$) in the low voltage region. Slopes of ~ 2.1 and ~ 4.1 represented the Child's square law and SCLC law in the high voltage region. [41, 140-144]

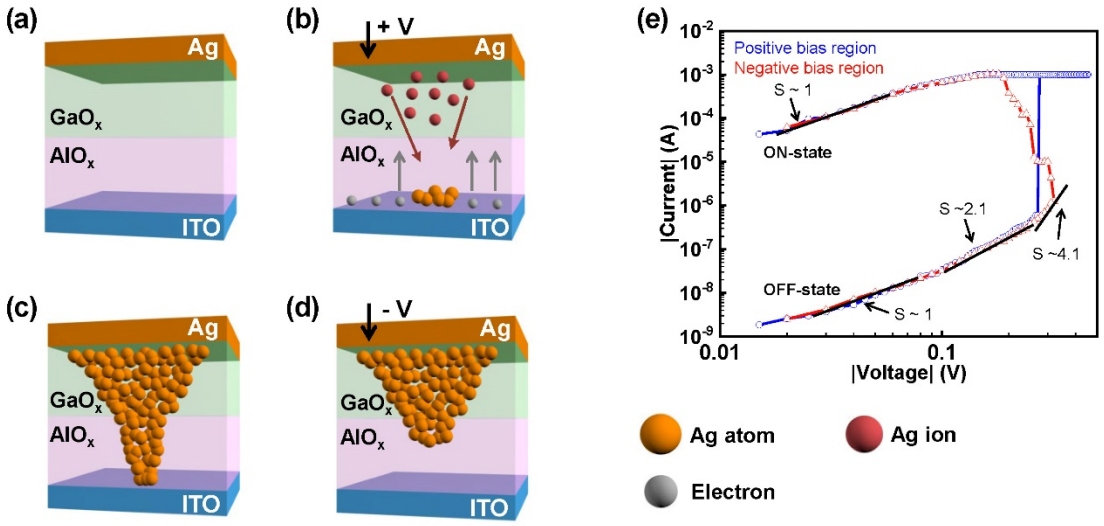

Figure 3-9. Switching mechanism of the Ag/SP-GaO_x/SP-AlO_x/ITO RRAM device with (a) initial OFF state, (b) redox reaction of Ag CF, (c) ON state after the SET operation, and (d) OFF state after the RESET operation. (e) Conduction mechanism with SCLC law of the Ag/SP-GaO_x/SP-AlO_x/ITORRAM device.

Although both Ag/SP-GaO_x/SP-AlO_x/ITO and Ag/SP-AlO_x/ITO RRAM devices worked based on the mechanism of metallic CF, the Ag/SP-GaO_x/SP-AlO_x/ITO RRAM device showed a stable ON/OFF ratio with a lower V_{SET} or V_{RESET}, which was associated with the rate of redox reaction and the ion mobility for different materials. In general, redox with a high reaction rate and ion mobility with a high rate always results in a high ion supply, which will make that the metallic CF formed from the inert electrode layer and the final shape of the formed CF will be an inverted cone. If the rates of redox reaction and ion mobility are low, a cone-shaped CF will be formed due to the ion nucleation. If the RRAM device works with a high rate of redox reaction and a low rate of ion mobility, the formation process of CF will occur in the dielectric layer and the accumulation of metal atoms will be observed in the cathode terminal, which can result in the anomalous and incompleted CF. Reversely, if the redox reaction with a low rate occurs in the RRAM device and the rate of ion mobility is high, because of

the insufficient supply of ions, CFs with shapes of branches will form from the inert electrode layer, and most redox reactions will occur near the edge of branched CFs. The lower operation voltages of the Ag/SP-GaO_x/ITO RRAM device indicated that the redox rate and ion mobility of the SP-GaO_x layer should be higher than the SP-AlO_x layer. Therefore, the Ag CF was easier to form in the Ag/SP-GaO_x/ITO RRAM device due to the higher redox rate and the faster velocity of the ion drift. Before the SET process, the Ag/SP-GaO_x/SP-AlO_x/ITO device was activated by a forming operation with a high voltage was applied and the device showed the LRS when the current was at $I_{CC.}$ The formed Ag CFs did not fully break during the following RESET operations and a part of Ag atoms might stay in the SP-GaO_x layer and act as the microscopic electrode, which conduced the subsequent formation process of Ag CF easier to realize with lower operation voltage. [185, 228-233] For the drift process of Ag^+ in the Ag/SP-GaO_x/SP-AlO_x/ITO RRAM device, before approaching BE ITO, Ag^+ needed to move through the SP-GaO_x layer and the SP-AlO_x layer. Due to the higher rates of redox reaction and ion mobility, a great deal of Ag^+ could easily drift through the SP-GaO_x layer with a lower voltage bias at first. Then partially of these Ag^+ could move into the SP-AlO_x layer due to the higher rates of redox reaction and ion mobility, and the reached BE ITO. Hence, Ag CFs in the Ag/SP-GaO_x/SP-AlO_x/ITO device formed with a lower operation voltage and presented in an inverted cone shape (**Fig. 3-9c**). [51, 64, 185, 228-233]

3.5 Conclusion

Successful improvement techniques were conducted onto the RRAM device with a single SP-AlO_x layer. The new device with the structure of Ni/SP-AlO_x/Pt was improved with the proposed structure of Ag/SP-GaO_x/SP-AlO_x/ITO, which demonstrated better electrical performance with lower operation voltage (< 0.6 V), larger ON/OFF ratio (> 2×10^4), longer retention time (> 2×10^4 s), more endurance cycles (> 200), and enhanced stability.

3.6 References

[7] C. Wan, P. Cai, M. Wang, Y. Qian, W. Huang, and X. Chen, "Artificial Sensory Memory," *Adv Mater,* vol. 32, no. 15, pp. e1902434(1-22), Apr 2020.

[8] H. Xu, L. Yin, C. Liu, X. Sheng, and N. Zhao, "Recent Advances in Biointegrated Optoelectronic Devices," *Adv Mater,* vol. 30, pp. e1800156(1-22), May 28 2018.

[10] Z. Shen, C. Zhao, Y. Qi, W. Xu, Y. Liu, I. Z. Mitrovic, L. Yang, and C. Zhao, "Advances of RRAM Devices: Resistive Switching Mechanisms, Materials and Bionic Synaptic Application," *Nanomaterials (Basel),* vol. 10, no. 8, pp. 1437(1-31), Jul 23 2020.

[32] P. Sun, L. Li, N. Lu, Y. Li, M. Wang, H. Xie, S. Liu, and M. Liu, "Physical model of dynamic Joule heating effect for reset process in conductive-bridge random access memory," *Journal of Computational Electronics,* vol. 13, no. 2, pp. 432-438, 2014.

[41] T. Guo, B. Sun, Y. Zhou, H. Zhao, M. Lei, and Y. Zhao, "Overwhelming coexistence of negative differential resistance effect and RRAM," *Phys Chem Chem Phys,* vol. 20, no. 31, pp. 20635-20640, Aug 8 2018.

[43] S. Long, Q. Liu, H. Lv, Y. Li, Y. Wang, S. Zhang, W. Lian, K. Zhang, M. Wang, H. Xie, and M. Liu, "Resistive switching mechanism of Ag/ZrO_2:Cu/Pt memory cell," *Applied Physics A,* vol. 102, no. 4, pp. 915-919, 2011.

[47] M. Kumar, S. Abbas, and J. Kim, "All-Oxide-Based Highly Transparent Photonic Synapse for Neuromorphic Computing," *ACS Appl Mater Interfaces,* vol. 10, no. 40, pp. 34370, Oct 10 2018.

[49] K. Lu, X. Li, Q. Sun, X. Pang, J. Chen, T. Minari, X. Liu, and Y. Song, "Solution-processed electronics for artificial synapses," *Materials Horizons,* vol.

8, no. 2, pp. 447-470, 2021.

[51] Z. Shen, C. Zhao, T. Zhao, W. Xu, Y. Liu, Y. Qi, I. Z. Mitrovic, L. Yang, and C. Z. Zhao, "Artificial Synaptic Performance with Learning Behavior for Memristor Fabricated with Stacked Solution-Processed Switching Layers," *ACS Applied Electronic Materials,* vol. 3, no. 3, pp. 1288-1300, 2021.

[61] H. S. P. Wong, H.-Y. Lee, S. Yu, Y.-S. Chen, Y. Wu, P.-S. Chen, B. Lee, F. T. Chen, and M.-J. Tsai, "Metal–Oxide RRAM," *Proceedings of the IEEE,* vol. 100, no. 6, pp. 1951-1970, 2012.

[62] X. Hong, D. J. Loy, P. A. Dananjaya, F. Tan, C. Ng, and W. Lew, "Oxide-based RRAM materials for neuromorphic computing," *Journal of Materials Science,* vol. 53, no. 12, pp. 8720-8746, 2018.

[63] V. Gupta, S. Kapur, S. Saurabh, and A. Grover, "Resistive Random Access Memory: A Review of Device Challenges," *IETE Technical Review,* vol. 37, no. 4, pp. 377-390, 2019.

[64] H. Wang and X. Yan, "Overview of Resistive Random Access Memory (RRAM): Materials, Filament Mechanisms, Performance Optimization, and Prospects," *physica status solidi (RRL) – Rapid Research Letters,* vol. 13, no. 9, pp. 1900073(1-12), 2019.

[79] S. Roy, G. Niu, Q. Wang, Y. Wang, Y. Zhang, H. Wu, S. Zhai, P. Shi, S. Song, Z. Song, Z. G. Ye, C. Wenger, T. Schroeder, Y. H. Xie, X. Meng, W. Luo, and W. Ren, "Toward a Reliable Synaptic Simulation Using Al-Doped HfO_2 RRAM," *ACS Appl Mater Interfaces,* vol. 12, no. 9, pp. 10648-10656, Mar 4 2020.

[80] D. Kumar, U. Chand, L. Wen Siang, and T.-Y. Tseng, "High-Performance $TiN/Al_2O_3/ZnO/Al_2O_3/TiN$ Flexible RRAM Device With High Bending Condition," *IEEE Transactions on Electron Devices,* vol. 67, no. 2, pp. 493-498, 2020.

[140] M. D. Debanjan Jana, Subhranu Samanta and Siddheswar Maikap, "RRAM characteristics using a new Cr/GdOx/TiN structure," *Nanoscale Research Letters,* vol. 9, pp. 680(1-9), 2014.

[141] F. Y. Yuan, N. Deng, C. C. Shih, Y. T. Tseng, T. C. Chang, K. C. Chang, M. H. Wang, W. C. Chen, H. X. Zheng, H. Wu, H. Qian, and S. M. Sze, "Conduction Mechanism and Improved Endurance in HfO_2-Based RRAM with Nitridation Treatment," *Nanoscale Res Lett,* vol. 12, no. 1, pp. 574(1-6), Oct 26 2017.

[142] A. N. Rodrigues, Y. P. Santos, C. L. Rodrigues, and M. A. Macêdo, "Al_2O_3 thin film multilayer structure for application in RRAM devices," *Solid-State Electronics,* vol. 149, pp. 1-5, 2018.

[143] T. S. Bhat, C. C. Revadekar, S. S. Patil, T. D. Dongale, D.-k. Kim, and P. S. Patil, "Photo-induced resistive switching in CdS-sensitized TiO_2 nanorod array memristive device," *Journal of Materials Science: Materials in Electronics,* vol. 31, no. 13, pp. 10919-10929, 2020.

[144] H.-D. Kim, M. J. Yun, and S. Kim, "Resistive switching characteristics of Al/Si_3N_4/p-Si MIS-based resistive switching memory devices," *Journal of the Korean Physical Society,* vol. 69, no. 3, pp. 435-438, 2016.

[149] Z. Hongbin, T. Hailing, W. Feng, and D. Jun, "Highly Transparent Dysprosium Oxide-Based RRAM With Multilayer Graphene Electrode for Low-Power Nonvolatile Memory Application," *IEEE Transactions on Electron Devices,* vol. 61, no. 5, pp. 1388-1393, 2014.

[150] M. Trapatseli, A. Khiat, S. Cortese, A. Serb, D. Carta, and T. Prodromakis, "Engineering the switching dynamics of TiO_x-based RRAM with Al doping," *Journal of Applied Physics,* vol. 120, no. 2, pp. 025108(1-9), 2016.

[151] K.-C. Chang, T.-J. Chu, J.-Y. Chen, Y.-T. Su, J.-P. Jiang, K.-H. Chen, H.-C. Huang, Y.-E. Syu, D.-S. Gan, S. M. Sze, C.-H. Pan, T.-C. Chang, T.-M. Tsai, R. Zhang, J.-C. Lou, T.-F. Young, J.-H. Chen, and C.-C. Shih, "Hopping effect of hydrogen-doped silicon oxide insert RRAM by supercritical CO_2 fluid treatment," *IEEE Electron Device Letters,* vol. 34, no. 5, pp. 617-619, 2013.

[152] F. Hussain, M. Imran, R. M. A. Khalil, M. A. Sattar, N. A. Niaz, A. M. Rana, M. Ismail, E. A. Khera, U. Rasheed, F. Mumtaz, T. Javed, and S. Kim, "A first-principles study of Cu and Al doping in ZrO_2 for RRAM device applications," *Vacuum,* vol. 168, pp. 108842(1-6), 2019.

[153] X. Huang, H. Wu, G. Bin, D. C. Sekar, L. Dai, M. Kellam, G. Bronner, N. Deng, and H. Qian, "HfO_2/Al_2O_3 multilayer for RRAM arrays: a technique to improve tail-bit retention," *Nanotechnology,* vol. 27, no. 39, pp. 395201(1-7), Sep 30 2016.

[154] Z. Fang, H. Y. Yu, X. Li, N. Singh, G. Q. Lo, and D. L. Kwong, "$HfO_x/TiO_x/HfO_x/TiO_x$ Multilayer-Based Forming-Free RRAM Devices With Excellent Uniformity," *IEEE Electron Device Letters,* vol. 32, no. 4, pp. 566-568, 2011.

[155] M.-C. Wu, J.-Y. Chen, Y.-H. Ting, C.-Y. Huang, and W.-W. Wu, "A novel high-performance and energy-efficient RRAM device with multi-functional conducting nanofilaments," *Nano Energy,* vol. 82, pp. 105717(1-10), 2021.

[156] S. Larentis, F. Nardi, S. Balatti, D. C. Gilmer, and D. Ielmini, "Resistive Switching by Voltage-Driven Ion Migration in Bipolar RRAM—Part II: Modeling," *IEEE Transactions on Electron Devices,* vol. 59, no. 9, pp. 2468-2475, 2012.

[157] D. Ielmini, F. Nardi, and C. Cagli, "Resistance-dependent amplitude of random telegraph-signal noise in resistive switching memories," *Applied Physics Letters,* vol. 96, no. 5, pp. 053503(1-4), 2010.

[158] L. Li, M. Chen, G. Huang, N. Yang, L. Zhang, H. Wang, Y. Liu, W. Wang, and J. Gao, "A green method to prepare Pd–Ag nanoparticles supported on reduced graphene oxide and their electrochemical catalysis of methanol and ethanol oxidation," *Journal of Power Sources,* vol. 263, pp. 13-21, 2014.

[159] N. M. Shiho Tokonam, Kanako Takasaki, and Naoki Toshima, "Novel Synthesis, Structure, and Oxidation Catalysis of Ag/Au Bimetallic Nanoparticles," *The Journal of Physical Chemistry C,* vol. 114, pp. 10336–10341, 2010.

[160] Y. Zhu, X. Xu, L. Zhang, J. Chen, and Y. Cao, "High efficiency inverted polymeric bulk-heterojunction solar cells with hydrophilic conjugated polymers as cathode interlayer on ITO," *Solar Energy Materials and Solar Cells,* vol. 97,

pp. 83-88, 2012.
[161] R.-H. Horng, D.-S. Wuu, Y.-C. Lien, and W.-H. Lan, "Low-resistance and high-transparency Ni/indium tin oxide ohmic contacts to p-type GaN," *Applied Physics Letters,* vol. 79, no. 18, pp. 2925-2927, 2001.
[162] C. S. M. Joseph George, "Electrical and optical properties of electron beam evaporated ITO thin films," *Surface and Coatings Technology,* vol. 132, pp. 45-48, 2000.
[163] H.-Y. L. H.-S. Philip Wong, Shimeng Yu, Yu-Sheng Chen, Yi Wu, Pang-Shiu Chen, Byoungil Lee, Frederick T. Chen, and Ming-Jinn Tsai, "Metal–Oxide RRAM," *PROCEEDINGS OF THE IEEE,* vol. 100, no. 6, pp. 1951-1970, 2012.
[164] Y. A. Asif Alia, Haider Abbasc, Yu-Rim Jeonc, Sajjad Hussaina, Bilal Abbas Naqvia, Changhwan Choic, Jongwan Junga, "Dependence of InGaZnO and SnO_2 thin film stacking sequence for the resistive switching characteristics of conductive bridge memory devices," *Applied Surface Science,* vol. 525, pp. 146390(1)-146390(8), 2020.
[165] S. Y. B. Gao, N. Xu, L.F. Liu, B. Sun, X.Y. Liu, R.Q. Han, J.F. Kang, B. Yu, Y.Y. Wang, "Oxide-Based RRAM Switching Mechanism: A New Ion-Transport-Recombination Model," presented at the 2008 IEEE International Electron Devices Meeting, San Francisco, CA, USA, 2008.
[166] J. H. Yoon, S. J. Song, I.-H. Yoo, J. Y. Seok, K. J. Yoon, D. E. Kwon, T. H. Park, and C. S. Hwang, "Highly Uniform, Electroforming-Free, and Self-Rectifying Resistive Memory in the Pt/Ta_2O_5/HfO_{2-x}/TiN Structure," *Advanced Functional Materials,* vol. 24, no. 32, pp. 5086-5095, 2014.
[167] K. J. Yoon, G. H. Kim, S. Yoo, W. Bae, J. H. Yoon, T. H. Park, D. E. Kwon, Y. J. Kwon, H. J. Kim, Y. M. Kim, and C. S. Hwang, "Double-Layer-Stacked One Diode-One Resistive Switching Memory Crossbar Array with an Extremely High Rectification Ratio of 10^9," *Advanced Electronic Materials,* vol. 3, no. 7, 2017.
[168] J. H. Yoon, D. E. Kwon, Y. Kim, Y. J. Kwon, K. J. Yoon, T. H. Park, X. L. Shao, and C. S. Hwang, "The current limit and self-rectification functionalities in the TiO_2/HfO_2 resistive switching material system," *Nanoscale,* vol. 9, no. 33, pp. 11920-11928, Aug 24 2017.
[169] S. Choi, S. Jang, J.-H. Moon, J. C. Kim, H. Y. Jeong, P. Jang, K.-J. Lee, and G. Wang, "A self-rectifying TaO_y/nanoporous TaO_x memristor synaptic array for learning and energy-efficient neuromorphic systems," *NPG Asia Materials,* vol. 10, no. 12, pp. 1097-1106, 2018.
[170] H. Jung, Y. H. Kim, J. Kim, T. S. Yoon, C. J. Kang, S. Yoon, and H. H. Lee, "Analog Memristive Characteristics of Mesoporous Silica-Titania Nanocomposite Device Concurrent with Selection Diode Property," *ACS Appl Mater Interfaces,* vol. 11, no. 40, pp. 36807-36816, Oct 9 2019.
[171] H. Tian, W. Mi, H. Zhao, M. A. Mohammad, Y. Yang, P. W. Chiu, and T. L. Ren, "A novel artificial synapse with dual modes using bilayer graphene as the bottom electrode," *Nanoscale,* vol. 9, no. 27, pp. 9275-9283, Jul 13 2017.
[172] Q. Cao, W. Lu, X. R. Wang, X. Guan, L. Wang, S. Yan, T. Wu, and X. Wang,

"Nonvolatile Multistates Memories for High-Density Data Storage," *ACS Appl Mater Interfaces,* vol. 12, no. 38, pp. 42449-42471, Sep 23 2020.

[173] F. Lopez-Herrera y Cairo, H. D. Jimenez-Torres, I. D. Barcelo-Quintal, P. F. Zarate-Del Valle, G. G. Carbajal-Arizaga, W. de la Cruz-Hernandez, and S. Gomez-Salazar, "Heavy metals on sediments of a Mexican tropical lake: chemical speciation, metal uptake capacity, and chemical states," *International Journal of Environmental Science and Technology,* vol. 16, no. 12, pp. 8423-8436, 2019.

[174] C. V. Ramana, E. J. Rubio, C. D. Barraza, A. Miranda Gallardo, S. McPeak, S. Kotru, and J. T. Grant, "Chemical bonding, optical constants, and electrical resistivity of sputter-deposited gallium oxide thin films," *Journal of Applied Physics,* vol. 115, no. 4, pp. 043508(1-10), 2014.

[175] C. L. B. R. Carli, "XPS analysis of gallium oxides," *Applied Surface Science* vol. 74, pp. 99-102, 1994.

[176] H. T. Nguyen, H. Lu, E. Kobayashi, T. Ishikawa, and M. Komiyama, "Raney-Nickel Catalyst Deactivation in Supercritical Water Gasification of Ethanol Fermentation Stillage and its Mitigation," *Topics in Catalysis,* vol. 57, no. 10-13, pp. 1078-1084, 2014.

[177] M.-H. T. Meng-Fan Luo, Chao-Chian Wang, Won-Ru Lin, Chiun-Yu Ho, Bo-We Chang, Cheng-Tin Wang, Yin-Chang Lin, and Yao-Jane Hsu, "Temperature-Dependent Oxidation of Pt Nanoclusters on a Thin Film of Al_2O_3 on NiAl(100)," *The Journal of Physical Chemistry C,* vol. 113, pp. 12419–12426, 2009.

[178] Z. Wang, W. G. Zhu, A. Y. Du, L. Wu, Z. Fang, X. A. Tran, W. J. Liu, K. L. Zhang, and H. Y. Yu, "Highly Uniform, Self-Compliance, and Forming-Free ALD HfO_2-Based RRAMWith Ge Doping," *IEEE Transactions on Electron Devices,* vol. 59, no. 4, pp. 1203-1208, 2012.

[179] N. Raghavan, A. Fantini, R. Degraeve, P. J. Roussel, L. Goux, B. Govoreanu, D. J. Wouters, G. Groeseneken, and M. Jurczak, "Statistical insight into controlled forming and forming free stacks for HfO_x RRAM," *Microelectronic Engineering,* vol. 109, pp. 177-181, 2013.

[180] Y.-F. Chang, T.-C. Chang, and C.-Y. Chang, "Investigation statistics of bipolar multilevel memristive mechanism and characterizations in a thin FeO_x transition layer of TiN/SiO_2/FeO_x/Fe structure," *Journal of Applied Physics,* vol. 110, no. 5, pp. 053703-1-053703-7, 2011.

[181] Y.-F. Chang, L. Ji, Y. Wang, P.-Y. Chen, F. Zhou, F. Xue, B. Fowler, E. T. Yu, and J. C. Lee, "Investigation of edge- and bulk-related resistive switching behaviors and backward-scan effects in SiO_x-based resistive switching memory," *Applied Physics Letters,* vol. 103, no. 19, pp. 193508-1-193508-5, 2013.

[182] Y.-C. Chen, H.-C. Huang, C.-Y. Lin, S. Kim, Y.-F. Chang, and J. C. Lee, "Effects of Ambient Sensing on SiO_x-Based Resistive Switching and Resilience Modulation by Stacking Engineering," *ECS Journal of Solid State Science and Technology,* vol. 7, no. 8, pp. P350-P354, 2018.

[183] X. Huang, R. Fang, C. Yang, K. Fu, H. Fu, H. Chen, T. H. Yang, J. Zhou, J. Montes, M. Kozicki, H. Barnaby, B. Zhang, and Y. Zhao, "Steep-slope field-effect transistors with AlGaN/GaN HEMT and oxide-based threshold switching device," *Nanotechnology,* vol. 30, no. 21, pp. 215201-1-215201-17, May 24 2019.

[184] F. Zhou, Y. F. Chang, Y. C. Chen, X. Wu, Y. Zhang, B. Fowler, and J. C. Lee, "A study of the interfacial resistive switching mechanism by proton exchange reactions on the SiO_x layer," *Phys Chem Chem Phys,* vol. 18, no. 2, pp. 700-703, Jan 14 2016.

[185] K. Bejtka, G. Milano, C. Ricciardi, C. F. Pirri, and S. Porro, "TEM Nanostructural Investigation of Ag-Conductive Filaments in Polycrystalline ZnO-Based Resistive Switching Devices," *ACS Appl Mater Interfaces,* vol. 12, no. 26, pp. 29451-29460, Jul 1 2020.

[186] L. L. Andrea Padovani, Member, Onofrio Pirrotta, Luca Vandelli, and Gennadi Bersuker, "Microscopic Modeling of HfO_x RRAM Operations: From Forming to Switching," *IEEE TRANSACTIONS ON ELECTRON DEVICES,* vol. 62, no. 6, pp. 1998-2006, 2015.

[187] D. C. G. G. Bersuker, D. Veksler, J. Yum, H. Park, S. Lian, L. Vandelli, A. Padovani, L. Larcher, K. McKenna, A. Shluger, V. Iglesias, M. Porti, M. Nafría, W. Taylor, P. D. Kirsch, R. Jammy, "Metal Oxide RRAM Switching Mechanism Based on Conductive Filament Microscopic Properties," presented at the 2010 International Electron Devices Meeting, San Francisco, CA, USA, 2010.

[188] H. Y. Li, X. D. Huang, J. H. Yuan, Y. F. Lu, T. Q. Wan, Y. Li, K. H. Xue, Y. H. He, M. Xu, H. Tong, and X. S. Miao, "Controlled Memory and Threshold Switching Behaviors in a Heterogeneous Memristor for Neuromorphic Computing," *Advanced Electronic Materials,* vol. 6, no. 8, pp. 2000309-1-2000309-11, 2020.

[189] S. Asapu and T. Maiti, "Electrothermal numerical modeling of multifilamentary conduction in Ta_2O_{5-x}/WO_{3-x} bilayer oxides based RRAM," *Ferroelectrics,* vol. 500, no. 1, pp. 229-240, 2016.

[190] S. Kim, T.-H. Kim, H. Kim, and B.-G. Park, "Current suppressed self-compliance characteristics of oxygen rich TiO_y inserted Al_2O_3/TiO_x based RRAM," *Applied Physics Letters,* vol. 117, no. 20, pp. 202106-202112, 2020.

[191] N. Sedghi, H. Li, I. F. Brunell, K. Dawson, R. J. Potter, Y. Guo, J. T. Gibbon, V. R. Dhanak, W. D. Zhang, J. F. Zhang, J. Robertson, S. Hall, and P. R. Chalker, "The role of nitrogen doping in ALD Ta_2O_5 and its influence on multilevel cell switching in RRAM," *Applied Physics Letters,* vol. 110, no. 10, pp. 102902-102907, 2017.

[192] D. K. Lee, M.-H. Kim, S. Bang, T.-H. Kim, Y.-J. Choi, K. Hong, S. Kim, S. Cho, J.-H. Lee, and B.-G. Park, "Improvement of Resistive Switching Characteristics of Titanium Oxide Based Nanowedge RRAM Through Nickel Silicidation," *IEEE Transactions on Electron Devices,* pp. 1-5, 2020.

[193] L. Hu, W. Han, and H. Wang, "Resistive switching and synaptic learning performance of a TiO_2 thin film based device prepared by sol-gel and spin

coating techniques," *Nanotechnology,* vol. 31, no. 15, pp. 155202-155222, Apr 10 2020.

[194] Z.-G. Long, C.-P. Zheng, and J.-C. Li, "Enhanced resistive switching performance in rare-earth/high-κ CeO_2/ZrO_2 nanocomposite films," *Physics Letters A,* vol. 386, pp. 126995-127001, 2021.

[195] C. J. Park, S. W. Han, and M. W. Shin, "Laser-Assisted Interface Engineering for Functional Interfacial Layer of Al/ZnO/Al Resistive Random Access Memory (RRAM)," *ACS Appl Mater Interfaces,* vol. 12, no. 28, pp. 32131-32142, Jul 15 2020.

[196] C. Sun, S. M. Lu, F. Jin, W. Q. Mo, J. L. Song, and K. F. Dong, "Multi-factors induced evolution of resistive switching properties for TiN/Gd_2O_3/Au RRAM devices," *Journal of Alloys and Compounds,* vol. 816, pp. 152564-152571, 2020.

[197] M. Ismail, Z. Batool, K. Mahmood, A. Manzoor Rana, B.-D. Yang, and S. Kim, "Resistive switching characteristics and mechanism of bilayer HfO_2/ZrO_2 structure deposited by radio-frequency sputtering for nonvolatile memory," *Results in Physics,* vol. 18, pp. 103275-103282, 2020.

[198] T. Liu, W. Wu, K. N. Liao, Q. Sun, X. Gong, V. A. L. Roy, Z. Z. Yu, and R. K. Y. Li, "Fabrication of carboxymethyl cellulose and graphene oxide bio-nanocomposites for flexible nonvolatile resistive switching memory devices," *Carbohydr Polym,* vol. 214, pp. 213-220, Jun 15 2019.

[199] C.-C. Hsu, J.-K. Sun, C.-C. Tsao, and P.-Y. Chuang, "Effects of Gibbs free energy of interfacial metal oxide on resistive switching characteristics of solution-processed HfO_x films," *Physica B: Condensed Matter,* vol. 519, pp. 21-25, 2017.

[200] S. Kim, B. Choi, M. Lim, Y. Kim, H. D. Kim, and S. J. Choi, "Synaptic Device Network Architecture with Feature Extraction for Unsupervised Image Classification," *Small,* vol. 14, no. 32, pp. e1800521(1-9), Aug 2018.

[201] X. Yi, Z. Yu, X. Niu, J. Shang, G. Mao, T. Yin, H. Yang, W. Xue, P. Dhanapal, S. Qu, G. Liu, and R.-W. Li, "Intrinsically Stretchable Resistive Switching Memory Enabled by Combining a Liquid Metal-Based Soft Electrode and a Metal-Organic Framework Insulator," *Advanced Electronic Materials,* vol. 5, no. 2, 2019.

[202] S. J. Kim, S. Yoon, and H. J. Kim, "Review of solution-processed oxide thin-film transistors," *Japanese Journal of Applied Physics,* vol. 53, no. 2S, pp. 02ba02-02ba12, 2014.

[203] A. Bid, A. Bora, and A. K. Raychaudhuri, "Temperature dependence of the resistance of metallic nanowires of diameter⩾15nm: Applicability of Bloch-Grüneisen theorem," *Physical Review B,* vol. 74, no. 3, pp. 035426(1-8), 2006.

[204] X. Yan, C. Qin, C. Lu, J. Zhao, R. Zhao, D. Ren, Z. Zhou, H. Wang, J. Wang, L. Zhang, X. Li, Y. Pei, G. Wang, Q. Zhao, K. Wang, Z. Xiao, and H. Li, "Robust Ag/ZrO_2/WS_2/Pt Memristor for Neuromorphic Computing," *ACS Appl Mater Interfaces,* vol. 11, no. 51, pp. 48029-48038, Dec 26 2019.

[205] Y. C. Chen, C. C. Lin, S. T. Hu, C. Y. Lin, B. Fowler, and J. Lee, "A Novel Resistive Switching Identification Method through Relaxation Characteristics

for Sneak-path-constrained Selectorless RRAM application," *Sci Rep,* vol. 9, no. 1, pp. 12420-12425, Aug 27 2019.

[206] Y. L. Xiao Di Huang, Hao Yang Li, Yi Fan Lu, Kan Hao Xue , and Xiang Shui Miao, "Enhancement of DC/AC resistive switching performance in AlO_x memristor by twotechnique bilayer approach," *Appl. Phys. Lett.,* vol. 116, pp. 173504-1-173504-6, 2020.

[207] R. A. D. Kumar, U. Chand, T.Y. Tseng, "Metal oxide resistive switchung memory: Materials, properties and switching mechanisms," *Ceramics International,* vol. 05, no. 289, pp. 1-10, 2017.

[208] S. M. S. Roy, G. Sreekanth, M. Dutta, D. Jana, Y.Y. Chen, J.R. Yang, "Improved resistive switching phenomena and mechanism using Cu-Al alloy in a new Cu: AlO_x/TaO_x/TiN structure," *Journal of Alloys and Compounds,* vol. 637, pp. 517-523, 2015.

[209] S. Y. Yi Wu, Byoungil Lee, and Philip Wong, "Low-power TiN/Al_2O_3/Pt resistive switching device with sub-20 μA switching current and gradual resistance modulation," *Journal of Applied Physics,* vol. 110, pp. 094104-1-094104-6, 2011.

[210] H. W. Ye Zhang, Minghao Wu, Ning Deng, Zhiping Yu, Jinyu Zhang, and He Qian, "Random telegraph noise analysis in AlO_x/WO_y resistive switching memories," *Applied Physics Letters,* vol. 104, pp. 103507-1-103507-5, 2014.

[211] S. K. Vishwanath, H. Woo, and S. Jeon, "Enhancement of resistive switching properties in Al_2O_3 bilayer-based atomic switches: multilevel resistive switching," *Nanotechnology,* vol. 29, no. 23, pp. 235202-1-235202-8, Jun 8 2018.

[212] A. B. Nikolaus Knorr, Zoi Karipidou, René Wirtz, Mustafa Sarpasan, Silvia Rosselli, and Gabriele Nelles, "Evidence of electrochemical resistive switching in the hydrated alumina layers of Cu/CuTCNQ/(native AlO_x)/Al junctions," *Journal of Applied Physics,* vol. 114, pp. 124510-1-124510-9, 2013.

[213] I. C. C. Chi Cun Kuo, Chih Cheng Shih, Kuan Chang Chang, Chao Hsien Huang, Po Hsun Chen, Ting Chang Chang, Tsung Ming Tsai, Jing Shuen Chang, Jacob Chih-Ching Huang, "Galvanic Effect of Au-Ag Electrodes for Conductive Bridging Resistive Switching Memory," *IEEE Electron Device Letters,* vol. 36, no. 12, pp. 1321-1324, 2015.

[214] Z. S. Yanfei Qi, Chun Zhao, Ce Zhou Zhao, "Effect of electrode area on resistive switching behavior in translucent solution-processed AlO_x based memory device," *Journal of Alloys and Compounds,* vol. 822, pp. 153603-1-153603-10, 2019.

[215] A. Ranjan, N. Raghavan, S. J. O'Shea, S. Mei, M. Bosman, K. Shubhakar, and K. L. Pey, "Conductive Atomic Force Microscope Study of Bipolar and Threshold Resistive Switching in 2D Hexagonal Boron Nitride Films," *Sci Rep,* vol. 8, no. 1, pp. 2854-2862, Feb 12 2018.

[216] P. W. S. A. Sleiman, and M. F. Mabrook, "Mechanism of resistive switching in Cu/AlO_x/W nonvolatile memory structures," *J. Appl. Phys.,* vol. 113, pp. 164506-1-164506-6, 2013.

[217] Z. D. YANG ZHANG, RUI LI, CHIEH-JEN KU, PAVEL REYES, ALMAMUN ASHRAFI, and YICHENG LU, "FeZnO-Based Resistive Switching Devices," *Journal of ELECTRONIC MATERIALS,* vol. 41, no. 10, pp. 2880-2885, 2012.

[218] R. W. Xiaolong ZHAO, Xiangheng XIAO, Congyan LU, Facai WU, Rongrong CAO, Changzhong JIANG & Qi LIU, "Flexible cation-based threshold selector for resistive switching memory integration," *SCIENCE CHINA,* vol. 61, pp. 060413:1–060413:8, 2018.

[219] C. Ye, J. Wu, G. He, J. Zhang, T. Deng, P. He, and H. Wang, "Physical Mechanism and Performance Factors of Metal Oxide Based Resistive Switching Memory: A Review," *Journal of Materials Science & Technology,* vol. 32, no. 1, pp. 1-11, 2016.

[220] K. Patel, J. Cottom, M. Bosman, A. J. Kenyon, and A. L. Shluger, "An oxygen vacancy mediated Ag reduction and nucleation mechanism in SiO_2 RRAM devices," *Microelectronics Reliability,* vol. 98, pp. 144-152, 2019.

[221] C.-F. Chang, J.-Y. Chen, G.-M. Huang, T.-Y. Lin, K.-L. Tai, C.-Y. Huang, P.-H. Yeh, and W.-W. Wu, "Revealing conducting filament evolution in low power and high reliability Fe_3O_4/Ta_2O_5 bilayer RRAM," *Nano Energy,* vol. 53, pp. 871-879, 2018.

[222] H. Abbas, A. Ali, J. Jung, Q. Hu, M. R. Park, H. H. Lee, T.-S. Yoon, and C. J. Kang, "Reversible transition of volatile to non-volatile resistive switching and compliance current-dependent multistate switching in IGZO/MnO RRAM devices," *Applied Physics Letters,* vol. 114, no. 9, pp. 093503(1-6), 2019.

[223] F. Echouchene and E. Jemii, "Analysis of the transient Joule heating effect in a conductive-bridge random-access memory (CBRAM) using a single-phase-lag (SPL) model," *Journal of Computational Electronics,* vol. 20, no. 3, pp. 1422-1429, 2021.

[224] Y. Imanishi, S. Kida, and T. Nakaoka, "Direct observation of Ag filament growth and unconventional SET-RESET operation in GeTe amorphous films," *AIP Advances,* vol. 6, no. 7, pp. 075003-1-075003-9, 2016.

[225] A. Suresh, G. Krishnakumar, and M. A. Namboothiry, "Filament theory based WORM memory devices using aluminum/poly(9-vinylcarbazole)/aluminum structures," *Phys Chem Chem Phys,* vol. 16, no. 26, pp. 13074-13077, Jul 14 2014.

[226] J. Hu, H. M. Branz, R. S. Crandall, S. Ward, and Q. Wang, "Switching and filament formation in hot-wire CVD p-type a-Si:H devices," *Thin Solid Films,* vol. 430, no. 1-2, pp. 249-252, 2003.

[227] H.-L. Ma, Z.-Q. Wang, H.-Y. Xu, L. Zhang, X.-N. Zhao, M.-S. Han, J.-G. Ma, and Y.-C. Liu, "Coexistence of unipolar and bipolar modes in Ag/ZnO/Pt resistive switching memory with oxygen-vacancy and metal-Ag filaments," *Chinese Physics B,* vol. 25, no. 12, pp. 127303-1-127303-7, 2016.

[228] X. Zhang, S. Liu, X. Zhao, F. Wu, Q. Wu, W. Wang, R. Cao, Y. Fang, H. Lv, S. Long, Q. Liu, and M. Liu, "Emulating Short-Term and Long-Term Plasticity of Bio-Synapse Based on Cu/a-Si/Pt Memristor," *IEEE Electron Device Letters,* vol. 38, no. 9, pp. 1208-1211, 2017.

[229] A. Ali, Y. Abbas, H. Abbas, Y.-R. Jeon, S. Hussain, B. A. Naqvi, C. Choi, and J. Jung, "Dependence of InGaZnO and SnO_2 thin film stacking sequence for the resistive switching characteristics of conductive bridge memory devices," *Applied Surface Science,* vol. 525, pp. 146390(1-8), 2020.

[230] J. Zhang, F. Wang, C. Li, X. Shan, A. Liang, K. Hu, Y. Li, Q. Liu, Y. Hao, and K. Zhang, "Insight into interface behavior and microscopic switching mechanism for flexible HfO_2 RRAM," *Applied Surface Science,* vol. 526, pp. 146723(1-7), 2020.

[231] S. Y. B. Gao, N. Xu, L.F. Liu, B. Sun, X.Y. Liu, R.Q. Han, J.F. Kang, B. Yu, Y.Y. Wang, "Oxide-Based RRAM Switching Mechanism: A New Ion-Transport-Recombination Model," presented at the 2008 IEEE International Electron Devices Meeting, San Francisco, CA, USA, 2008.

[232] A. Padovani, L. Larcher, O. Pirrotta, L. Vandelli, and G. Bersuker, "Microscopic Modeling of HfO_x RRAM Operations: From Forming to Switching," *IEEE Transactions on Electron Devices,* vol. 62, no. 6, pp. 1998-2006, 2015.

[233] D. C. G. G. Bersuker, D. Veksler, J. Yum, H. Park, S. Lian, L. Vandelli1, A. Padovani, L. Larcher1, K. McKenna, A. Shluger, V. Iglesias, M. Porti, M. Nafría, W. Taylor, P. D. Kirsch, R. Jammy, "Metal Oxide RRAM Switching Mechanism Based on Conductive Filament Microscopic Properties," presented at the 2010 International Electron Devices Meeting, San Francisco, CA, USA, 2010.

Chapter 4: Artificial synaptic performance for RRAM devices with stacked solution-processed GaO_x/AlO_x dielectric

Superior electrical characteristics such as low energy consumption, high data storage density, fast operation speed, and excellent scalability of the RRAM device have made it receive extensive attention from the field of artificial intelligence (AI) and neuromorphic network. [5-8, 234, 235] Artificial synaptic characteristics of two-terminal devices represented by RRAM are considered to be one of the most effective techniques to solve the current hardware dilemma of AI area induced by Moore's law, memory limitation, and high energy consumption. [16, 46, 62, 63] The final goal of AI research is to make digital computers operate like the human brain, emulating bionic abilities like massive parallelism, self-learning behavior, self-cognition progress, and self-adaptation operation. [7, 62, 63] As illustrated in **Fig. 4-1a**, biologically, the human brain controls the brain-inspired behaviors based on hundreds of millions of neurons (~10^{11}) with the connection form of the synapses (~10^{15}). The significance of exploring artificial synapses is to enable electronic devices to exhibit the characteristics of biological synapses. Many researchers have provided evidence to support that RRAM devices could demonstrate artificial synaptic behaviors. [7, 16, 46, 62, 63]

The priority of artificial synaptic behaviors for an RRAM device is excellent electrical performance, which is always presented with multi-level states of current and conductance at first. Hence, in this chapter, the multi-level states of I-V characteristics for the Ag/SP-GaO_x/SP-AlO_x/ITO RRAM device were confirmed with different

electrical characterization methods. Then some essential artificial synaptic characteristics, such as excitatory postsynaptic current (EPSC), paired-pulse facilitation (PPF), long-term potentiation (LTP), long-term depression (LTD), and spiking-timing-dependent plasticity (STDP) were evaluated with various external pulse stimuli to present artificial short-term memory (STM) and long-term memory (LTM) of the Ag/SP-GaO_x/SP-AlO_x/ITO RRAM device. Finally, based on vital parameters of the artificial synaptic behaviors, handwriting Arabic numbers (0 ~ 9) were recognized by an artificial neuron network system (ANN) with the data set from Mixed National Institute of Standards and Technology (MNIST). After 3000 times training processes, the highest accuracy of the pattern recognition was up to 96%. [50, 51]

4.1 Biological and biomimetic foundation of neuron synapses

The primary purpose of exploration in biomimetic synaptic devices is to emulate the synaptic function of biological synapses. Therefore, it is necessary to provide a detailed discussion on the connection between biological synapses and biomimetic synaptic devices in this section.

4.1.1 Biological synapse

In the biological neuron system, two main transmission modalities, electrical and chemical, of synapses have been considered to provide the physiological basis to neural activities, which derived the electrical synapse (**Fig. 4-1c**) and the chemical synapse

(**Fig. 4-1d**). [8, 50, 200, 236-239] For the electrical synapse, the transmission of nerve signals is realized in the form of electrical transmission and the transmission channel is a low-resistance gap junction between pre-and post-synaptic membranes. [8, 236-239] Electrical synapses are mainly found in the nervous tissues of invertebrates and lower vertebrates. [8, 236-239] Compared with the electrical synapse, the chemical synapse relies on the terminal of the presynaptic neuron to release special chemicals (neurotransmitters) as media for transmitting information to affect the postsynaptic neuron, which is closely related to the high-level neural activities, such as memorizing and learning. [236-239] In this thesis, the research on artificial synaptic behaviors of the Ag/SP-GaO_x/SP-AlO_x/ITO RRAM device was based on the chemical synapse as the theoretical foundation. The transmission of information in the human brain is based on a neural network composed of neurons. During the transmission process, external stimulus signals are transmitted to the axons of neurons. A neuron has only one axon, and the tip of an axon produces multiple branches. The tip of each branch is enlarged into the shape of a cup or ball, which is called a synaptosome. Synaptosomes are in contact with the cyton or dendrites of multiple neurons to form synapses. The structure of a biological synapse could be observed in **Fig. 4-1d**, which mainly included a presynaptic membrane, a synaptic cleft, and a postsynaptic membrane. The stimuli signal from the neuron is transmitted from the axon to the synaptosome and the potential of the synaptosome changes due to the flow of calcium ions (Ca^{2+}), which promotes the synaptic vesicles in the synaptosome to release neurotransmitters into the synaptic cleft. Then The combination of neurotransmitter and postsynaptic membrane results in the

potential change of the postsynaptic membrane, which produces the local postsynaptic current (PSC) and completes the information transmission. [46]

4.1.2 Biomimetic synaptic behaviors of the synaptic device

At present, most of the research on biomimetic synaptic devices focuses on the imitation of chemical synapses. The function variation of the biological chemical synapse is determined by the synaptic weight, which is the fundamental presence of neural connection strength. [7, 51, 62] For the biomimetic synaptic device, this synaptic weight can be obtained with the forms of specific resistance or conductance and the change of this synaptic weight indicates the synaptic plasticity. [7, 10, 235, 239] When the external spiking was applied upon to the synaptic device, the biomimetic synaptic performance is always evaluated by the change of the PSC, which may be inhibitory or excitatory. [7, 10, 235, 239] With various modulation techniques of the PSC, different essential characteristics of synaptic plasticity can be obtained, including classic short-term plasticity, long-term plasticity, and STDP. [7, 10, 235, 239] Biological synaptic plasticity is responsible for neural activities like memorizing, learning, recognition, and logical thinking. Therefore, it is significant to investigate the synaptic plasticity of biomimetic synaptic devices. [7, 10, 235, 239]

Short-term plasticity and long-term plasticity have been accepted as the typical response to external stimuli. In general, short-term plasticity is always reflected by PPF. [10, 237, 238] PPF is demonstrated by the response of the synaptic device to two consecutive

external stimuli. After the first stimuli A_1, the synaptic device may exhibit an increased current to respond to the second stimuli A_2, which results in PPF. [7, 10, 236] The PPF index is always determined by the current ratio of EPSC. The relationship between the PPF index and the time interval (Δt) of two consecutive stimuli is always used to evaluate STP. With the increment of Δt, the PPF always decays follow the equation 4-1 (**Eq. 4-1**): [7, 10, 236]

$$\mathrm{PPF} = C_1 \cdot \exp\left(-\frac{\Delta t}{\tau_1}\right) + C_2 \cdot \exp\left(-\frac{\Delta t}{\tau_2}\right) \quad \textbf{(Eq. 4-1)}$$

where τ_1 and τ_2 are the relaxation time of the rapid and slow stages for the PPF decay, respectively. The magnitudes of initial facilitation for rapid (slow) phases are represented by C_1 (C_2). Generally, as one successful stimuli process, τ_2 should be an order of magnitude larger than τ_1. [10] The short-term plasticity is associated with the short-term response and recognition of external information, which can transit to The long-term plasticity after repeated rehearsal and training processes. [10] Based on the fundamental behaviors of short-term plasticity, long-term plasticity is related to long-term learning and memorizing. The long-term plasticity could be considered as the accumulation of more consecutive external stimuli, which was transferred from the short-term plasticity. Due to the repeated operations of short-term plasticity, the long-term plasticity and the long-term memory behavior of the synapses could be obtained. Current research on long-term plasticity mainly focuses on LTP, LTD, and the transition from STM to LTM. For a single artificial synaptic device, compared with the

PPF characteristic generated by two consecutive pulses, the performance of LTP and LTD are always triggered by a series of pulses and the pulse number is usually over 100. In addition, the duration time of PPF measurement is always lower than 1 s while the testing time of LTP and LTD is generally longer than 2 s. For an array or a matrix comprising of many artificial synaptic devices, with modulation techniques based on various properties of input pulses, STM, LTM, and transition from STM to LTM can be obtained. [10, 62] All these properties of synaptic plasticity are presented by electrical synaptic performance.

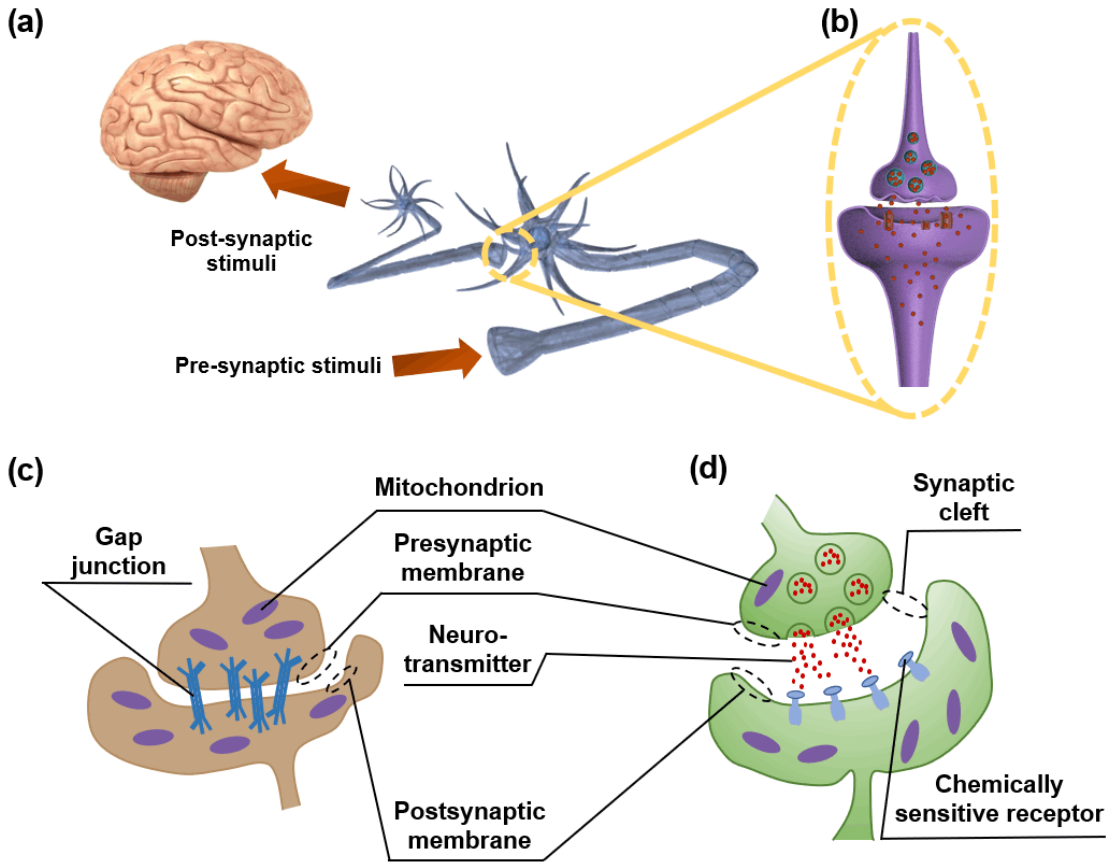

Figure 4-1. Schematic views of (a) neuron activities in the human brain and (b) 3D structure of a biological synapse. Cross-sectional structures of (c) the electrical synapse and (d) the chemical synapse.

4.2 Multi-level states of the I-V characteristic for the Ag/SP-GaO_x/SP-AlO_x/ITO RRAM device

Fig. 4-2 demonstrated I-V curves of the Ag/SP-GaO_x/SP-AlO_x/ITO RRAM device with multiple states. Two different testing operations were utilized in **Figs. 4-2a** and **4-2b**, respectively. In **Fig. 4-2a**, each operation cycle included one SET operation and one RESET operation. For the first cycles, after the SET operation (SET-1), the Ag/SP-GaO_x/SP-AlO_x/ITO RRAM device was at LRS with I_{CC} at 200 μA. Then the subsequent RESET operation (RESET-1) was conducted to make the device switch back to HRS. SET-2 and SET-3 were realized with I_{CC} at 1 mA and 5 mA, respectively. The final SET-4 showed an I_{CC} of 10 mA when the device was at LRS, which indicated that the Ag/SP-GaO_x/SP-AlO_x/ITO RRAM device could demonstrate multi-level current and conductance states with the external voltage stimuli. In **Fig. 4-2b**, another testing method was used. Three consecutive SET operations (1^{st}, 2^{nd}, and 3^{rd}) with increasing I_{CC} were conducted at first and the device showed LRS at three different I_{CC}s. Then six continuous RESET operations were performed with gradually increasing stop voltages (0.1 to 0.8 V), which made the device transfer to HRS and indicated more states of current and conductance.

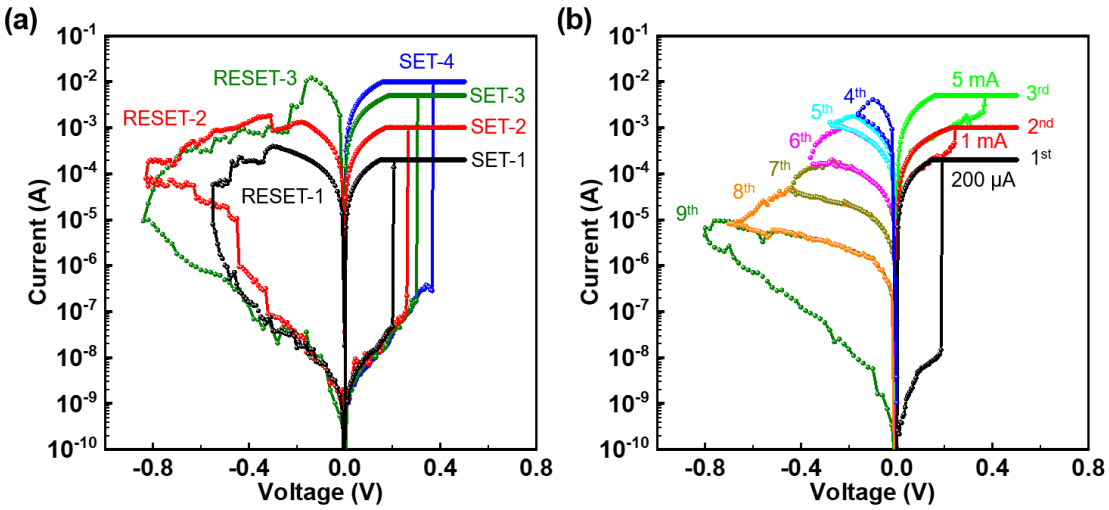

Figure 4-2. Multi-level states of I-V characteristics for the Ag/SP-GaO_x/SP-AlO_x/ITO RRAM device with different measurement operations.

4.3 Artificial synaptic behaviors of the Ag/SP-GaO_x/SP-AlO_x/ITO RRAM device

The multi-level states of current and conductance indicated the great potential of artificial synaptic performance. [10, 51] Pulse-response measurement of EPSC and PFF supported this speculation, which was presented in **Figs. 4-3a** and **4-3b**, respectively. In **Fig. 4-3a**, one single pulse with the amplitude (P_A) of 0.8 V and the pulse width (P_W) of 50 ms was applied onto TE Ag. An obvious increase of response current was observed with the stimuli from the electrical pulse and the current decayed to the initial state, which emulated the biological EPSC behavior [240-242] In **Fig. 4-3b**, two consecutive electrical pulses were applied onto TE Ag with the same P_A and P_W. Each pulse triggered corresponding EPSC behaviors, which have been labeled with blue and red curves, respectively. A higher current was obtained in the second stimuli process, which emulated the biological PPF characteristic. [243-245] After the second pulse, the current decayed again, and the final current amplitude was higher than the amplitude of

the initial current, which emulated the artificial STM behavior.

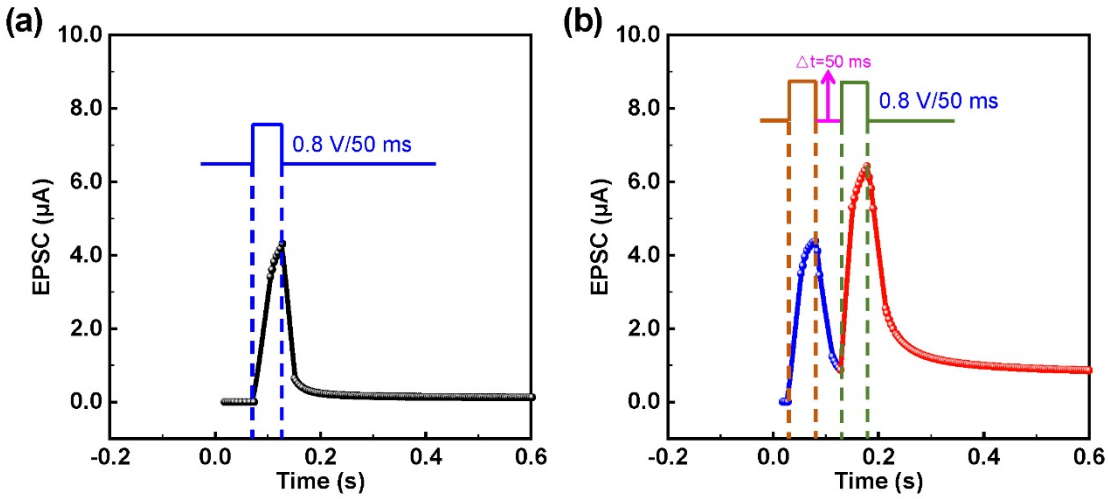

Figure 4-3. Artificial synaptic behavior of the Ag/SP-GaO_x/SP-AlO_x/ITO RRAM device with (a) EPSC and (b) PPF characteristics.

The performance of PPF for an RRAM device could be evaluated by PPF index, which followed the equation 4-2 (**Eq. 4-2**):

$$\text{PPF Index} = (I_1 - I_2) / I_1 \times 100\% \qquad \textbf{(Eq. 4-2)}$$

where I_1 was the peak current of the EPSC triggered by the first pulse, and I_2 was the peak current of the EPSC triggered by the second pulse. According to the expression in **Eq. 4-1**, the change of PPF was influenced by the time interval between two consecutive pulses. Hence, the relationship between the PPF index and the pulse time interval could be observed in **Fig. 4-4a**. In addition, the artificial synaptic response of the Ag/SP-GaO_x/SP-AlO_x/ITO RRAM device to external pulses with different P_W was assessed, as illustrated in **Fig. 4-4b**. The EPSC peak values increased with the

increment of P_W, which indicated that the synaptic behavior of the Ag/SP-GaO_x/SP-AlO_x/ITO RRAM device could be modulated by controlling input pulses.

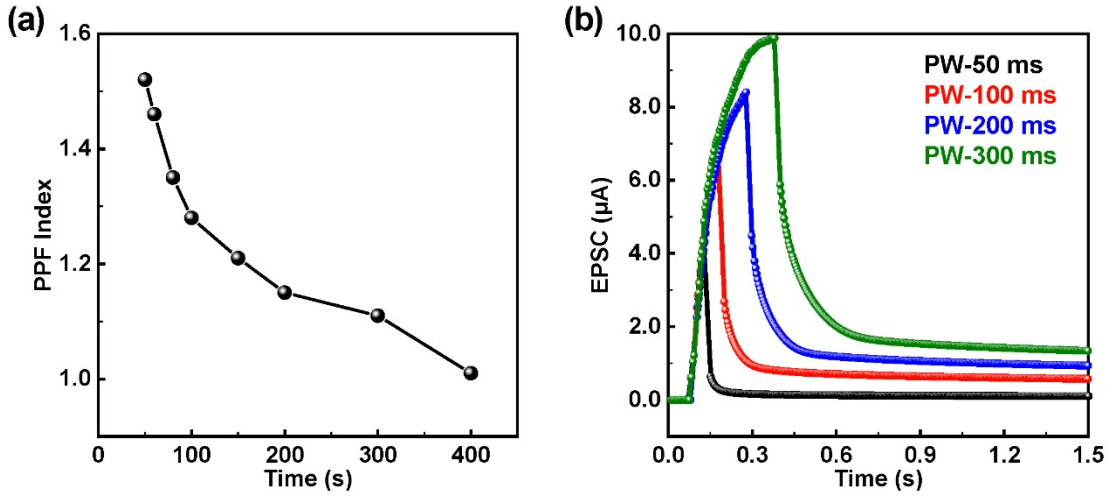

Figure 4-4. (a) Relationship between the PPF index and the time interval of applied pulse stimuli. (b) Artificial synaptic response to external pulses with various pulse widths.

Previous results have pointed that the Ag/SP-GaO_x/SP-AlO_x/ITO RRAM device could exhibit artificial synaptic behaviors based on the multi-level states of conductance and the synaptic current could be modulated by processing stimuli pulses. Multi-level conductance states with some desired tendency such as potentiation and depression could influence the connection amplitude or connection strength between two contiguous terminals. This amplitude or strength of the synaptic connection was named synaptic weight. [243-245] Therefore, a series of pulses were used to evaluate the synaptic response of one Ag/SP-GaO_x/SP-AlO_x/ITO RRAM device. As illustrated in **Fig. 4-5a**, the device exhibited multi-level conductance states with the external 50 consecutive electrical pules (0.5 V/10 ms), which demonstrated a short-term potentiation tendency of the synaptic weight and the conductance of the device was ~ 0.0555 mS. This artificial synaptic response emulated the biological short-term 'learning' behavior of the synapse. [5, 7, 51, 238] Then the external pulse stimuli were removed and the synaptic

weight started to decay. The first 8000 s retention test was conducted and the short-term depression was observed in **Fig. 4-5b**. This artificial synaptic response emulated the biological 'forgetting' behavior of the synapse. [5, 7, 51, 238] After 8000 s, the conductance of the device was decayed to ~ 0.2322 mS, which was very close to the initial conductance value. Then a series of electrical pulses were applied onto TE Ag. During this test, the device was at a high-conductance state around ~ 0.0555 mS again with only 27 consecutive pules, which indicated that the device demonstrated the STM characteristic, as illustrated in **Fig. 4-5c**. [5, 7, 51, 238]

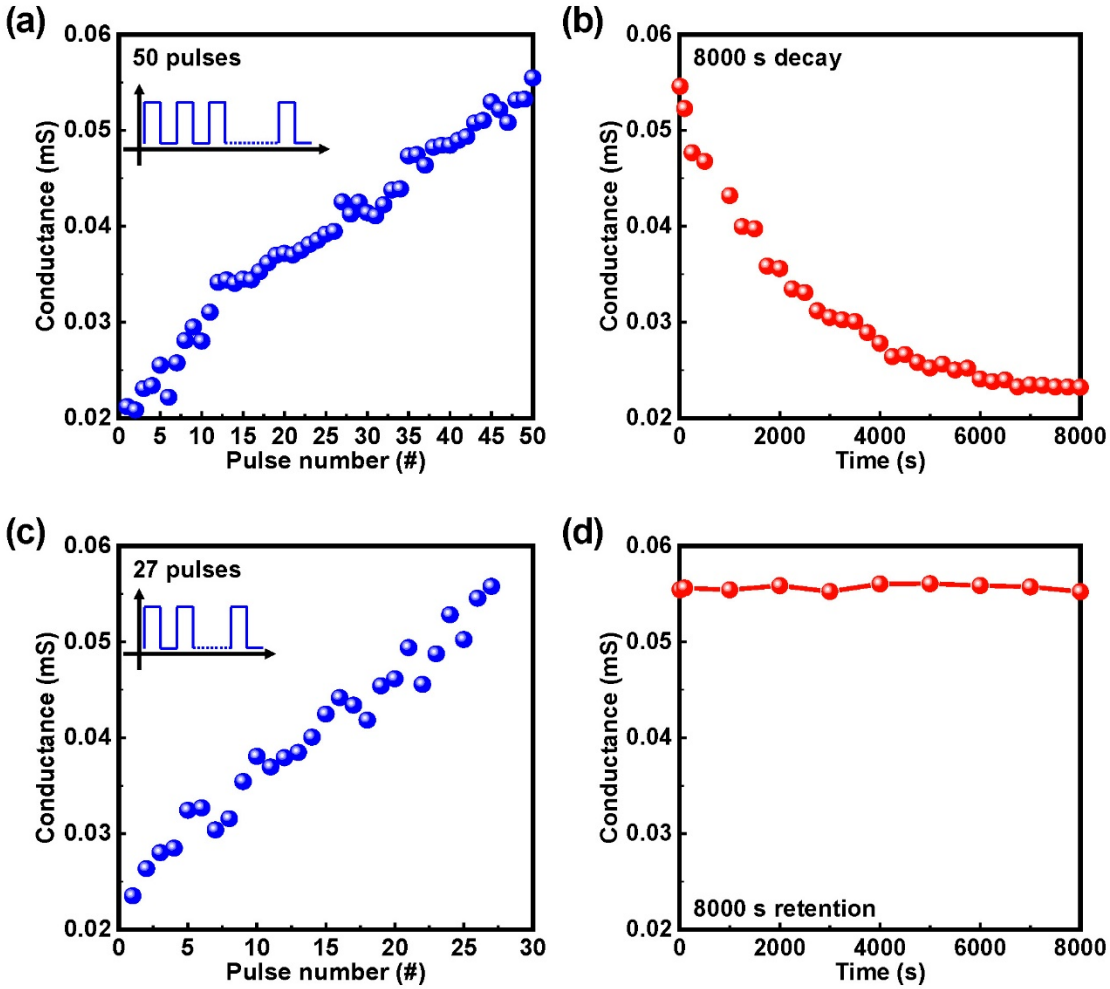

Figure 4-5. Emulation of 'learning - forgetting - re-learning' behaviors with the Ag/SP-GaO_x/SP-AlO_x/ITO RRAM device showing (a) potentiation conductance state with 50 pulses, (b) spontaneous decay with depression conductance state, (c) potentiation conductance state with 27 pulses, and (d) stable high-conductance state.

In **Fig. 4-5d,** The second 8000 s retention test was conducted and the device showed a stable high-conductance state longer than 8000 s, which indicated the successful emulation of biological 're-learning' behavior. [5, 7, 51, 238] The successful emulation of 'learning - forgetting - re-learning' also indicated that the short-term plasticity of this Ag/SP-GaO_x/SP-AlO_x/ITO RRAM device could transit to the long-term plasticity with the external stimuli. [5, 7, 51, 238] The performance in **Fig. 4-5** demonstrated the excellent synaptic response of one Ag/SP-GaO_x/SP-AlO_x/ITO RRAM device. In **Fig. 4-6**, a matrix with 20 devices was selected to emulate the transition from STM to LTM. **Fig. 4-6a** showed a scale bar of one device at different conductance states with various colors. **Fig. 4-6b** demonstrated an RRAM matrix with 20 devices. The height of the cylinder meant the conductance values of each device in this matrix. An array of 8 devices in this matrix was marked with the red framework, which indicated that these 8 devices with the shape of the letter 'L' would be chosen as the research objectives. **Fig. 4-6b** demonstrated an RRAM matrix with 20 devices. The height of the cylinder meant the conductance values of each device in this matrix. An array of 8 devices in this matrix was marked with the red framework, which indicated that these 8 devices with the shape of the letter 'L' would be chosen as the research objectives. In **Fig. 4-6c**, each device in the L array showed the potentiation tendency with multi-level conductance states. For each device, the pulse (0.5 V/10 ms) number of the stimuli was around ~ 50. The letter 'L' was presented in **Fig. 4-6c** emulated the brain-like STM characteristic of the matrix based on the learning ability of the single Ag/SP-GaO_x/SP-AlO_x/ITO RRAM device. [5, 7, 51, 238] In **Fig. 4-6d**, with all external stimuli of this array

removed from TE Ag, 8 devices in the marked array showed the depression tendency of conductance states, and their conductance values decayed close to the initial values at last, which emulate the brain-like forgetting characteristic. [5, 7, 51, 238] Then all devices in the L array were spiked with external electrical pulses (0.5 V/10 ms) again, as illustrated in **Fig. 4-6e**. The whole L array was at a high-conductance state after the stimuli and the number of pulses applied onto each device was lower than 30, which emulated the brain-like re-learning characteristic. [5, 7, 51, 238] After removing all pulse stimuli of each device in the L array, selected 8 devices in the L array still showed high-conductance states after 8000 s (**Fig. 4-6f**), which emulated the brain-like memorizing characteristic and realized the successful transition from STM to LTM. [5, 7, 51, 238]

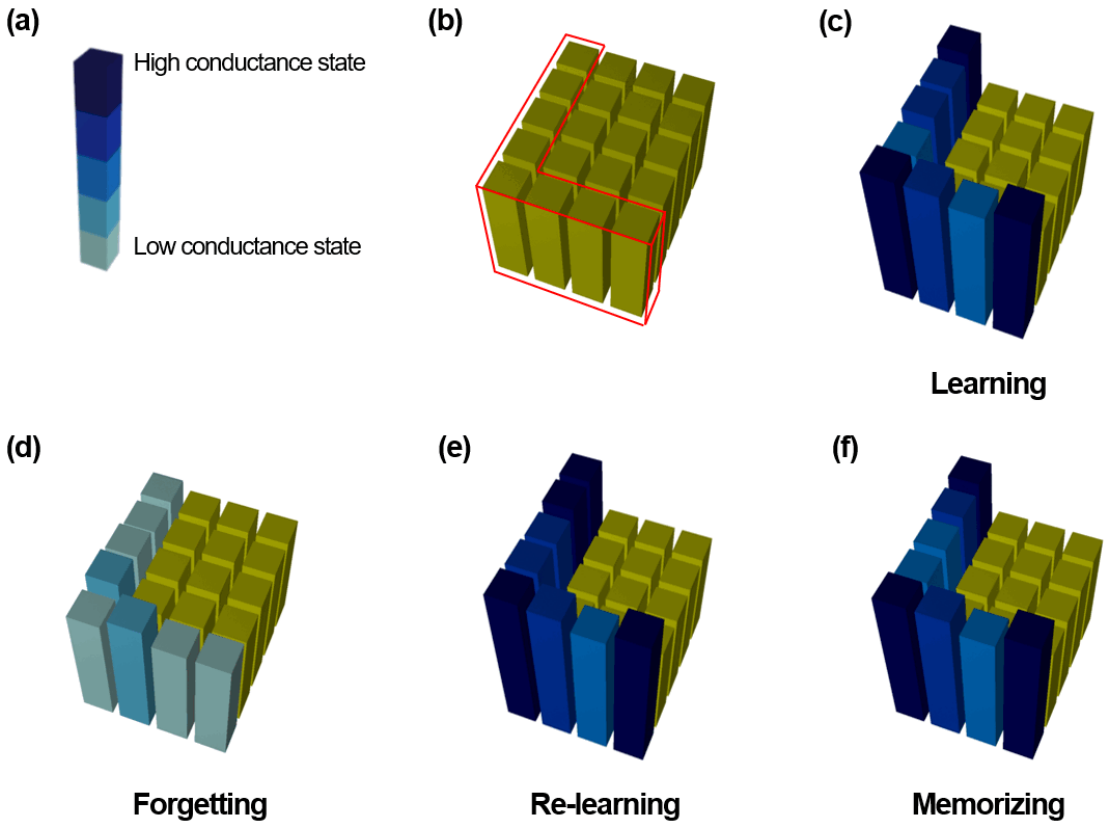

Figure 4-6. (a) Scale bar of an Ag/SP-GaO_x/SP-AlO_x/ITO RRAM device at various conductance states. Transition from STM to LTM of a selected array in the matrix and emulated the memorizing

process of the 'L' shape with (b) initial state, (c) learning state, (d) forgetting state, (e) re-learning state, and (f) memorizing state.

Apart from the short-term plasticity and the transition from short-term plasticity to long-term plasticity of the Ag/SP-GaO_x/SP-AlO_x/ITO RRAM device, the long-term plasticity with LTP and LTD was also evaluated by applying more consecutive electrical pulses. As illustrated in **Fig. 4-7a**, LTP and LTD behaviors were triggered by 100 positive pulse stimuli (+ 0.5 V/10 ms) and 100 negative pulse stimuli (- 0.5 V/10 ms), which indicated the excellent long-term plasticity of the Ag/SP-GaO_x/SP-AlO_x/ITO RRAM device.

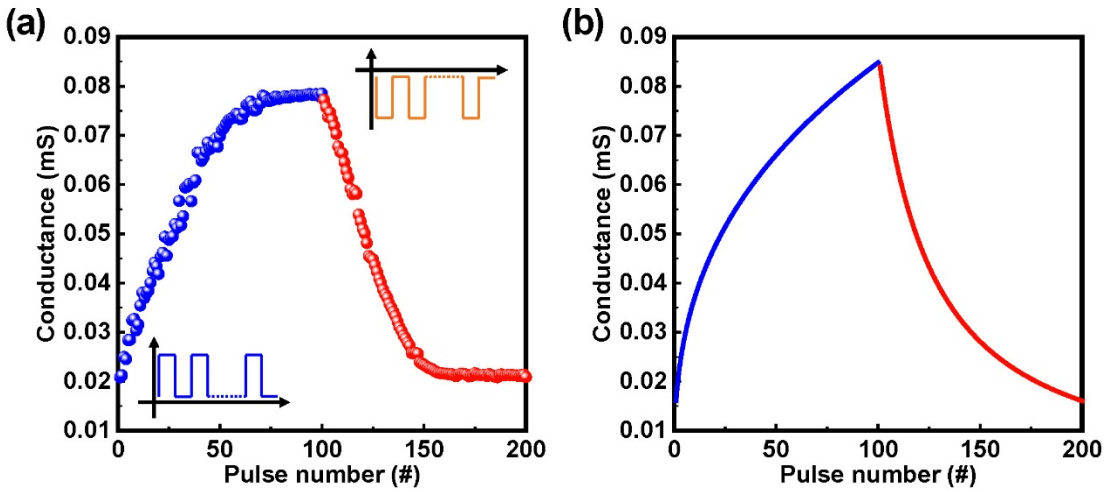

Figure 4-7. (a) Artificial synaptic performance of the long-term plasticity with LTP and LTD. (b) Results of nonlinearity for fitting curves of LTP and LTD.

Based on the previous research results of artificial synaptic behaviors of the Ag/SP-GaO_x/SP-AlO_x/ITO RRAM device, a neuromorphic system was established with the ANN algorithm in MATLAB, which was used to emulate a pattern recognition process. Evidence has suggested that humans receive the most external information through the

visual perception system. [246-248] The normal life of human beings cannot be separated from vision and the content of vision depends on the light reflected on the surface of things. [246-249] For the human brain, the optical signal hit on the retina induces the signal transfer process between the retina and the synapses in the human brain. The transfer process depended on the biological electrical potential induced by the drift of Ca^{2+}. For the RRAM device, the switching process and related artificial synaptic behaviors were also influenced by the change of electrical charge in the stacked switching layers. All artificial synaptic behaviors of the Ag/SP-GaO_x/SP-AlO_x/ITO RRAM device were determined by the operations of electrical programming and electrical erasing. Therefore, this recognition process emulated the image recognition of the human eyes and the optical input signal was replaced by the electrical input signal, as illustrated in **Fig. 4-8a**. Handwriting Arabic numbers 0 ~ 9 were selected as the recognition objectives. As illustrated in **Fig. 4-8b**, this recognition system included 784 input neurons and 10 output neurons. 784 input neurons constructed the input layer with a 28 × 28 matrix while the output layer consisted of 10 neurons. The connection state between the input layer and the output layer was determined by the synaptic weight, which was associated with the artificial synaptic characteristics of the Ag/SP-GaO_x/SP-AlO_x/ITO RRAM device. For this pattern recognition system.

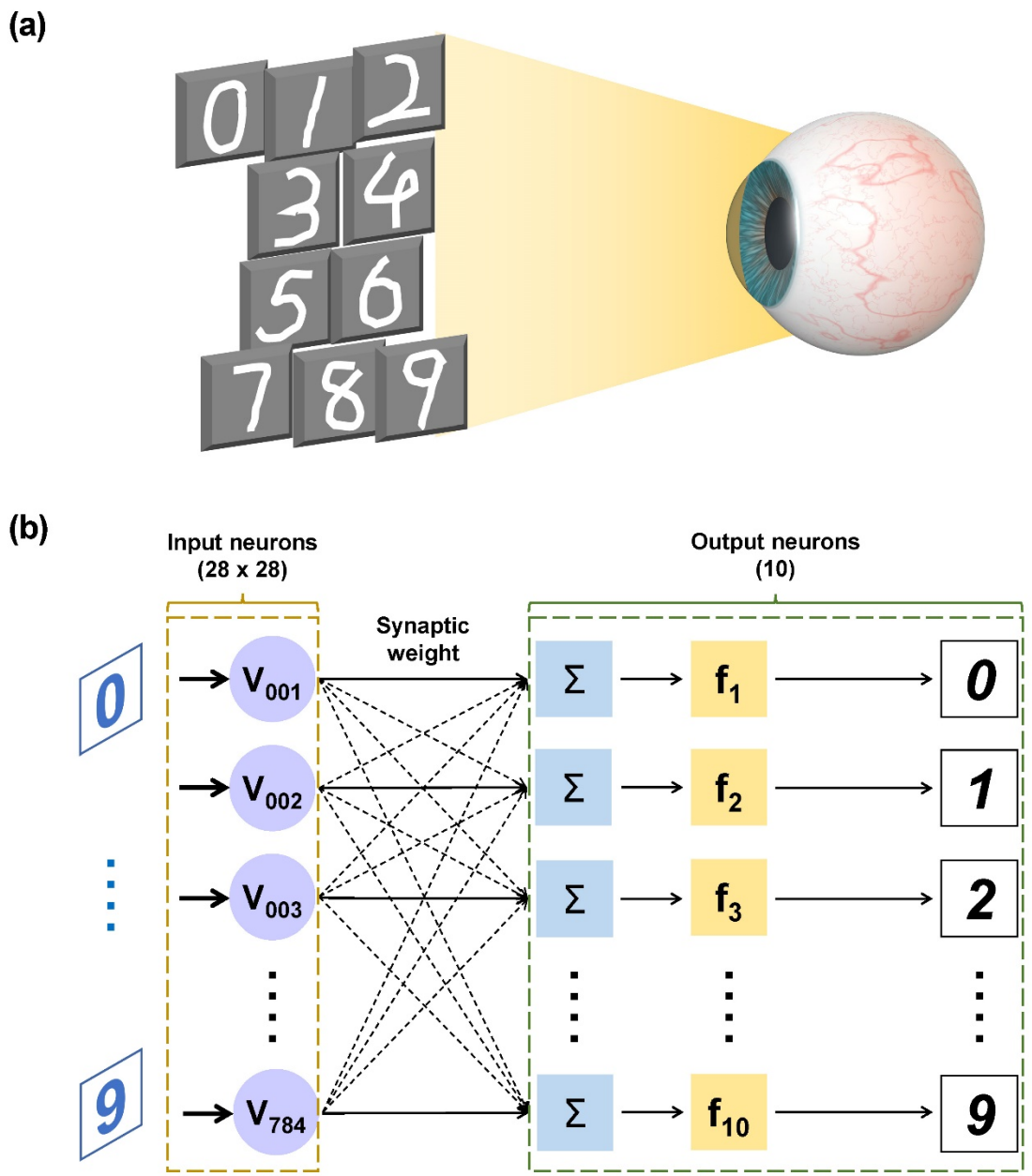

Figure 4-8. (a) Biological image recognition of the human eyes. (b) Schematic view of a pattern recognition system with a multiple-layer structure.

For this pattern recognition system based on the ANN algorithm, several parameters were required, which could be observed in **Table 4-1**.

Table 4-1. Key parameters required for the ANN pattern recognition system

Key Parameters	Values
Learning rate (lr)	2

Maximum conductance value (*Gmax*)	7.84992×10^{-5}
Minimum conductance value (*Gmin*)	2.08503×10^{-5}
LTP nonlinearity (NL_{LT-P})	0.64044
LTD nonlinearity (NL_{LT-D})	0.14886
Input size	784
Output size	10
Training time	3000

As illustrated in **Table 4-1**, among these parameters, some parameters received more attention, including LTP nonlinearity (NL_{LT-P}), LTD nonlinearity (NL_{LT-D}), the maximum value of the conductance (G_{MAX}), and the minimum value of the conductance (G_{MIN}). The upper limit and the lower limit of the program were regulated by G_{MAX} and G_{MIN} while the recognition accuracy of the final results was influenced by the nonlinearity of fitting curves for LTP and LTD behaviors, which has been demonstrated in **Fig. 4-7b**. With the fitting operation in **Fig. 4-7b**, G_{MAX} was 7.84992×10^{-5} mS and G_{MIN} was 2.08503×10^{-5} Ms while NL_{LT-P} was 0.64044 and NL_{LT-D} was 0.14886. Based on the origin values in the MNIST data set, the recognition results of numbers from 0 to 9 could be observed in **Fig. 4-9a** after training and the times of the training cycle were 3000. **Fig. 4-9b** showed the accuracy change during the whole recognition process and the statistic result was presented in **Fig. 4-9c**. The average accuracy of the pattern recognition process was around 87% and the highest recognition accuracy was ~ 96%.

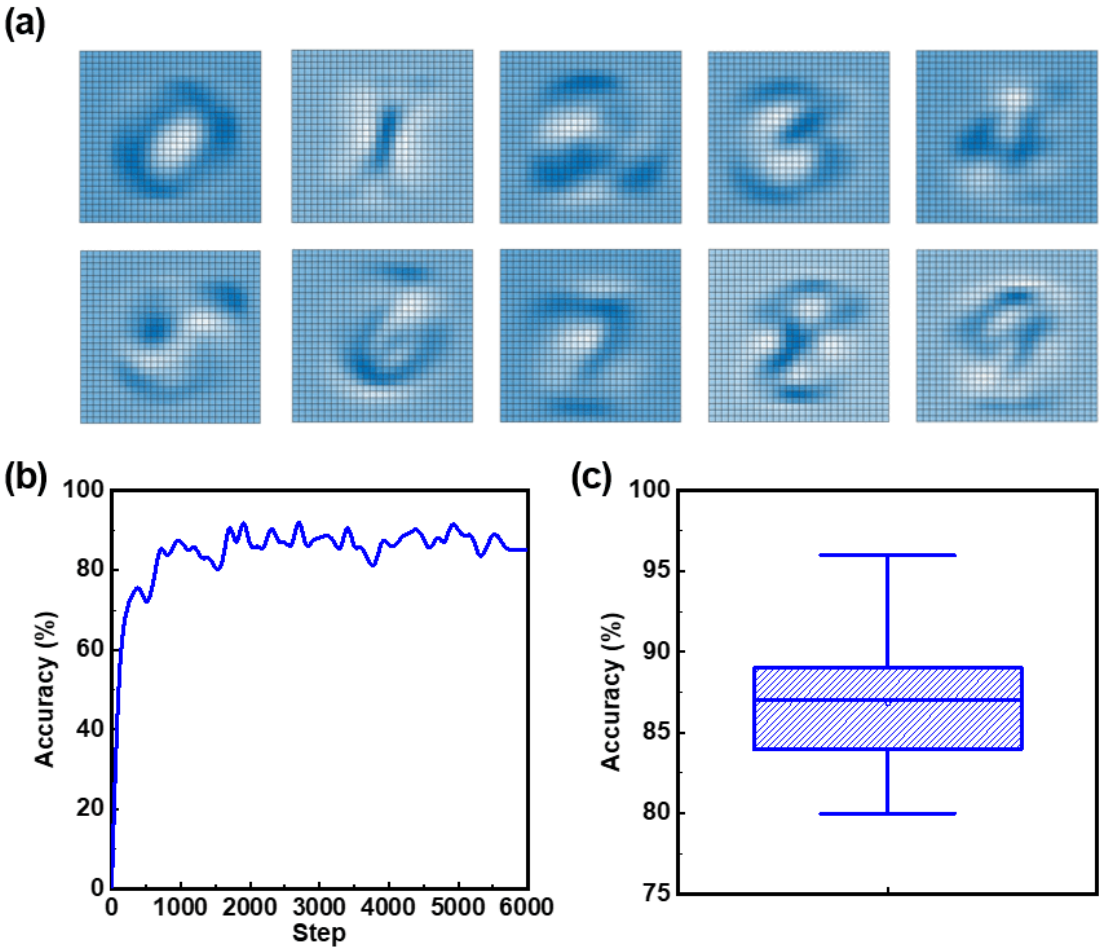

Figure 4-9. (a) Recognition results of numbers from 0 to 9 after 3000 times training. (b) The accuracy change of the system during the pattern recognition process. (c) The statistic result of the recognition accuracy.

During the measurement of artificial synaptic behaviors for LTP and LTD, an obvious plateau state of the conductance change was observed at the end of the LTP phase while a flat valley of conductance was observed at the end of the LTD phase, as illustrated in **Fig. 4-7a**. This phenomenon was associated with the saturation states of LTP and LTD response, which had a negative influence on the linearity of LTP and LTD curves. For the pattern recognition process mentioned above, better linearity (nonlinearity close to 0) of LTP and LTD curves could be helpful to improve the recognition accuracy. [10, 51, 239] Therefore, by controlling the number of consecutive electrical pulses, a modulation

method was conducted to the potentiation and depression response of the Ag/SP-GaO_x/SP-AlO_x/ITO RRAM device, which improved the linear tendency of the conductance change. (**Fig. 4-10a**). The statistic result of the recognition accuracy after improving LTP and LTD nonlinearity was presented in **Fig. 4-10b**, numbers were recognized with an average accuracy of ~ 94% and the highest average accuracy was about 98%.

Besides the assessment of the long-term plasticity, another measurement, STDP, of the Ag/SP-GaO_x/SP-AlO_x/ITO RRAM device was also conducted, which was a plasticity that related to time dependency of input spikes. [10, 51, 239] The performance of STDP was influenced by the sequence and time interval (Δt) of spikes applied onto the presynaptic neuron and the postsynaptic neuron. As illustrated in **Fig. 4-10c**, when the presynaptic neuron was spiked at first and the postsynaptic neuron was spiked after the time of Δt ($\Delta t > 0$), the connection between two adjacent synaptic neurons was strengthened and a potentiation tendency (LTP) of synaptic weight occurred. On the contrary, if the postsynaptic neuron was activated by the external spike before the spiking stimuli arrived at the presynaptic neuron ($\Delta t > 0$), the synaptic weight demonstrated the depression performance (LTD), and the connection strength between two adjacent synaptic neurons was weakened. [10, 51, 239] Therefore, an asymmetrical Hebbian STDP performance was presented in **Fig. 4-10d**.

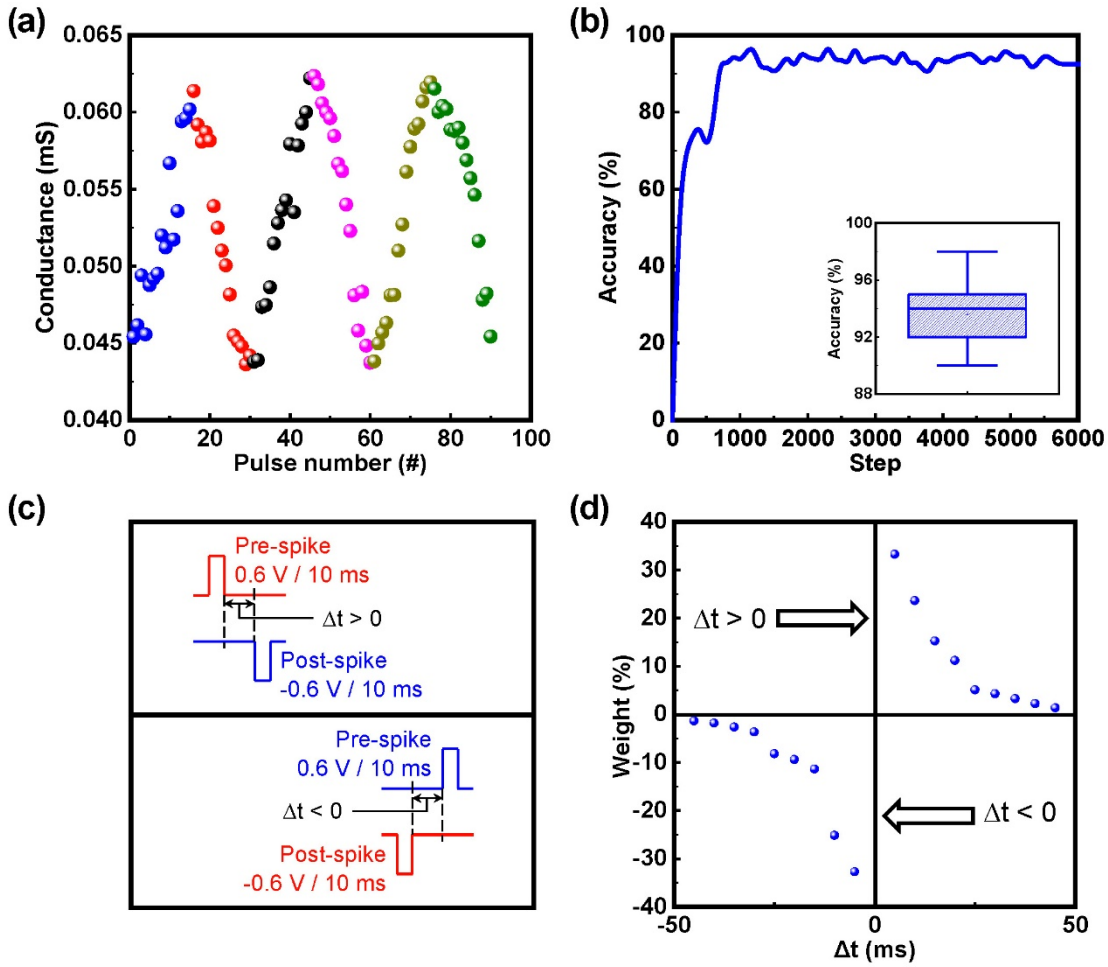

Figure 4-10. (a) Improvement of the linearity of LTP and LTD by controlling the number of electrical pulses. (b) Enhanced recognition accuracy of the pattern recognition process with the improvement of LTP and LTD linearity. (c) Input spike sequence of the STDP measurement. (d) SRDP performance of the Ag/SP-GaO_x/SP-AlO_x/ITO RRAM device based on Hebbain's rule.

4.4 Conclusion

In this chapter, the artificial synaptic performance of the Ag/SP-GaO_x/SP-AlO_x/ITO RRAM device was investigated. The multi-level RS behavior indicated the multiple states of the conductance and revealed the potential of the synaptic device. With the external electrical pulses as the artificial stimuli, the Ag/SP-GaO_x/SP-AlO_x/ITO device displayed artificial synaptic behaviors, including EPSC, PPF, LTP, LTD, STM, and

LTM. The single device demonstrated the transition from STM to LTM, which resulted in an integrated array to emulate the biomimetic behaviors of ‘learning - forgetting - relearning - memorizing’. In addition, based on key parameters of the long-term plasticity, an ANN recognition process was carried out with the highest recognition accuracy of ~ 98%.

4.5 References

[5] S. Dai, Y. Zhao, Y. Wang, J. Zhang, L. Fang, S. Jin, Y. Shao, and J. Huang, "Recent Advances in Transistor-Based Artificial Synapses," *Advanced Functional Materials,* vol. 29, no. 42, pp. 1903700(1-23), 2019.

[6] H. Han, H. Yu, H. Wei, J. Gong, and W. Xu, "Recent Progress in Three-Terminal Artificial Synapses: From Device to System," *Small,* vol. 15, no. 32, pp. e1900695(1-17), Aug 2019.

[7] C. Wan, P. Cai, M. Wang, Y. Qian, W. Huang, and X. Chen, "Artificial Sensory Memory," *Adv Mater,* vol. 32, no. 15, pp. e1902434(1-22), Apr 2020.

[8] H. Xu, L. Yin, C. Liu, X. Sheng, and N. Zhao, "Recent Advances in Biointegrated Optoelectronic Devices," *Adv Mater,* vol. 30, pp. e1800156(1-22), May 28 2018.

[10] Z. Shen, C. Zhao, Y. Qi, W. Xu, Y. Liu, I. Z. Mitrovic, L. Yang, and C. Zhao, "Advances of RRAM Devices: Resistive Switching Mechanisms, Materials and Bionic Synaptic Application," *Nanomaterials (Basel),* vol. 10, no. 8, pp. 1437(1-31), Jul 23 2020.

[16] A. Sawa, "Resistive switching in transition metal oxides," *Materials Today,* vol. 11, no. 6, pp. 28-36, 2008.

[46] L. Chen, C. Li, T. Huang, Y. Chen, S. Wen, and J. Qi, "A synapse memristor model with forgetting effect," *Physics Letters A,* vol. 377, no. 45-48, pp. 3260, 2013.

[50] Y. Zhai, J.-Q. Yang, Y. Zhou, J.-Y. Mao, Y. Ren, V. A. L. Roy, and S.-T. Han, "Toward non-volatile photonic memory: concept, material and design," *Materials Horizons,* vol. 5, no. 4, pp. 641-654, 2018.

[51] Z. Shen, C. Zhao, T. Zhao, W. Xu, Y. Liu, Y. Qi, I. Z. Mitrovic, L. Yang, and C. Z. Zhao, "Artificial Synaptic Performance with Learning Behavior for Memristor Fabricated with Stacked Solution-Processed Switching Layers," *ACS Applied Electronic Materials,* vol. 3, no. 3, pp. 1288-1300, 2021.

[62] X. Hong, D. J. Loy, P. A. Dananjaya, F. Tan, C. Ng, and W. Lew, "Oxide-based RRAM materials for neuromorphic computing," *Journal of Materials Science,*

vol. 53, no. 12, pp. 8720-8746, 2018.

[63] V. Gupta, S. Kapur, S. Saurabh, and A. Grover, "Resistive Random Access Memory: A Review of Device Challenges," *IETE Technical Review,* vol. 37, no. 4, pp. 377-390, 2019.

[200] S. Kim, B. Choi, M. Lim, Y. Kim, H. D. Kim, and S. J. Choi, "Synaptic Device Network Architecture with Feature Extraction for Unsupervised Image Classification," *Small,* vol. 14, no. 32, pp. e1800521(1-9), Aug 2018.

[234] V. Milo, A. Glukhov, E. Perez, C. Zambelli, N. Lepri, M. K. Mahadevaiah, E. P.-B. Quesada, P. Olivo, C. Wenger, and D. Ielmini, "Accurate Program/Verify Schemes of Resistive Switching Memory (RRAM) for In-Memory Neural Network Circuits," *IEEE Transactions on Electron Devices,* vol. 68, no. 8, pp. 3832-3837, 2021.

[235] C. Zhang, Y.-T. Tai, J. Shang, G. Liu, K.-L. Wang, C. Hsu, X. Yi, X. Yang, W. Xue, H. Tan, S. Guo, L. Pan, and R.-W. Li, "Synaptic plasticity and learning behaviours in flexible artificial synapse based on polymer/viologen system," *Journal of Materials Chemistry C,* vol. 4, no. 15, pp. 3217(1-17), 2016.

[236] S. Zhao, Z. Ni, H. Tan, Y. Wang, H. Jin, T. Nie, M. Xu, X. Pi, and D. Yang, "Electroluminescent synaptic devices with logic functions," *Nano Energy,* vol. 54, pp. 383-389, 2018.

[237] E. Goi, Q. Zhang, X. Chen, H. Luan, and M. Gu, "Perspective on photonic memristive neuromorphic computing," *PhotoniX,* vol. 1, no. 3, pp. 1-26, 2020.

[238] W. Huang, P. Hang, Y. Wang, K. Wang, S. Han, Z. Chen, W. Peng, Y. Zhu, M. Xu, Y. Zhang, Y. Fang, X. Yu, D. Yang, and X. Pi, "Zero-power optoelectronic synaptic devices," *Nano Energy,* vol. 73, pp. 104790(1-9), 2020.

[239] X. Liao, W. Song, X. Zhang, H. Jin, S. Liu, Y. Wang, A. V. Y. Thean, and Y. Zheng, "An Artificial Peripheral Neural System Based on Highly Stretchable and Integrated Multifunctional Sensors," *Advanced Functional Materials,* pp. 2101107(1-11), 2021.

[240] M. Park, M. Kang, and S. Kim, "Pulse frequency dependent synaptic characteristics in Ta/SiN/Si memristor device for neuromorphic system," *Journal of Alloys and Compounds,* vol. 882, pp. 160760(1-6), 2021.

[241] T. Y. Wang, J. L. Meng, L. Chen, H. Zhu, Q. Q. Sun, S. J. Ding, W. Z. Bao, and D. W. Zhang, "Flexible 3D memristor array for binary storage and multi-states neuromorphic computing applications," *InfoMat,* vol. 3, no. 2, pp. 212-221, 2020.

[242] T.-Y. Wang, J.-L. Meng, Q.-X. Li, Z.-Y. He, H. Zhu, L. Ji, Q.-Q. Sun, L. Chen, and D. W. Zhang, "Reconfigurable optoelectronic memristor for in-sensor computing applications," *Nano Energy,* vol. 89, pp. 106291(1-8), 2021.

[243] M. Ismail, U. Chand, C. Mahata, J. Nebhen, and S. Kim, "Demonstration of synaptic and resistive switching characteristics in W/TiO_2/HfO_2/TaN memristor crossbar array for bioinspired neuromorphic computing," *Journal of Materials Science & Technology,* vol. 96, pp. 94-102, 2022.

[244] M. Ismail, H. Abbas, A. Sokolov, C. Mahata, C. Choi, and S. Kim, "Emulating synaptic plasticity and resistive switching characteristics through amorphous

Ta_2O_5 embedded layer for neuromorphic computing," *Ceramics International,* vol. In press, 2021.

[245] J. Yang, H. Cho, H. Ryu, M. Ismail, C. Mahata, and S. Kim, "Tunable Synaptic Characteristics of a Ti/TiO_2/Si Memory Device for Reservoir Computing," *ACS Appl Mater Interfaces,* vol. 13, no. 28, pp. 33244-33252, Jul 21 2021.

[246] H.-T. Hsu, D.-L. Yang, L. D. Wiyanto, and J.-Y. Chen, "Red-Light-Stimulated Photonic Synapses Based on Nonvolatile Perovskite-Based Photomemory," *Advanced Photonics Research,* vol. 2, no. 5, pp. 2000185, 2021.

[247] L. M. Gurtner, M. Hartmann, and F. W. Mast, "Eye movements during visual imagery and perception show spatial correspondence but have unique temporal signatures," *Cognition,* vol. 210, pp. 104597, May 2021.

[248] V. Conboy, C. Edwards, R. Ainsworth, D. Natusch, C. Burcham, B. Danisment, S. Khot, R. Seymour, S. J. Larcombe, I. Tracey, and J. Kolasinski, "Chronic musculoskeletal impairment is associated with alterations in brain regions responsible for the production and perception of movement," *J Physiol,* vol. 599, no. 8, pp. 2255, Apr 2021.

[249] J. A. F. Fabio Pellacini, Donald P. Greenberg, "Toward a psychophysically-based light reflection model for image synthesis," in *27th annual conference on Computer graphics and interactive techniques*, New Orleans, LA USA, 2000, p. 55: SIGGRAPH.

Chapter 5: Conclusion and outlook

5.1 Conclusion

In this thesis, the foundation of all RRAM devices was the RS behavior of the SP RS layers fabricated from the spin-coating technique. In **Chapter 1**, the background introduction of RRAM devices and advantages of SP techniques were introduced. In **Chapter 2**, TiN/SP-AlO_x/Pt and Ni/SP-AlO_x/Pt RRAM devices were fabricated. The performance variation between these two devices was under investigation at first, which was associated with the difference of $\Delta\Phi_M$ induced by the material variation of Ni and TiN. Ni/SP-AlO_x/Pt devices under each annealing temperature exhibited better performance with lower operation voltages (< 1.5 V), more stable ON/OFF ratio (> 10^2), and enhanced stability (retention time > 10^4 s and endurance cycles > 150), which was contributed to the smaller $\Delta\Phi_M$ between TE Ni and BE Pt. The Φ_M was defined as the minimum energy consumption of the escape process of electrons and the escape direction was from the inside of the metal to the vacuum. Therefore, a larger Φ_M indicated that it was harder for electrons to escape. $\Delta\Phi_M$ still influenced the whole drift process of electrons and the higher $\Delta\Phi_M$ indicated that it was required more energy to support the electron drift, which presented the RS behavior with higher voltage. Compared with the $\Delta\Phi_M$ between TE TiN and BE Pt, $\Delta\Phi_M$ between Ni and Pt was smaller than that between TiN and Pt (0.58 eV < 1.53 eV). Hence, a lower V_{SET} of Ni/SP-AlO_x/Pt device was needed during the SET process. During the RESET process, lower energy demand was required to cancel the band bending of the SP-AlO_x layer,

which indicated the lower operation voltages were needed during the RS process. Apart from the research between Ni/SP-AlO_x/Pt and TiN/SP-AlO_x/Pt RRAM devices, the investigation on SP-AlO_x layers annealed at different temperatures (225°C, 250°C, and 275°C) of the Ni/SP-AlO_x/Pt devices was also carried out and the best electrical performance was obtained on the Ni/SP-AlO_x/Pt device with the SP-AlO_x thin film annealed at 250°C, which was contributed to the concentration variation of M-O and -OH influenced by the annealing temperature. For an SP-AlO_x layer, M-O and -OH indicated the existence of AlO_x and $Al(OH)_x$, these two components played dominating roles in the formation/rupture process of CF based on oxygen vacancy. With the increase of the annealing temperature, the concentration of -OH was higher than M-O, which revealed that the -OH played a more important role. For the SP-AlO_x thin film annealed at 250°C, the lowest roughness due to the highest -OH concentration was helpful to the sufficient accumulation of oxygen vacancies. Therefore, the Ni/SP-AlO_x/Pt RRAM device with a 250°C annealed SP-AlO_x layer demonstrated the best electrical performance with the lowest operation voltage, stablest ON/OFF ratio, and the best stability. Other samples showed electrical performance that was not as good as those of 250°C annealed samples, which was contributed to the lower concentration of -OH in their SP-AlO_x thin films annealed at 225°C and 275°C. [110, 112]

In **Chapter 3**, based on the investigation on RS behavior of the SP-AlO_x thin films, improvement techniques were considered to improve the electrical performance of the RRAM device. For the improvement of the electrode layer, TE Ni was replaced with

TE Ag, and BE Pt was replaced by BE ITO. For the improvement of the RS layer, According to the comprehensive comparison among Ag/SP-InO_x/ITO, Ag/SP-GaO_x/ITO, and Ag/GO/ITO RRAM devices with single SP RS layers, the SP-GaO_x layer was selected as the upper component of the stacked SP-X/SP-AlO_x layer, which resulted in the SP-GaO_x/SP-AlO_x layer. Further electrical characterizations confirmed the success of improvement methods. The Ag/SP-GaO_x/SP-AlO_x/ITO RRAM device displayed enhanced RS behaviors with an operation voltage lower than 0.6 V, an ON/OFF ratio larger than 2×10^4, a retention time longer than 2×10^4 s, and retention cycles over 200. With the measurement of metallic temperature dependency for the Ag/SP-GaO_x/SP-AlO_x/ITO RRAM device at LRS, the metallic CF based on the oxidation and reduction reaction of Ag atoms was considered to be responsible for the RS process. In addition, compared with the Ag/SP-AlO_x/ITO RRAM device, the Ag/SP-GaO_x/SP-AlO_x/ITO device had a higher rate of redox reaction and ion mobility due to the existence of the SP-GaO_x thin film, which was more beneficial to the formation of Ag CF and then resulted in the lower energy consumption with the lower voltage. [51]

In **Chapter 4**, based on the enhanced electrical performance in **Chapter 3**, the multi-level states of current and conductance for the Ag/SP-GaO_x/SP-AlO_x/ITO RRAM device were confirmed with different electrical characterization methods, which indicated the great potential of the Ag/SP-GaO_x/SP-AlO_x/ITO RRAM device as the artificial synaptic devices. According to the gradual change of the conductance states,

artificial synaptic behaviors of the Ag/SP-GaO_x/SP-AlO_x/ITO RRAM device were investigated based on the response to electrical pulses, including EPSC, PPF, LTP, LTD, STM, LTM, and STDP. With the successful transition from short-term plasticity to long-term plasticity of the single device, an array with multiple devices emulated the biomimetic behaviors of 'learning – forgetting- re-learning - memorizing'. In addition, some vital parameters of the artificial synaptic behaviors were used in an ANN recognition system and handwriting Arabic numbers (0 ~ 9) were recognized with high recognition accuracy after multiple training processes. [51]

5.2 Outlook

Results and discussion in this thesis have indicated the promising prospect of exploring devices with artificial synaptic behaviors, which is also supported by many other published works. [8, 50, 51, 110, 112] However, current synaptic devices (three-terminal transistor, two-terminal memristor, and atomic switch) represented by the popular NVM are significantly affected by the purely electronic control, which has an important influence on electrical input/output, delay of resistance-capacitance (RC) interconnection, and circuit crosstalk. [10, 11, 51, 99, 100, 250-256] As mentioned before, the final aim of developing artificial synaptic devices with better performance was to prompt the digital computer could think and judge like the human brain. For the information input of the human brain, most of them were accepted by the biological visual system. [246-248] When light hits the surface of an object, the reflected light reaches

the retina in the eye and transmits stimulus information to neuron systems in the brain. The brain will ultimately determine what it is seeing. [246-249] The investigation of optogenetics of biological neuroscience also promoted the integration of light and synaptic devices, which resulted in optical synaptic devices. [250-252, 257] Compared with synaptic devices that rely on electrical control, optical synaptic devices could realize the interconversion between optical and electrical signals, which had a positive influence on the integration of the optical neuron network system. [237, 257-259] Optical synaptic devices also exhibited advantages with low circuit crosstalk, high operation speed, large bandwidth, and ignorable RC delay. [237, 250, 258] In addition, optical synaptic devices also revealed the utilization potential in the application of signal processing, image recognition, and visual sensory. [237, 250, 258, 260] Therefore, it is significant to explore the artificial synaptic behavior induced by external optical stimuli.

I also completed related review work on optical synaptic devices. One of the most serious constraints on the research of optical synaptic devices is the utilization of materials. Compared with the electrical synaptic device like the Ag/SP-GaO_x/SP-AlO_x/ITO RRAM device in this thesis, the materials required for optical synaptic devices must have both high electrical conductivity and high optical sensitivity. For now, some materials have been investigated as the optical-response RS layer, including perovskites, metal oxides, organics, and low-dimensional nanomaterials, as illustrated in **Fig. 5-1**. [24, 47, 48, 101, 261-272] Perovskites have shown high electro-optic conversion efficiency, metal oxides have exhibited high-carrier-mobility and excellent

transparency, while organics also demonstrated advantages like low-temperature manufacturing and degradability. [24, 47, 48, 101, 261-272] These properties have made these conventional materials become popular candidates during the research of artificial optical synapses.

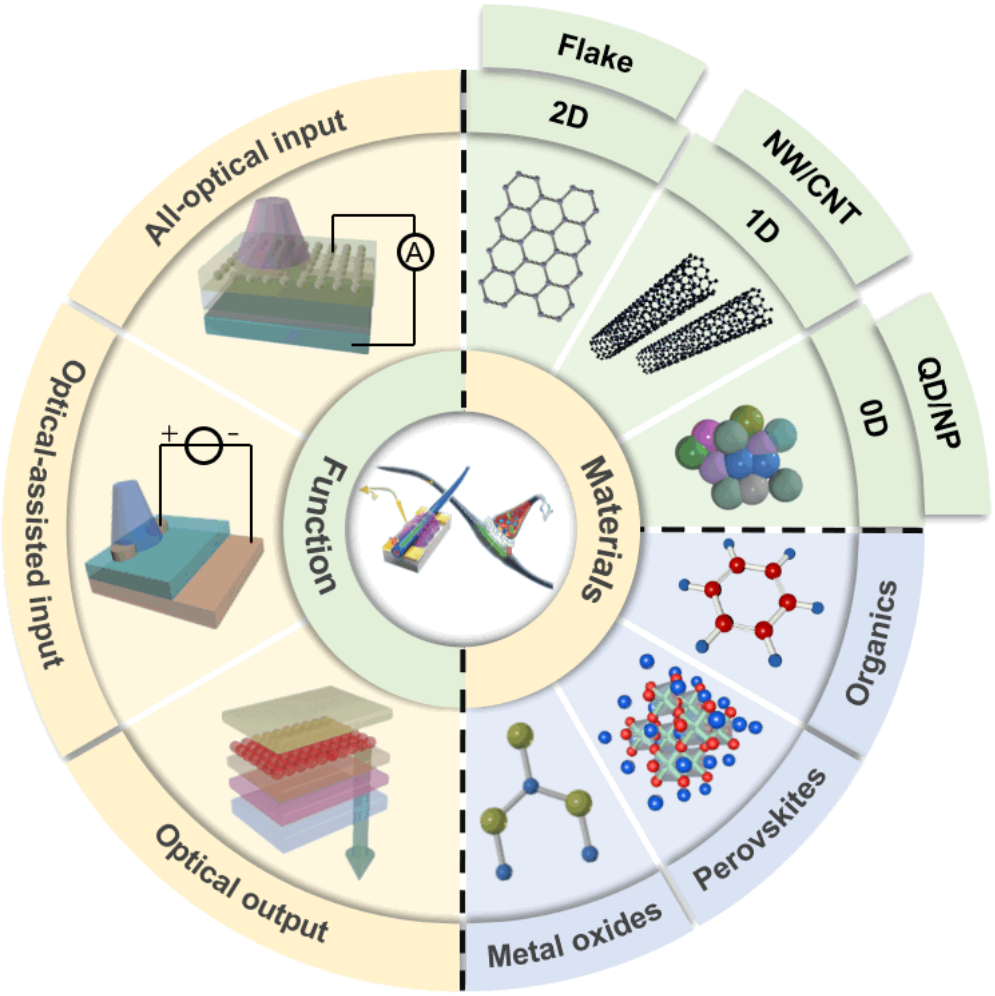

Figure 5-1. Function category of optical synaptic devices with forms of all-optical-input, optical-assisted input, and optical output. Materials category of optical synaptic devices including metal oxides, organics, perovskites, and low-dimensional (0D, 1D, and 2D) materials.

Among thesis materials, Low-dimensional materials (zero dimension-0D, one dimension-1D, and two dimension-2D) such as $CsPbBr_3$ quantum dot (QD), InAs

nanowire, and MoS_2 nanosheet have received incredible growing interest due to their unique advantages like nonlinear optical character, high optical-sensitivity efficiency, and wide-bandgap in the field of photoelectric conversion. [10, 11, 250-253, 273] Besides, other properties including ease of preparation, low leakage current, and feasibility of bandgap modulation also make low-dimensional nanomaterials attractive and popular to researchers of microelectronic devices. Many reports also provided evidence of developing artificial optical devices based on low-dimensional nanomaterials.

At present, various factors are influencing the performance of optical synaptic devices in terms of structure, size, energy consumption, materials categories, and input source, which results in that there is no general standard to define the performance of optical synaptic devices. For a fully optical-control synaptic device, the inhibitory and excitatory of PSC is completely affected by the power intensity, optical frequency, and wavelength of input optical stimuli. Photo-induced carriers in the functional layers determined the optical-electronic response of the device. For an optical synaptic device with a three-terminal structure, the inhibitory response of PSC is almost controlled by electrical stimuli and the operation power is always in the range from several tens of nanowatts to several micro-watts. Compared with the power level in the biological neuron system from 1fJ to 100fJ, the artificial neuron network requires extra energy consumption during the operation process. Low-dimensional materials with high optical sensitivity, nanoscale structure, and high electrical conductivity enhance the feasibility of performance optimization and energy consumption reduction. In addition,

properties like manageable transport rates of charge carrier, relatively high trap density, atomic-level thickness structure are conducive to the utilization of 0D, 1D, and 2D materials in further research on artificial neuromorphic computing. The final goal of researching optical synaptic devices is to realize the high integration of the neuromorphic system in hardware while ensuring excellent device performance and reducing device energy consumption, which indicated the tendency of shrinking the size of optical synaptic devices. The nano-scale structure of low-dimensional materials makes them become extremely competitive candidates in the future. In the field of optoelectronic devices fabricated with silicon-based materials, feasible and relative-mature experiences have been obtained when investigating computing operations based on von Neuman architecture. These experiences will positively affect the exploration of information interconnection between optical and electrical signals, which also reveals that brain-inspired optical synaptic devices applicated in neuromorphic systems will also benefit from these advanced experiences. In addition to sensing external optical stimuli, future optical synaptic devices may integrate optical-sensing, neuromorphic computing, and non-volatile memory to better adapt to artificial intelligence in the Internet of Things (IoT) environment.

5.3 References

[8] H. Xu, L. Yin, C. Liu, X. Sheng, and N. Zhao, "Recent Advances in Biointegrated Optoelectronic Devices," *Adv Mater,* vol. 30, pp. e1800156(1-22), May 28 2018.

[10] Z. Shen, C. Zhao, Y. Qi, W. Xu, Y. Liu, I. Z. Mitrovic, L. Yang, and C. Zhao, "Advances of RRAM Devices: Resistive Switching Mechanisms, Materials and

Bionic Synaptic Application," *Nanomaterials (Basel),* vol. 10, no. 8, pp. 1437(1-31), Jul 23 2020.

[11] Z. Shen, C. Zhao, Y. Qi, I. Z. Mitrovic, L. Yang, J. Wen, Y. Huang, P. Li, and C. Zhao, "Memristive Non-Volatile Memory Based on Graphene Materials," *Micromachines (Basel),* vol. 11, no. 4, pp. 341(1-26), Mar 25 2020.

[24] L. Shao, H. Wang, Y. Yang, Y. He, Y. Tang, H. Fang, J. Zhao, H. Xiao, K. Liang, M. Wei, W. Xu, M. Luo, Q. Wan, W. Hu, T. Gao, and Z. Cui, "Optoelectronic Properties of Printed Photogating Carbon Nanotube Thin Film Transistors and Their Application for Light-Stimulated Neuromorphic Devices," *ACS Appl Mater Interfaces,* vol. 11, no. 12, pp. 12161, Mar 27 2019.

[47] M. Kumar, S. Abbas, and J. Kim, "All-Oxide-Based Highly Transparent Photonic Synapse for Neuromorphic Computing," *ACS Appl Mater Interfaces,* vol. 10, no. 40, pp. 34370, Oct 10 2018.

[48] M. Lee, W. Lee, S. Choi, J. W. Jo, J. Kim, S. K. Park, and Y. H. Kim, "Brain-Inspired Photonic Neuromorphic Devices using Photodynamic Amorphous Oxide Semiconductors and their Persistent Photoconductivity," *Adv Mater,* vol. 29, no. 28, pp. 1700951, Jul 2017.

[50] Y. Zhai, J.-Q. Yang, Y. Zhou, J.-Y. Mao, Y. Ren, V. A. L. Roy, and S.-T. Han, "Toward non-volatile photonic memory: concept, material and design," *Materials Horizons,* vol. 5, no. 4, pp. 641-654, 2018.

[51] Z. Shen, C. Zhao, T. Zhao, W. Xu, Y. Liu, Y. Qi, I. Z. Mitrovic, L. Yang, and C. Z. Zhao, "Artificial Synaptic Performance with Learning Behavior for Memristor Fabricated with Stacked Solution-Processed Switching Layers," *ACS Applied Electronic Materials,* vol. 3, no. 3, pp. 1288-1300, 2021.

[99] C.-C. Chiang, V. Ostwal, P. Wu, C.-S. Pang, F. Zhang, Z. Chen, and J. Appenzeller, "Memory applications from 2D materials," *Applied Physics Reviews,* vol. 8, no. 2, pp. 021306(1-19), 2021.

[100] X. Jiang, Q. Liu, J. Xing, N. Liu, Y. Guo, Z. Liu, and J. Zhao, "Recent progress on 2D magnets: Fundamental mechanism, structural design and modification," *Applied Physics Reviews,* vol. 8, no. 3, pp. 031305(1-69), 2021.

[101] J. Zhang, Y. Lu, S. Dai, R. Wang, D. Hao, S. Zhang, L. Xiong, and J. Huang, "Retina-Inspired Organic Heterojunction-Based Optoelectronic Synapses for Artificial Visual Systems," *Research (Wash D C),* vol. 2021, pp. 7131895(1-10), 2021.

[110] Z. Shen, Y. Qi, I. Z. Mitrovic, C. Zhao, S. Hall, L. Yang, T. Luo, Y. Huang, and C. Zhao, "Effect of Annealing Temperature for Ni/AlO_X/Pt RRAM Devices Fabricated with Solution-Based Dielectric," *Micromachines (Basel),* vol. 10, no. 7, pp. 446(1-12), Jul 2 2019.

[112] Z. Shen, C. Zhao, Y. Liu, Y. Qi, I. Z. Mitrovic, L. Yang, and C. Zhao, "Performance variation of solution-processed memristor induced by different top electrode," *Solid-State Electronics,* vol. 186, pp. 108132(1-6), 2021.

[237] E. Goi, Q. Zhang, X. Chen, H. Luan, and M. Gu, "Perspective on photonic memristive neuromorphic computing," *PhotoniX,* vol. 1, no. 3, pp. 1-26, 2020.

[246] H.-T. Hsu, D.-L. Yang, L. D. Wiyanto, and J.-Y. Chen, "Red-Light-Stimulated

Photonic Synapses Based on Nonvolatile Perovskite-Based Photomemory," *Advanced Photonics Research,* vol. 2, no. 5, pp. 2000185, 2021.

[247] L. M. Gurtner, M. Hartmann, and F. W. Mast, "Eye movements during visual imagery and perception show spatial correspondence but have unique temporal signatures," *Cognition,* vol. 210, pp. 104597, May 2021.

[248] V. Conboy, C. Edwards, R. Ainsworth, D. Natusch, C. Burcham, B. Danisment, S. Khot, R. Seymour, S. J. Larcombe, I. Tracey, and J. Kolasinski, "Chronic musculoskeletal impairment is associated with alterations in brain regions responsible for the production and perception of movement," *J Physiol,* vol. 599, no. 8, pp. 2255, Apr 2021.

[249] J. A. F. Fabio Pellacini, Donald P. Greenberg, "Toward a psychophysically-based light reflection model for image synthesis," in *27th annual conference on Computer graphics and interactive techniques*, New Orleans, LA USA, 2000, p. 55: SIGGRAPH.

[250] H. Xu, L. Yin, C. Liu, X. Sheng, and N. Zhao, "Recent Advances in Biointegrated Optoelectronic Devices," *Adv Mater,* vol. 30, pp. e1800156, May 28 2018.

[251] Y. Wang, L. Yin, W. Huang, Y. Li, S. Huang, Y. Zhu, D. Yang, and X. Pi, "Optoelectronic Synaptic Devices for Neuromorphic Computing," *Advanced Intelligent Systems,* vol. 3, no. 1, pp. 2000099, 2020.

[252] S. Song, J. Kim, S. M. Kwon, J. W. Jo, S. K. Park, and Y. H. Kim, "Recent Progress of Optoelectronic and All-Optical Neuromorphic Devices: A Comprehensive Review of Device Structures, Materials, and Applications," *Advanced Intelligent Systems,* vol. 3, no. 4, pp. 2000119, 2020.

[253] B. W. Yao, J. Li, X. D. Chen, M. X. Yu, Z. C. Zhang, Y. Li, T. B. Lu, and J. Zhang, "Non-Volatile Electrolyte-Gated Transistors Based on Graphdiyne/MoS_2 with Robust Stability for Low-Power Neuromorphic Computing and Logic-In-Memory," *Advanced Functional Materials,* pp. 2100069, 2021.

[254] Y. Zhou, Y. Huang, X. Xu, Z. Fan, J. B. Khurgin, and Q. Xiong, "Nonlinear optical properties of halide perovskites and their applications," *Applied Physics Reviews,* vol. 7, no. 4, pp. 041313, 2020.

[255] G. Ding, B. Yang, R.-S. Chen, K. Zhou, S.-T. Han, and Y. Zhou, "MXenes for memristive and tactile sensory systems," *Applied Physics Reviews,* vol. 8, no. 1, pp. 011316, 2021.

[256] X. Song, F. Yuan, and L. M. Schoop, "The properties and prospects of chemically exfoliated nanosheets for quantum materials in two dimensions," *Applied Physics Reviews,* vol. 8, no. 1, pp. 011312, 2021.

[257] Y. Wang, Z. Lv, J. Chen, Z. Wang, Y. Zhou, L. Zhou, X. Chen, and S. T. Han, "Photonic Synapses Based on Inorganic Perovskite Quantum Dots for Neuromorphic Computing," *Adv Mater,* vol. 30, no. 38, pp. e1802883, Sep 2018.

[258] H. Han, H. Yu, H. Wei, J. Gong, and W. Xu, "Recent Progress in Three-Terminal Artificial Synapses: From Device to System," *Small,* vol. 15, no. 32, pp. e1900695, Aug 2019.

[259] B. J. Shastri, A. N. Tait, T. Ferreira de Lima, W. H. P. Pernice, H. Bhaskaran, C. D. Wright, and P. R. Prucnal, "Photonics for artificial intelligence and neuromorphic computing," *Nature Photonics,* vol. 15, no. 2, pp. 102, 2021.

[260] J. Jiang, W. Hu, D. Xie, J. Yang, J. He, Y. Gao, and Q. Wan, "2D electric-double-layer phototransistor for photoelectronic and spatiotemporal hybrid neuromorphic integration," *Nanoscale,* vol. 11, no. 3, pp. 1360, Jan 17 2019.

[261] S. W. Cho, S. M. Kwon, M. Lee, J.-W. Jo, J. S. Heo, Y.-H. Kim, H. K. Cho, and S. K. Park, "Multi-spectral gate-triggered heterogeneous photonic neuro-transistors for power-efficient brain-inspired neuromorphic computing," *Nano Energy,* vol. 66, pp. 104097, 2019.

[262] W. Qiu, Y. Huang, L. A. Kong, Y. Chen, W. Liu, Z. Wang, J. Sun, Q. Wan, J. H. Cho, J. Yang, and Y. Gao, "Optoelectronic In-Ga-Zn-O Memtransistors for Artificial Vision System," *Advanced Functional Materials,* vol. 30, no. 40, pp. 2002325, 2020.

[263] L. Yin, W. Huang, R. Xiao, W. Peng, Y. Zhu, Y. Zhang, X. Pi, and D. Yang, "Optically Stimulated Synaptic Devices Based on the Hybrid Structure of Silicon Nanomembrane and Perovskite," *Nano Lett,* vol. 20, no. 5, pp. 3378, May 13 2020.

[264] C. Qian, S. Oh, Y. Choi, J.-H. Kim, J. Sun, H. Huang, J. Yang, Y. Gao, J.-H. Park, and J. H. Cho, "Solar-stimulated optoelectronic synapse based on organic heterojunction with linearly potentiated synaptic weight for neuromorphic computing," *Nano Energy,* vol. 66, pp. 104095, 2019.

[265] S. Lan, J. Zhong, J. Chen, W. He, L. He, R. Yu, G. Chen, and H. Chen, "An optoelectronic synaptic transistor with efficient dual modulation by light illumination," *Journal of Materials Chemistry C,* vol. 9, no. 10, pp. 3412, 2021.

[266] S. Zhao, Y. Wang, W. Huang, H. Jin, P. Huang, H. Wang, K. Wang, D. Li, M. Xu, D. Yang, and X. Pi, "Developing near-infrared quantum-dot light-emitting diodes to mimic synaptic plasticity," *Science China Materials,* vol. 62, no. 10, pp. 1470, 2019.

[267] S. D. Basudev Pradhan, Jinxin Li, Farzana Chowdhury, Jayesh Cherusseri, Deepak Pandey, Durjoy Dev, Adithi Krishnaprasad, Elizabeth Barrios, Andrew Towers, Andre Gesquiere, Laurene Tetard, Tania Roy, Jayan Thomas, "Ultrasensitive and ultrathin phototransistors and photonic synapses using perovskite quantum dots grown from graphene lattice," *SCIENCE ADVANCES,* vol. 6, pp. eaay5225, 2020.

[268] K. Pilarczyk, A. Podborska, M. Lis, M. Kawa, D. Migdal, and K. Szaciłowski, "Synaptic Behavior in an Optoelectronic Device Based on Semiconductor-Nanotube Hybrid," *Advanced Electronic Materials,* vol. 2, no. 6, pp. 1500471, 2016.

[269] Y. Choi, J. H. Kim, C. Qian, J. Kang, M. C. Hersam, J. H. Park, and J. H. Cho, "Gate-Tunable Synaptic Dynamics of Ferroelectric-Coupled Carbon-Nanotube Transistors," *ACS Appl Mater Interfaces,* vol. 12, no. 4, pp. 4707, Jan 29 2020.

[270] X. Y. Jinran Yu, Guoyun Gao, Yao Xiong, Yifei Wang, Jing Han, Youhui Chen, Huai Zhang, Qijun Sun, Zhong Lin Wang, "Bioinspired mechano-photonic

artificial synapse based on graphene/MoS2 heterostructure," *SCIENCE ADVANCES,* vol. 7, pp. eabd9117, 2021.

[271] Y. W. Zhenyi Ni, Lixiang Liu, Shuangyi Zhao, Yang Xu, Xiaodong Pi, and Deren Yang, "Hybrid Structure of Silicon Nanocrystals and 2D WSe_2 for Broadband Optoelectronic Synaptic Devices," presented at the 2018 IEEE International Electron Devices Meeting (IEDM), San Francisco, CA, USA, 2018.

[272] J. Sun, S. Oh, Y. Choi, S. Seo, M. J. Oh, M. Lee, W. B. Lee, P. J. Yoo, J. H. Cho, and J.-H. Park, "Optoelectronic Synapse Based on IGZO-Alkylated Graphene Oxide Hybrid Structure," *Advanced Functional Materials,* vol. 28, no. 47, pp. 1804397, 2018.

[273] G. Cao, P. Meng, J. Chen, H. Liu, R. Bian, C. Zhu, F. Liu, and Z. Liu, "2D Material Based Synaptic Devices for Neuromorphic Computing," *Advanced Functional Materials,* vol. 31, no. 4, pp. 2005443, 2020.

Supplementary Information

In the section of the supplementary information, some data and illustrations with minor significance were included.

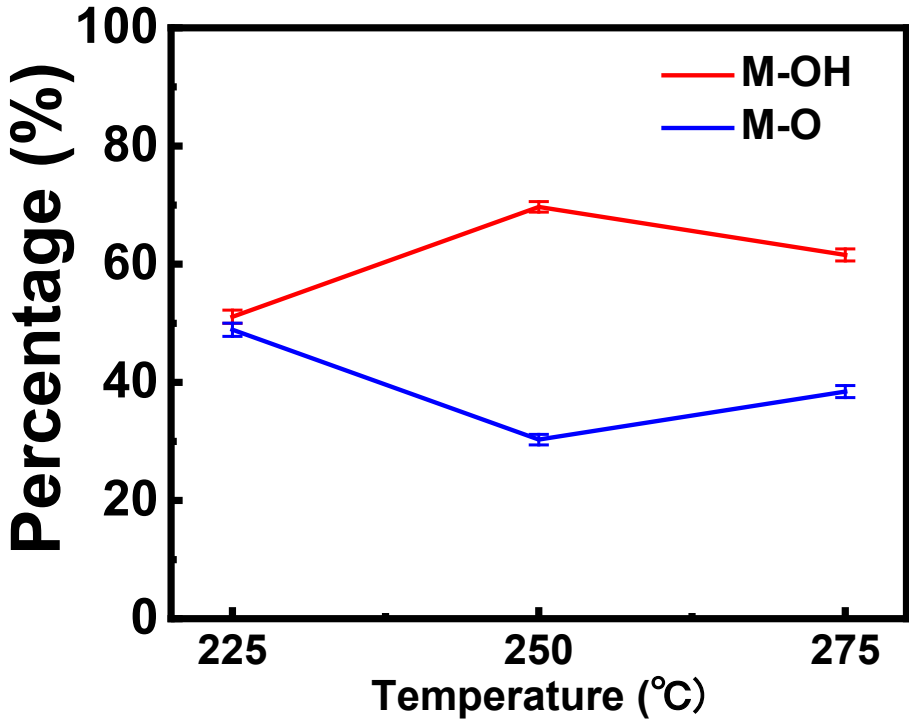

Figure SI-1. Integrated intensities of O 1s CL sub-peak referring to M-OH bond and M-O bond for solution-based AlOx layers annealed at different temperatures.

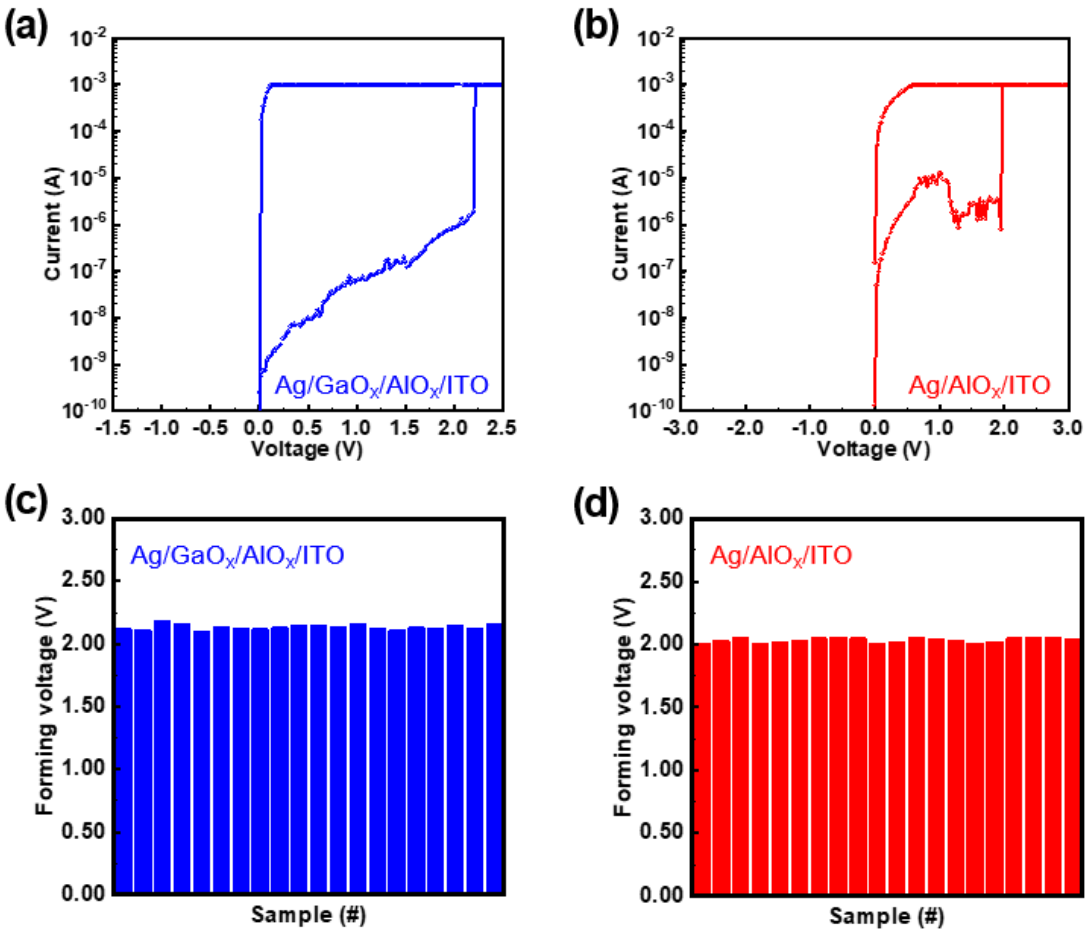

Figure SI-2. Single forming operations of (a) Ag/SP-GaO_x/SP-AlO_x/ITO and (b) Ag/SP-AlO_x/ITO RRAM devices. Device-to-device variation of forming voltages for (c) Ag/SP-GaO_x/SP-AlO_x/ITO and (d) Ag/SP-AlO_x/ITO RRAM devices.

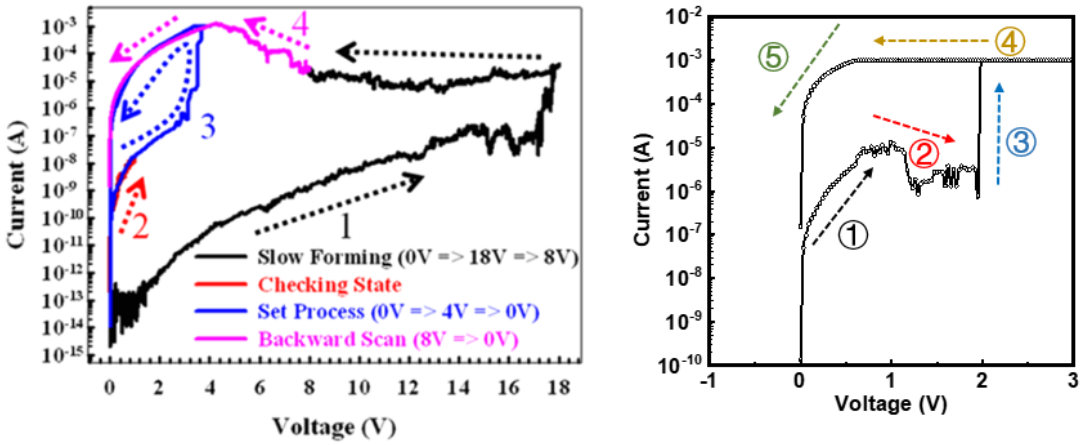

Figure SI-3. (a) The backward scan effect of RRAM device with SiO_x layer. (Step 1). Forming voltage sweep with the slow rate (1000 points in sweep range). (Step 2). Checking state from 0 V

to 1 V . (Step 3). Set process by 4 V forward/reverse sweep with 1 mA compliance current limit. (Step 4). Backward scan effect in SiO_x-device. (b) The single forming process of Ag/AlO_x/ITO RRAM devices.